UNIVERSITY OF OKLAHOMA

GRADUATE COLLEGE

SYNTHETIC SPECTRUM METHODS FOR THREE DIMENSIONAL SUPERNOVA MODELS

A Dissertation

SUBMITTED TO THE GRADUATE FACULTY

in partial fulfillment of the requirements for the

degree of

Doctor of Philosophy

By

Rollin C. Thomas

Norman, Oklahoma

2003

Downloaded from SHAREOK. Persistent Handle URL: https://hdl.handle.net/11244/615

UMI Number: 3093583

UMI®

UMI Microform 3093583

Copyright 2003 by ProQuest Information and Learning Company.

All rights reserved. This microform edition is protected against unauthorized copying under Title 17, United States Code.

ProQuest Information and Learning Company
300 North Zeeb Road
P.O. Box 1346
Ann Arbor, MI 48106-1346

©Copyright by Rollin C. Thomas 2003
All Rights Reserved.

SYNTHETIC SPECTRUM METHODS FOR
THREE DIMENSIONAL SUPERNOVA MODELS

A Dissertation APPROVED FOR THE
DEPARTMENT OF PHYSICS AND ASTRONOMY

By

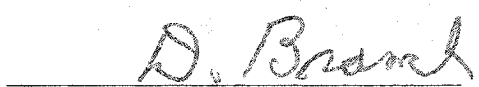

David Branch
Dissertation Committee Chair



Eddie Baron



John Cowan



Ron Kantowski

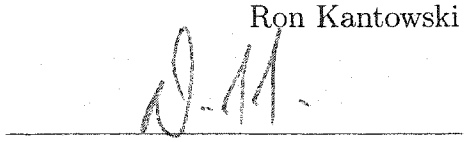

Dan Tuckness

ACKNOWLEDGMENTS

I am pleased to thank David Branch and Eddie Baron, my research advisors since 1997, for their patient indulgence of my bad ideas, stupid questions, and confused mental digressions. I look forward to continue being educated by them for years to come. They provided needed encouragement at key points during my time at the University of Oklahoma, and a real education in radiative transfer, supernovae, and how science is done. I also commend the efforts of my entire doctoral committee for never causing scheduling problems, for their dedication and diligence, and for asking hard questions.

I thank student members of the OU SN group past and present as well. I look forward to building on two years of collaboration with Dan Kasen. Darrin Casebeer deserves credit for working through some early Monte Carlo transfer issues with me, and for suggesting the name of the code, `Brute`. Eric Lentz (directly) and Adam Fisher (indirectly) are responsible for clearing up a lot of my misconceptions about radiative transfer and the Sobolev approximation. I also thank Dean Richardson for not completely using up the internet.

For their support of interest in my education over many years, I thank my family. Especially for her sacrifices, her understanding, her friendship, and artwork assistance, I am deeply indebted to Dianna.

Contents

1 **Introduction** 1

2 **The Model SN Atmosphere Problem** 13
- 2.1 The Radiation Transfer Equation . . . 15
- 2.2 Basic Assumptions and Consequences . . . 20
  - 2.2.1 Assumptions – The Elementary Supernova Model . . . 21
  - 2.2.2 The Sobolev Approximation and the ES Model . . . 22

3 **Line Formation in 3D SN Models** 31
- 3.1 Spectra from Clumpy SNe Ia . . . 34
  - 3.1.1 `Synow` and `ClumpySyn` . . . 34
  - 3.1.2 `ClumpySyn` Spectra . . . 40
- 3.2 Single Scattering Line Profiles in 3D Models . . . 41
- 3.3 Multiple Scattering Line Profiles in 3D Models . . . 48
- 3.4 Role of Perspective-Dependence in Spectroscopic Diversity . . . 56
- 3.5 Summary . . . 66

4 **High-Velocity Ejecta in the Peculiar SN Ia 2000cx** 68
- 4.1 Spectra . . . 70
- 4.2 Fits . . . 73
  - 4.2.1 `Synow` Fits . . . 74
  - 4.2.2 `synBrute` Fit . . . 83
- 4.3 Discussion . . . 85
  - 4.3.1 HV Ejecta Geometry from the Fits . . . 85
  - 4.3.2 HV Ejecta Mass Estimates . . . 89
- 4.4 Summary . . . 97

5 **3D LTE Modelling** 99
- 5.1 Radiative Equilibrium . . . 100
- 5.2 Application . . . 103
- 5.3 Continuous Opacity . . . 105
- 5.4 Equivalent Two Level Atom . . . 106
- 5.5 1D Example - Mixed W7 . . . 106
- 5.6 3D Example – W7 with HV Clump . . . 110
- 5.7 Summary and Conclusion . . . 112

6 Summary and Conclusions 113

A tauBrute 120
A.1 CellClass . . . 120
A.1.1 Cell_new . . . 120
A.1.2 Cell_copy . . . 122
A.1.3 Cell_die . . . 122
A.1.4 nextTemp . . . 122
A.1.5 defCell . . . 122
A.1.6 undefCell . . . 123
A.1.7 showCellShort . . . 123
A.1.8 showCellLong . . . 123
A.1.9 localIndex . . . 123
A.1.10 thermalize . . . 124
A.2 CharClass . . . 124
A.2.1 Char_new . . . 124
A.2.2 Char_copy . . . 124
A.2.3 Char_die . . . 124
A.2.4 showChar . . . 124
A.2.5 setObserver_phth . . . 125
A.2.6 setObserver_nhat . . . 125
A.3 CoreClass . . . 125
A.3.1 Core_new . . . 125
A.3.2 Core_copy . . . 125
A.3.3 Core_die . . . 126
A.3.4 showCore . . . 126
A.3.5 point . . . 126
A.3.6 beam . . . 126
A.3.7 ray . . . 127
A.3.8 segment . . . 127
A.3.9 intPoints . . . 127
A.3.10 dilFactor . . . 127
A.3.11 getLaunch . . . 128
A.4 GridClass . . . 128
A.4.1 Grid_new . . . 128
A.4.2 Grid_copy . . . 128
A.4.3 Grid_die . . . 128
A.4.4 setCellMap . . . 128
A.4.5 unsetCellMap . . . 129
A.4.6 showGrid . . . 129
A.4.7 activeVolume_cmps3 . . . 129
A.4.8 activeVolume_kmps3 . . . 129
A.5 Lambda . . . 130
A.5.1 setLambdas_range . . . 130

A.5.2 setLambdas_array . . . 130
A.5.3 unsetLambdas . . . 130
A.5.4 showLambdasShort . . . 130
A.5.5 showLambdasMedium . . . 130
A.5.6 showLambdasLong . . . 130
A.5.7 linkLambdas_array . . . 131
A.5.8 linkLambdas_umask . . . 131
A.5.9 showLambdasLinked . . . 131
A.5.10 getLambdaIndex . . . 131
A.5.11 getLambdaLinkedIndex . . . 131
A.6 RandomClass . . . 132
A.6.1 Random_new . . . 132
A.6.2 Random_copy . . . 132
A.6.3 Random_die . . . 132
A.6.4 unifDev_sngl . . . 132
A.6.5 unifDev_mult . . . 132
A.6.6 expoDev . . . 133
A.7 Scheme . . . 133
A.7.1 setScheme . . . 133
A.7.2 unsetScheme . . . 133
A.7.3 showScheme . . . 133
A.8 SedClass . . . 134
A.8.1 Sed_new . . . 134
A.8.2 Sed_copy . . . 134
A.8.3 Sed_die . . . 134
A.8.4 showSed . . . 134
A.8.5 pickFromSed . . . 134
A.9 Spectrum . . . 135
A.9.1 setSpectrum . . . 135
A.9.2 unsetSpectrum . . . 135
A.9.3 calcSpectrum . . . 135
A.10 TempClass . . . 136
A.10.1 Temp_new_int . . . 136
A.10.2 Temp_new_rwp . . . 136
A.10.3 Temp_copy . . . 136
A.10.4 Temp_die . . . 137
A.10.5 showTemp . . . 137
A.10.6 cacheTemp . . . 137
A.10.7 fetchTemp . . . 137
A.11 Transport . . . 137
A.11.1 ssTransport . . . 137
A.11.2 msTransport . . . 138

B synBrute 139
B.1 Kurucz1993 . . . 141
B.1.1 hasKuruczPath . . . 141
B.1.2 setKuruczPath . . . 141
B.1.3 onDisk . . . 141
B.1.4 connect . . . 141
B.1.5 disconnect . . . 141
B.1.6 isConnected . . . 141
B.1.7 hasLine_sngl . . . 142
B.1.8 hasLine_mult . . . 142
B.1.9 numLines_totl . . . 142
B.1.10 numLines_lglo . . . 142
B.1.11 numLines_wllm . . . 142
B.1.12 numLines_lglo_wllm . . . 143
B.1.13 selectLine_sngl . . . 143
B.1.14 selectLine_refl . . . 143
B.1.15 selectLine_mult . . . 143
B.1.16 selectLine_totl . . . 143
B.1.17 selectLine_lglo . . . 144
B.1.18 selectLine_wllm . . . 144
B.1.19 selectLine_lglo_wllm . . . 144
B.2 LineClass . . . 145
B.2.1 lineCount . . . 145
B.2.2 Line_new . . . 145
B.2.3 refLine . . . 145
B.2.4 locateLine . . . 145
B.2.5 setBands . . . 146

C lteBrute 147
C.1 AtomData . . . 147
C.1.1 ionStageLabel . . . 147
C.1.2 atomLabel . . . 149
C.1.3 ionLabel . . . 149
C.1.4 atomWeight . . . 149
C.2 LtePartFunc . . . 149
C.2.1 hasLtePartFunc . . . 149
C.2.2 getLtePartFunc . . . 149
C.2.3 getChi . . . 150
C.3 CompClass . . . 150
C.3.1 Comp_new . . . 150
C.3.2 Comp_file . . . 150
C.3.3 Comp_copy . . . 150
C.3.4 Comp_die . . . 151
C.3.5 getMu . . . 151

C.3.6 dumpComp 151
C.4 LteEosClass 151
C.4.1 LteEos_new 151
C.4.2 LteEos_copy 151
C.4.3 LteEos_die 152
C.4.4 setLteEos 152

D List of Acronyms **153**

List of Tables

4.1 Synow fit parameters for non-calcium ions in SN 2000cx 75
4.2 Synow Ca II Fit Parameters for SN 2000cx 76

List of Figures

1.1 Schematic P-Cygni line profile. 2
1.2 Geometry resulting in a P-Cygni line profile. 3
1.3 Example SN spectra at maximum light. 5
1.4 The SN classification system. 6
1.5 Example SN light curves. 7

2.1 Geometry defining the specific intensity. 16
2.2 Geometry for the formal solution. 18
2.3 Observer frame picture of the ES atmosphere. 23
2.4 Comoving frame picture of the ES atmosphere. 24
2.5 CP surface in 3D atmosphere geometry. 28
2.6 CD surface in 3D atmosphere geometry. 29

3.1 A sample clumpy model with 66% of the envelope filled 41
3.2 `ClumpySyn` calculations for volume filling factor 0.85. 42
3.3 `ClumpySyn` calculations for volume filling factor 0.75. 42
3.4 `ClumpySyn` calculations for volume filling factor 0.66. 43
3.5 `ClumpySyn` calculations for volume filling factor 0.54. 43
3.6 Layout for clump examples. 44
3.7 Single line profiles forming in a single clump, $S = J$ 46
3.8 Single line profiles forming in a single clump, $S = I_{ph}$ 47
3.9 Computing J without and with Monte Carlo 50
3.10 Line blend formation in a clump, small separation. 54
3.11 Line blend formation in a clump, large separation. 55
3.12 White noise parameterization. 57
3.13 An example optical depth distribution for white noise experiments . . 58
3.14 Example white noise line and covering fraction profiles 59
3.15 White noise profile diversity plots for $s_c = 0.18$ 61
3.16 White noise profile diversity plots for $s_c = 0.30$ 62
3.17 White noise profile diversity plots for $s_c = 0.53$ 63
3.18 White noise profile diversity plots for $s_c = 1.01$ 64
3.19 White noise profile diversity plots for $s_c = 1.96$ 65
3.20 Line profile deviation as a function of covering fraction deviation. . . 66
3.21 Si II absorption features in maximum light SNe Ia 67

4.1 Near-maximum light spectra of SN 2000cx 70

4.2 Ca II features in SN 2000cx 72
4.3 Synow fit 1D1 of SN 2000cx 77
4.4 Synow fit 1D1 of Ca II features in SN 2000cx 78
4.5 Synow fit 1D1PV of Ca II features in SN 2000cx 80
4.6 Synow fit 1D1HV of Ca II features in SN 2000cx 81
4.7 Synow fit 1D2 of Ca II features in SN 2000cx 82
4.8 Synow fit 1D3 of Ca II features in SN 2000cx 84
4.9 Ca II reference line optical depth along $-z$ axis in 3D model 85
4.10 synBrute fit of Ca II features in SN 2000cx 86
4.11 Ca II signatures in C/O-rich composition 92
4.12 Ion signatures in C/O-rich composition 94
4.13 synBrute fit to SN 2000cx including hydrogen 96

5.1 One zone mixed W7 temperature structures without e^-. 107
5.2 One zone mixed W7 spectra without e^-. 108
5.3 One zone mixed W7 spectra without e^-. 109
5.4 One zone mixed W7 spectra with HV clump. 111

A.1 Flowchart for the tauBrute code. 121

B.1 Flowchart for the synBrute code. 140

C.1 Flowchart for the lteBrute code. 148

ABSTRACT

This dissertation describes some problems associated with synthesizing emergent spectra from three-dimensional supernova envelope models. We confront these problems by developing a three-dimensional implementation of a hybrid Sobolev/Monte Carlo technique. A collection of experiments (extending from the illustrative to the more detailed) are included.

Chapter 1

Introduction

A few days to weeks after explosion, the spectrum of a supernova (SN) consists of a bewildering mess of overlapping P-Cygni line profiles (Figure 1.1) superposed on a pseudo-thermal continuum. This type of line profile is characteristic of an optically thick stellar core surrounded by an extended, expanding line forming region as depicted in Figure 1.2. The material between the observer and the core is expanding toward the observer, resulting in a blueshifted absorption, while the rest of the material (excluding that occulted by the core) contributes to an emission feature peaked at the rest wavelength of the line. In SNe, the observed Doppler shifts in the blue absorption components of the line profiles suggest velocities on the order of 10^4 km s^{-1}. These events are energetic phenomena; they can rival their host galaxies in energy production at maximum brightness.

SNe, along with planetary nebulae, are the means through which accumulated light elements from a stellar lifetime of nucleosynthesis are dispersed into the interstellar medium. This material, and freshly synthesized heavier elements, go into the production of the next generation of stars. The production of compact objects such as neutron stars and black holes are the direct result of some SNe. White dwarfs

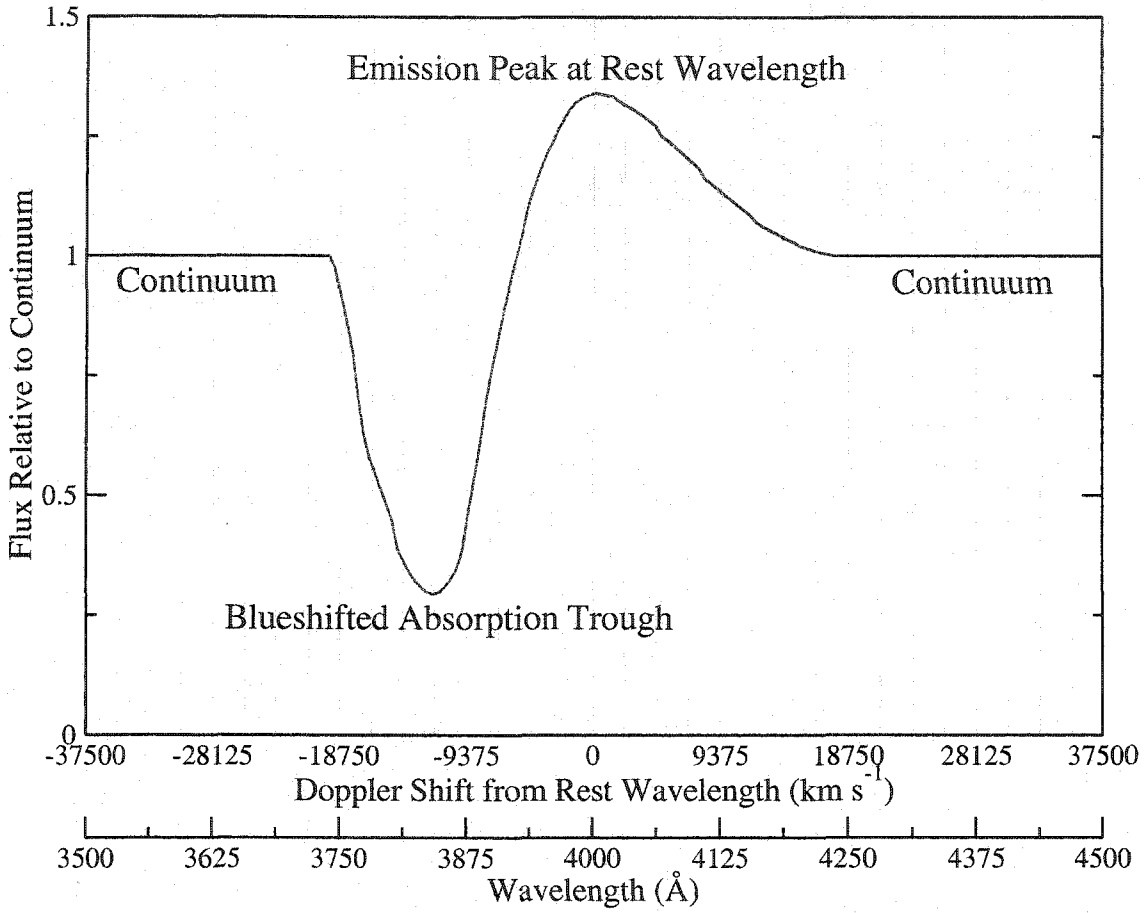

Figure 1.1: Schematic P-Cygni line profile. The blueshifted absorption trough comes from material blocking the core of the object, expanding toward the observer. The emission feature is peaked at the rest wavelength, and results from light scattered toward the observer.

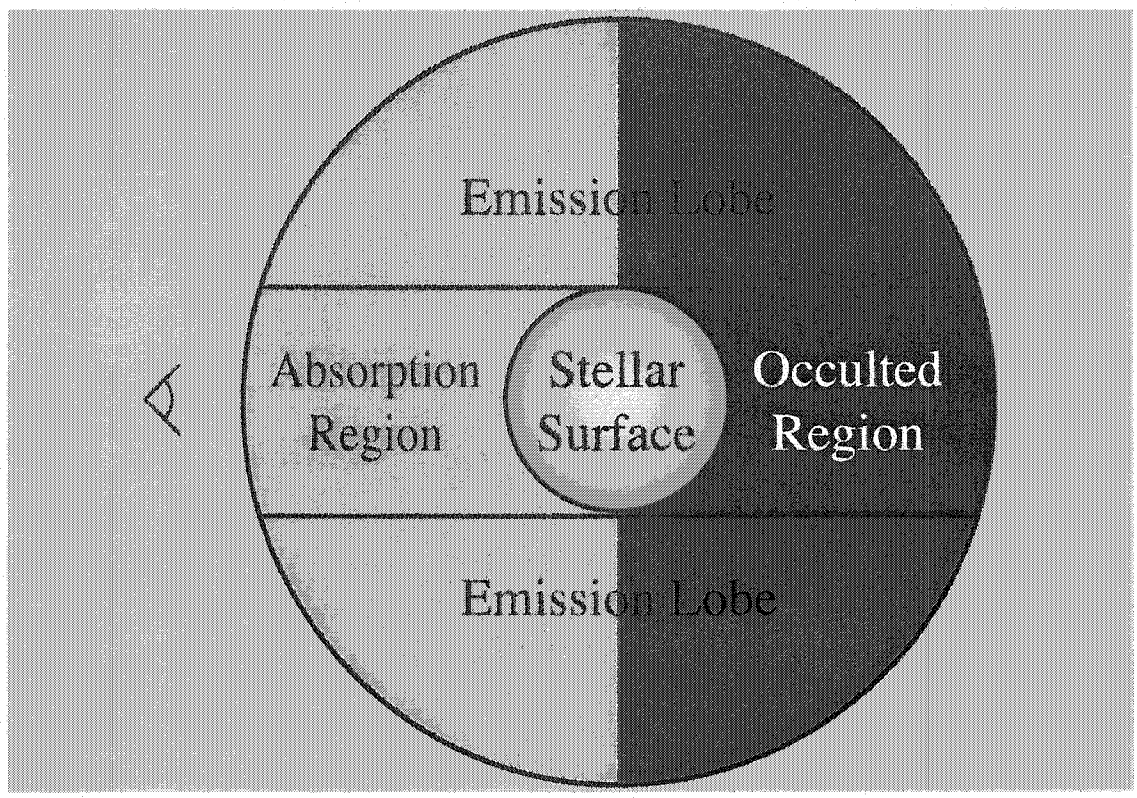

Figure 1.2: Geometry resulting in a P-Cygni line profile. In this simplistic picture, the extended line forming region above the stellar surface is optically thin to continuum radiation, but is optically thick to line radiation. The far side of the emission lobe is moving away from the observer (at the left), resulting in an emission feature extending to the red of the rest wavelength of the line.

are destroyed in other SN scenarios, and their consumption is responsible for the production of heavier elements required for building terrestrial planets.

The result of the explosive ejection of a stellar atmosphere at high velocity is uniform motion homologous expansion (homologous expansion for short), mathematically $v \propto r$. Right after explosion, the SN ejecta move apart so rapidly that the distances separating different portions become large very quickly. Different parts of the ejecta cannot interact hydrodynamically, so free expansion is the result. Homologous expansion is also descriptive of the Hubble expansion of the universe: As seen from an observer at one point in the universe, all other points recede and do so at rates proportional to their distances from the observer.

Figure 1.3 shows several SN spectra near the time of maximum light. Some features are distinct P-Cygni profiles but others may consist of several overlapping blends of lines. SNe are roughly categorized according to the appearance of their spectra at this phase; the presence or absence of certain ion signatures forms the basis of the classification system. Strictly speaking, the presence of Balmer hydrogen in a spectrum characterizes a Type II SN (SN II) while its absence marks a Type I event (SN I) – see Figure 1.4. These classes are further subdivided based on the presence of other features and additionally according to light curve shape (examples in Figure 1.5 – Wheeler, 1990). This simplified system provides a set of general guidelines for grouping events, but the underlying astrophysics (the progenitor star, the immediate environment of the SN) is what differentiates one SN from another.

The presence of Balmer hydrogen features in SN II spectra suggests that the progenitors of these events are massive stars with intact hydrogen envelopes. Massive stars spend millions of years burning hydrogen into helium, and burning heavier product elements into even heavier ones. The process stops at iron, at the peak of the binding energy per nucleon curve. At this point, the core is supported only by degenerate electron pressure. As burning in a shell around the core progresses, the

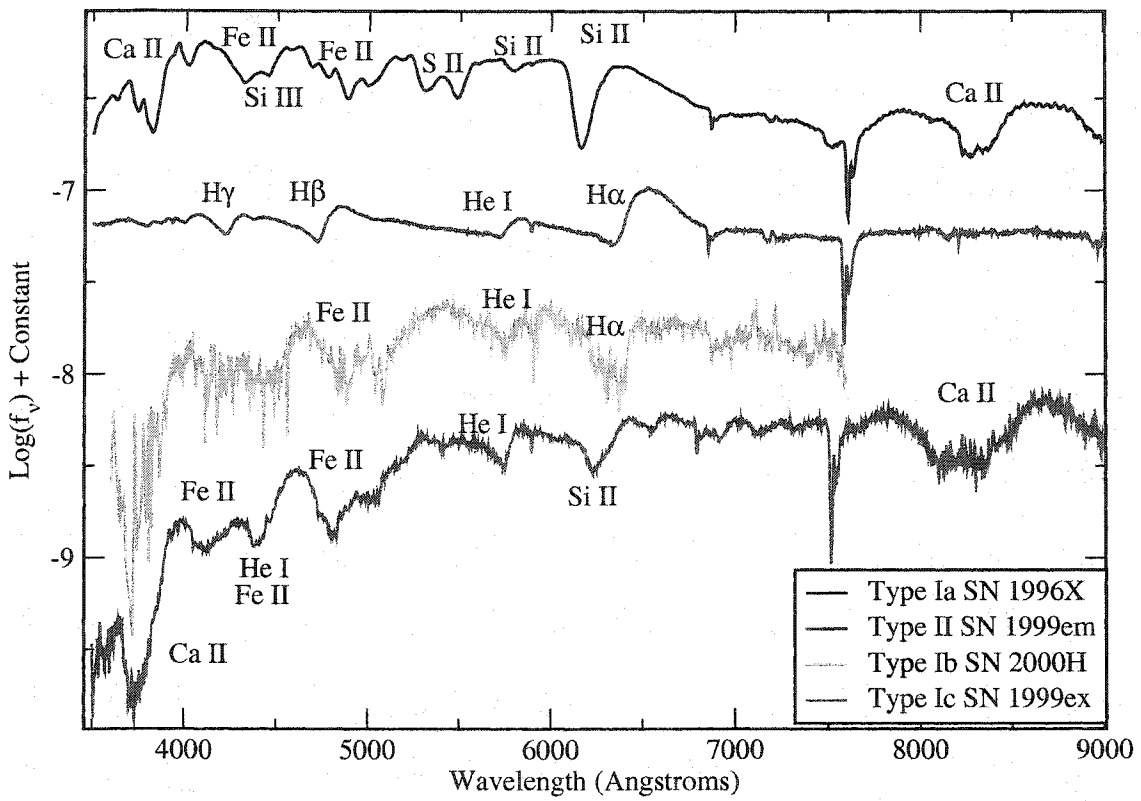

Figure 1.3: Example SN spectra at maximum light. From top to bottom are SN Ia 1996X, SN II 1999em, SN Ib 2000H, and SN Ic 1999ex. Note the somewhat loose adherence to the spectroscopic classification system. For example, SN Ib 2000H has a strong Balmer Hα absorption signature.

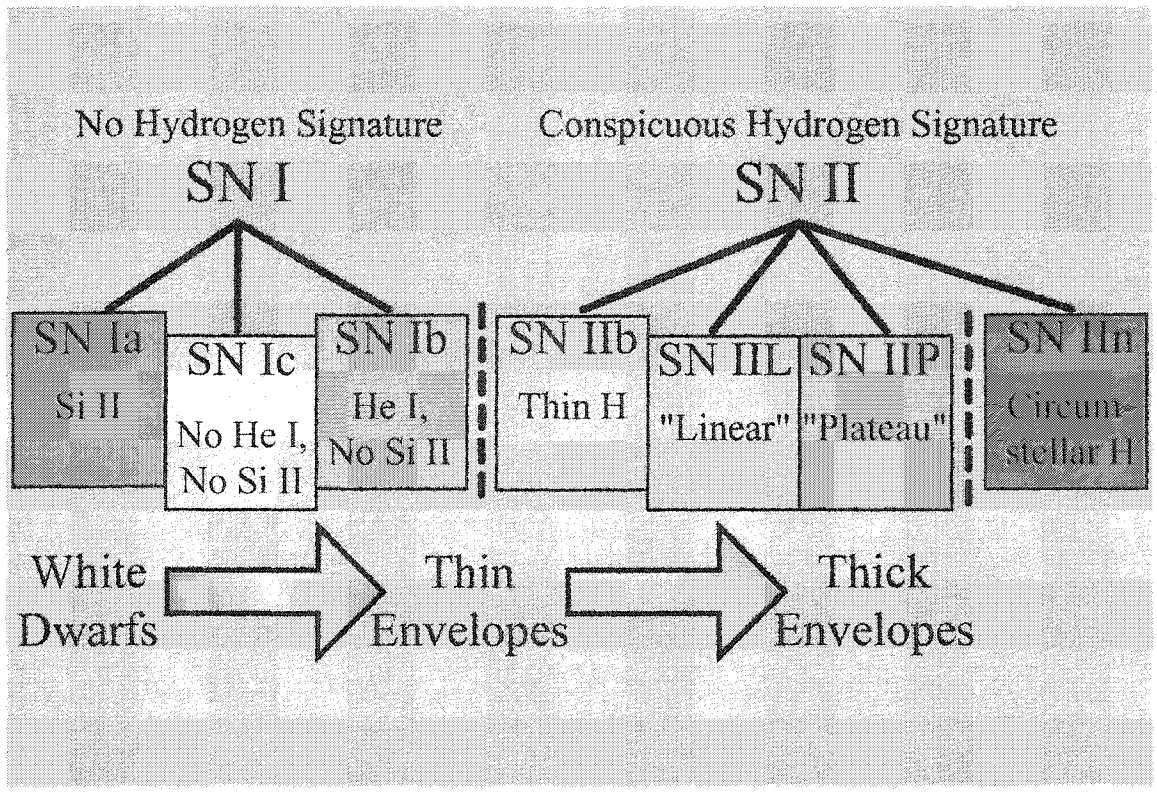

Figure 1.4: The SN classification system. This system is an informal way of grouping events based mostly on spectroscopic signatures. Those on the left tend to lack hydrogen signatures, while these features are apparent in those on the right. This suggests a sequence based on progenitor star envelope mass and environment at explosion time.

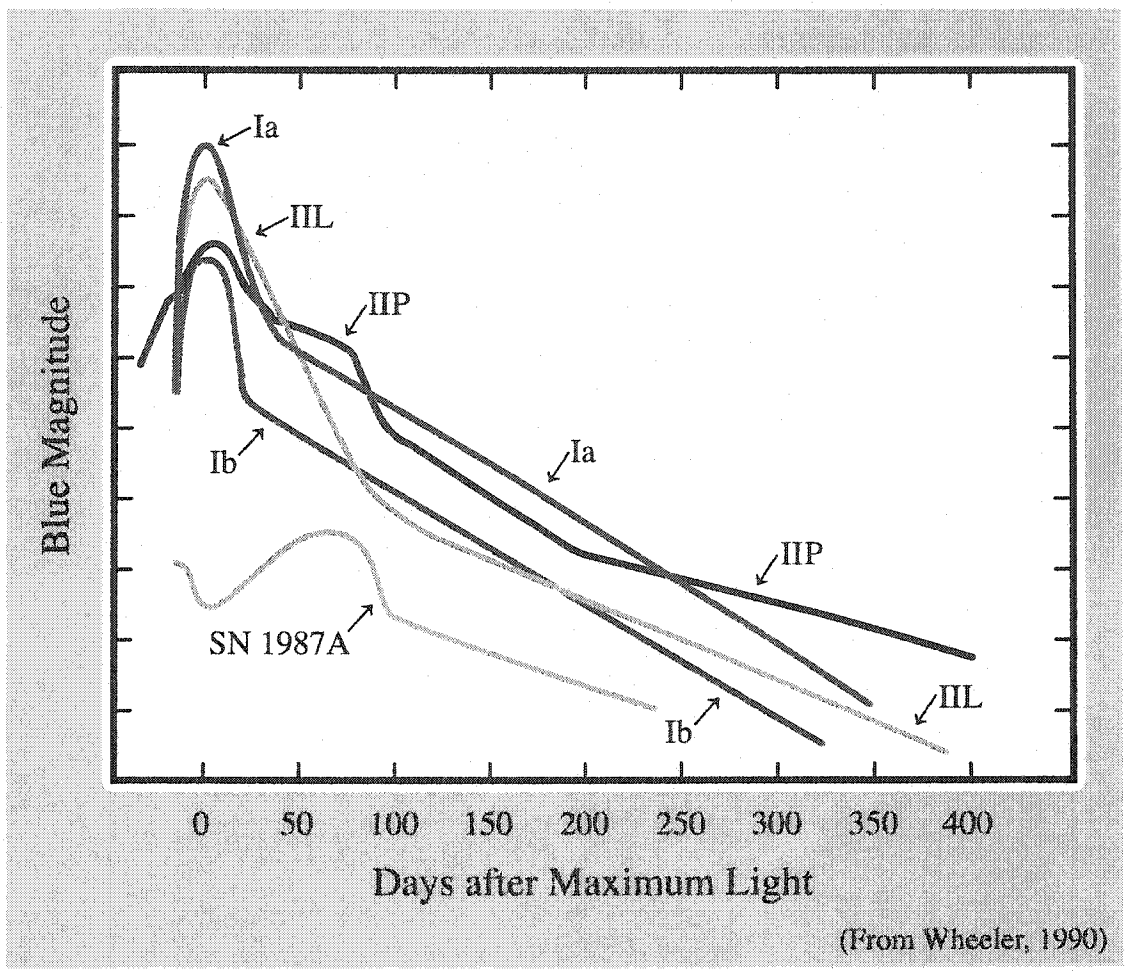

Figure 1.5: Example SN light curves. Light curve shape is another way to group SNe together. Two SN II categories depend on light curve shape (IIP for "plateau" SN II light curves and IIL for "linearly" decaying SN II light curves). The peak of each light curve is commonly referred to as "maximum light."

core becomes more massive and contracts. At some point, rapid neutronization occurs when electrons combine with protons, robbing the core of its source of support. The core collapses, sending a powerful shock upward into the surrounding envelope. This shock deposits energy into the expanding envelope, and the subsequent release of this energy as radiation largely powers the light curve of a SN II.

The weakness or absence of Balmer hydrogen lines in other SN types suggests that the corresponding progenitors have a stripped hydrogen envelope or none at all. The standard SN Ia model involves the thermonuclear disruption of a white dwarf (not collapse), and the light curve is powered by the radioactive decay of product ^{56}Ni to ^{56}Co to ^{56}Fe. SNe Ib/c are thought to result from core collapse in evolved stars which have somehow shed an appreciable fraction of their outer layers prior to collapse.

In order to understand these events it is clearly necessary to do more than classify them. Thus, SN explosions are *simulated* numerically and the results of these hydrodynamical explosion calculations are somehow *compared* with observed SNe. Hydrodynamical models are validated or falsified through the synthesis of their emergent spectra and the evaluation of those spectra with respect to observations. Conversely, parameterized or model-independent techniques of spectrum synthesis provide general, qualitative constraints for explosion simulators – suggesting where in the ejecta certain nucleosynthesis products should be found. Clearly, the endeavor of SN spectrum synthesis is crucial for a full reconciliation of model SN explosions with real events.

Historically, one-dimensional (1D) or spherically symmetric explosion models have been used to synthesize emergent spectra in good agreement with observed ones (Branch et al., 1985; Nugent et al., 1995; Mitchell et al., 2001). But new data and new computational technologies have led to a new class of *multidimensional* explosion models, making the need for multidimensional spectrum synthesis more pressing. Three distinct pieces of evidence make a compelling case for the existence of ejecta

distributions deviating from spherical symmetry.

• **Polarization Phenomena.** First proposed as a useful diagnostic of SN envelope geometry by Shapiro & Sutherland (1982), polarization measurements can characterize shape asymmetries on large scales. The envelopes of young SNe are dominated by the polarizing process of electron scattering. Thus, an unresolved spherical SN envelope will evince no net polarization since the electric vector components from different parts of the envelope completely cancel one another. But if the envelope shape is ellipsoidal, for example, a net polarization signature arises due to incomplete cancellation. Polarization measurements consistent with such envelope asymmetries (and others) are frequently present in stripped-envelope core collapse events (SNe IIb, Ib and Ic) and in events with circumstellar interaction (SNe IIn) (Wang et al., 2001; Leonard et al., 2000; Wheeler, 2000). A core collapse event, enshrouded by an intact hydrogen envelope, tends to be less polarized but polarization in this case can increase as the SN expands and reveals its deeper, more asymmetric inner layers (Leonard et al., 2000). Most thermonuclear SNe (SNe Ia) fail to exhibit polarization (Wang et al., 2001), but there are noteworthy exceptions (Howell et al., 2001; Wang et al., 1997, 2003).

• **Spectroscopic Phenomena.** A clumpy or macroscopically mixed ejecta distribution (or at least an ionization/temperature structure deviating from spherical symmetry) has been invoked to explain certain flux spectrum features. Most notably, the "Bochum event" in the Hα feature of the SN II 1987A (about 20 days after explosion, see Phillips & Heathcote, 1989) has been attributed to an asymmetry in the distribution of ^{56}Ni resulting in an asymmetric over-excitation of hydrogen in the ejecta (Utrobin et al., 1995). Spectroscopic features observed a few months to years after explosion have been used to obtain envelope filling factors for certain ions which are much less than unity and indicative of ejecta clumping (Spyromilio, 1991; Spyromilio & Pinto, 1991; Li & McCray, 1992; Spyromilio, 1994), but this is still

uncertain (Houck & Fransson, 1996). Some mixing of freshly synthesized radioactive nickel from the core is required for detailed synthetic spectra to fit the observed spectra of the SNe II 1987A (Mitchell et al., 2001) and 1995V (Fassia et al., 1998). In the case of SN 1987A, the mixing must be macroscopic and the clumps must evolve in size (Li et al., 1993). The SNe Ia 2001el (Kasen et al., 2003) and 2000cx (Thomas et al., 2003) possess high velocity Ca II features which can be explained as signatures of deviation from spherical symmetry. In the case of SN 2001el, polarization data corroborates this hypothesis.

• **Supernova Remnant Morphologies.** Probably the most conspicuous indication of macroscopic mixing in SN envelopes comes from the interesting morphologies of SN remnants. The presence of moving shrapnel in Galactic SN remnants such as Cas A (Fesen & Gunderson, 1996; Hwang et al., 2000), Vela (Tsunemi et al., 1999), and Tycho (Decourchelle et al., 2001) has been interpreted in the context of hydrodynamical instabilities resulting in the ejection of a clumpy envelope (Chevalier & Klein, 1978; Burrows et al., 1995; Kifonidis et al., 2000). The resulting clumps evolve into the observed knots and filaments as the remnant ages and interacts with the interstellar medium (Anderson et al., 1994).

• **Other Evidence.** These more direct clues supporting the existence of deviation from spherical symmetry in SN envelopes are bolstered by other indirect arguments. The space velocity distribution of pulsars is known to be anomalous, with an average of 450 km s^{-1}, leading some to suggest that they are born with kicks from asymmetric SN explosions (Cordes & Chernoff, 1998). In addition, there is evidence supporting a correspondence between some core collapse SNe and gamma ray bursts (GRBs). Some SNe have been spatially correlated with GRB afterglows (SN 1998bw & GRB 980425, SN 1997cy & GRB 970514, and most recently SN 2003dh & GRB 030329 – Stanek et al., 2003). Jet-induced SN explosions, resulting in prodigious deviation from spherical symmetry, have been modelled in an attempt to unify these two phenomena

(see, for example – MacFadyen et al., 2001).

It is clear that to fully understand SNe, explain the aforementioned phenomena and investigate the link between SNe and GRBs, three-dimensional (3D) explosion models are necessary (fresh, exciting preliminary models have been published recently – Reinecke et al., 2002; Gamezo et al., 2003; Kifonidis et al., 2003). Hence, there is a need for 3D spectrum synthesis for SNe.

The SN research group at the University of Oklahoma primarily uses two highly successful codes for the synthesis of SN spectra. One is the well-known general-purpose stellar atmosphere code `PHOENIX` (Hauschildt & Baron, 1999), which solves the fully relativistic moving-atmosphere radiation transport and non-local thermodynamic equilibrium rate equations. The second is the simple, parameterized, and fast code `Synow` (Fisher, 2000; Branch et al., 2002; Millard et al., 1999). `PHOENIX` is referred to as a *detailed analysis* code since its users strive to replicate all relevant physical phenomena in their simulations. On the other hand, `Synow` is a *direct analysis* code chiefly for the identification of spectral features, ejecta velocity measurements, and general qualitative spectrum assessments. Both codes rely on spherical symmetry, however, and thus are not directly useful for addressing problems of SN geometry.

In this dissertation, we focus on some problems associated with spectrum synthesis for 3D models of SNe. The structure is as follows:

In **Chapter 2**, we provide a brief overview of the model atmospheres problem in the context of SNe. We also include a brief discussion of the Sobolev method of line radiative transfer, focusing on its direct application to the SN problem.

Some very simple arguments and models are used to present general constraints on composition clumping in **Chapter 3**. These constraints are general "rules of thumb" useful for thinking about SN line formation outside of the assumption of spherical symmetry.

In **Chapter 4**, a parameterized technique is used to analyze a SN Ia with high-velocity absorption features. We investigate the geometry of this high-velocity ejecta, and suggest a viable 3D model and speculate on the origin of the ejecta.

Chapter 5 is concerned with more self-consistent transfer techniques for 3D SN models. These models use a radiative equilibrium technique implemented for the first time in the 3D SN case. Example spectra and parameter studies are included, as well as details about how the method works. The results presented here are the first small step toward validating 3D explosion models to come in the next decade.

A summary is presented in **Chapter 6**. Problems to overcome and suggestions for future research projects are included.

For completeness and for future programming reference, three **Appendices** are included to address some technical aspects of the programs used to produce results presented. This discussion includes simple descriptions of the code and some diagrams to express relationships between program components. These Appendices are not intended to be an exhaustive discussion of the codes; rather they just provide some technical details.

Chapter 2

The Model SN Atmosphere Problem

Our ultimate goal is to obtain solutions to the model atmospheres problem in the special context of 3D SN models. Simply put, the model atmospheres problem involves the construction of a self-consistent description of the matter and ambient radiation field in a stellar atmosphere through mathematical (computational) modelling. The motivation for confronting this problem in this context is that its solution permits the matching of spectroscopic phenomena (i.e. unusual line profiles) with deviation from spherical symmetry in model SN atmospheres.

Along the way to solving the SN model atmospheres problem, we will discuss some intermediate methods for studying SN geometry in a parameterized way. These methods are crucial for understanding the scale and class of deviation from spherical symmetry which could manifest in observed spectra. The general guidelines derived form a sort of SN geometry primer, useful for making sense of the SN model atmosphere solutions. Their discussion also incrementally moves us closer to the full solution of the problem.

The key difference between the formulation of the model atmospheres problem in SNe with respect to other stars is that the initial SN explosion imparts tremendous kinetic energy (about 10^{51} erg) to the ejecta, resulting in a macroscopic velocity field with a large velocity gradient. The ejecta velocities exceed the local thermal velocities in the gas by a factor of about 10^3. By contrast, ordinary stellar structure is governed (to first order; neglecting convection, differential rotation, and magnetic field effects) by a condition of hydrostatic equilibrium, where internal pressure is balanced by gravity. This condition is absent from SN envelopes, which we take to be in free expansion a short time (hours to days) after explosion and beyond.

Macroscopic velocity fields manifest themselves in the model atmospheres problem through the effects that they have on the calculation of the ambient radiation field. As different parts of the envelope move with respect to one another (in different inertial frames) radiation emitted from one point Doppler shifts with respect to the matter as it propagates to another point. This shift complicates the equation governing the radiation field by coupling spatial, angle, and wavelength terms. When the assumption of spherical symmetry is relaxed for 3D modelling purposes, solving this equation for arbitrary matter distribution and radiation fields becomes intractable, mostly because of problems of computational capacity.

Surprisingly, large velocity gradients themselves can provide us with an escape hatch which we may use, provided we are willing to neglect some modest radiation transfer effects. This escape hatch, the *Sobolev approximation* (Sobolev, 1947), becomes especially attractive considering the more obvious solution of decomposing the radiation field into spherical harmonics at all points for all wavelengths throughout an expanding envelope. As long as the surrendered transfer effects are not critical for producing clear, realistic signatures of 3D phenomena in emergent spectra, we may proceed through Sobolev's escape hatch to study 3D SN models with confidence.

In this chapter, we provide a basic introduction to the formalism we use to confront

3D SN spectrum modelling, including only those concepts and nomenclature germaine to this particular situation. We also discuss the explicit and implicit assumptions of the formalism, and point out where these assumptions may be somewhat inadequate.

2.1 The Radiation Transfer Equation

The radiation transfer equation (RTE) is a Boltzmann transport equation for photons except that in place of the phase space density of particles $f(\vec{q}, \vec{p}, t)$, an energy-like quantity called the *specific intensity* $I(\vec{r}, \hat{n}, \lambda, t)$ is used. The equation may be derived from basic statistical mechanics principles (Mihalas, 1978; Collins, 1989). The 3D time-independent form of the RTE is

$$\hat{n} \cdot \vec{\nabla} I(\vec{r}, \hat{n}, \lambda) = \eta(\vec{r}, \hat{n}, \lambda) - \chi(\vec{r}, \hat{n}, \lambda) I(\vec{r}, \hat{n}, \lambda). \tag{2.1}$$

For now we include a brief discussion of the terms included in the RTE, and defer details about their computation for later on. We include time-dependence in their definitions, but neglect it elsewhere. We will return to the issue of time-dependence later.

- $I(\vec{r}, \hat{n}, \lambda, t)$. Consider a quantity of radiation dE in the form of photons with wavelengths in the band $(\lambda, \lambda + d\lambda)$ passing through a point $\vec{r}$ in the direction $\hat{n}$, through an element of area dS and into a solid angle element $d\Omega$ about the unit normal $\hat{dS}$ during a time interval $(t, t + dt)$. Figure 2.1 illustrates the geometry. The specific intensity is defined according to the relation

$$I(\vec{r}, \hat{n}, \lambda, t) = \frac{dE(\vec{r}, \hat{n}, \lambda, t)}{\hat{n} \cdot dS \; dt \; d\lambda \; d\Omega}. \tag{2.2}$$

Specific intensity has CGS units of erg cm^{-2} s^{-1} Å^{-1} ster^{-1}.

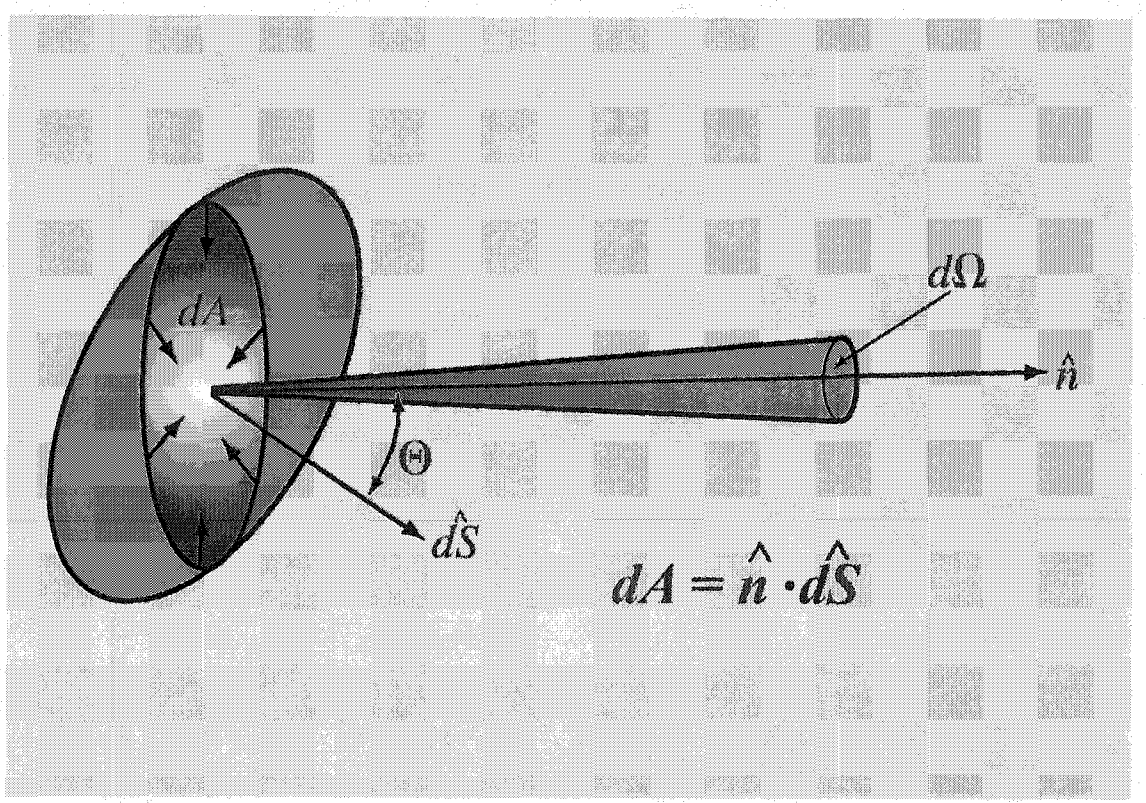

Figure 2.1: Geometry defining the specific intensity. This quantity is a measure of the energy passing through a unit surface into a cone of small solid angle around a given direction.

• $\eta(\vec{r}, \hat{n}, \lambda, t)$. The *monochromatic emissivity* is a measure of the amount of energy added to the radiation in a differential volume element dV in a wavelength band $(\lambda, \lambda + d\lambda)$ in the solid angle $d\Omega$ about the direction $\hat{n}$ during a time interval $(t, t + dt)$:

$$\eta(\vec{r}, \hat{n}, \lambda, t) = \frac{dE(\vec{r}, \hat{n}, \lambda, t)}{dV\ dt\ d\lambda\ d\Omega}. \tag{2.3}$$

Monochromatic emissivity has CGS units of erg cm^{-3} s^{-1} Å^{-1} ster^{-1}. The emissivity contains both scattered and locally emitted radiation contributed to the beam.

• $\chi(\vec{r}, \hat{n}, \lambda, t)$. The *monochromatic extinction* coefficient represents subtractions from the energy supplied by a specific intensity beam in a particular wavelength band. Hence, its CGS units are cm^{-1}.

At this point we define an auxiliary quantity called the *source function* which is simply the ratio of the emissivity to extinction coefficient:

$$S(\vec{r}, \hat{n}, \lambda) = \frac{\eta(\vec{r}, \hat{n}, \lambda)}{\chi(\vec{r}, \hat{n}, \lambda)}. \tag{2.4}$$

The CGS units of the source function are the same as specific intensity.

Now if the coefficients $\eta(\vec{r}, \hat{n}, \lambda)$ and $\chi(\vec{r}, \hat{n}, \lambda)$ (or alternatively the source function) are somehow supplied and the initial conditions for $I(\vec{r}, \hat{n}, \lambda)$ are given, then the RTE may be solved. In practice, the RTE at some point $\vec{r}$ is solved for each member of a collection of beams intersecting the point from many different directions, as depicted in Figure 2.2.

For a single beam, we may parameterize the RTE in terms of the beam-path coordinate s:

$$-\frac{d}{ds} I(\vec{r} - \hat{n}s, \lambda) = \eta(\vec{r} - \hat{n}s, \lambda) - \chi(\vec{r} - \hat{n}s, \lambda) I(\vec{r} - \hat{n}s, \lambda). \tag{2.5}$$

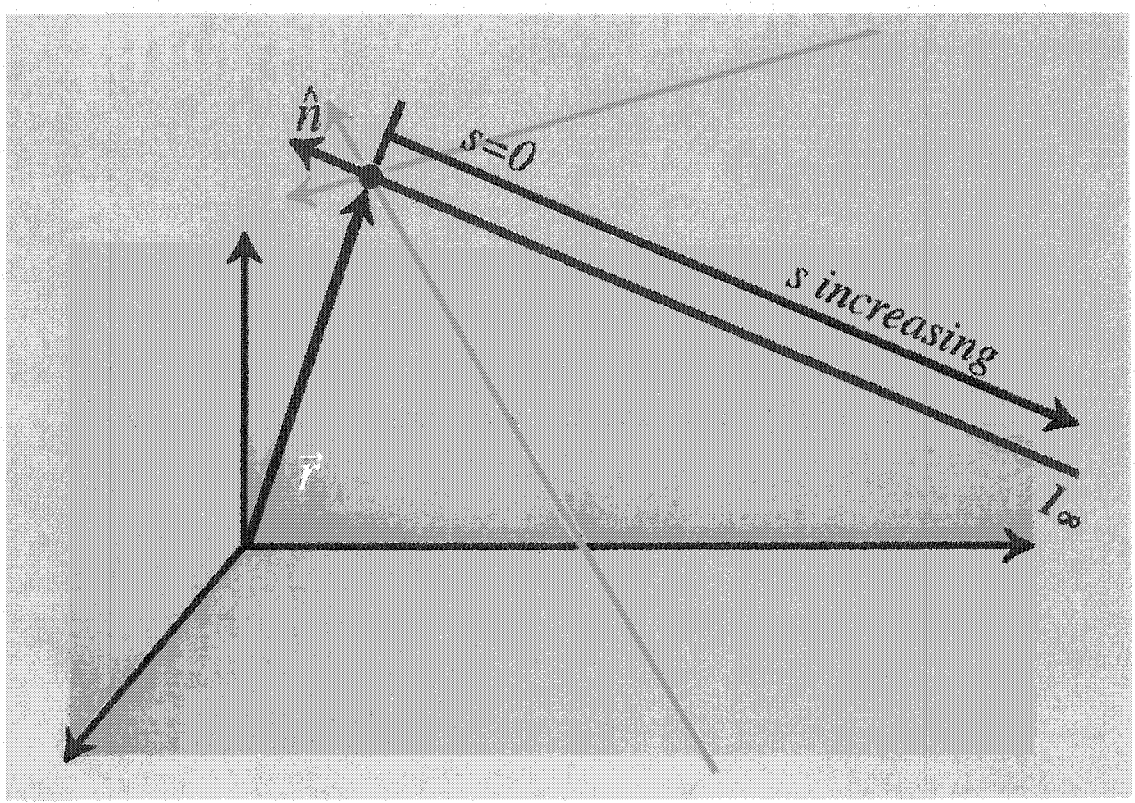

Figure 2.2: Geometry for the formal solution. The RTE for a large number of beams (three are shown) intersecting $\vec{r}$ is solved in order to obtain the radiation field incident on that point. For each beam, we take the beam-path coordinate s to be increasing backward with respect to the direction $\hat{n}$.

The left-hand side of Equation (2.5) incurs a minus sign since we take the beam-path coordinate to increase *backward* along the beam from the point $\vec{r}$. This equation is a first order linear differential equation so it may be solved with the use of an integrating factor. We label the intensity directed at the point $\vec{r}$ from $s = \infty$ as $I_\infty(\vec{r}, \hat{n}, \lambda)$, the initial condition on $I(\vec{r}, \hat{n}, \lambda)$. We may then write the solution,

$$\begin{aligned} I(\vec{r}, \hat{n}, \lambda) &= I_\infty(\vec{r}, \hat{n}, \lambda) \exp\Big(-\int_0^\infty ds\ \chi(\vec{r} - \hat{n}s, \lambda)\Big) + \\ &\int_0^\infty ds\ \Big[\eta(\vec{r} - \hat{n}s, \lambda) \exp\Big(-\int_0^s ds'\ \chi(\vec{r} - \hat{n}s', \lambda)\Big)\Big] \end{aligned} \tag{2.6}$$

The process of evaluating Equation (2.6) for given emission and extinction coefficients is known as the *formal solution.* This process is complicated by three problems.

[1] In general, the full RTE is expressed in a mixture of frames (Auer, 2003). The left-hand side of Equation (2.1) is most naturally expressed in the observer frame, since the wavelength and direction of a specific intensity beam are constant in this frame. However, the coefficients on the right-hand side of Equation (2.1) are described more naturally in the comoving frame (at rest with respect to the matter in all frames simultaneously), since in this frame they are generally smooth functions of angle. Boosting these quantities into the observer frame erases this expiditing quality.

[2] Solving the RTE for one beam generally requires the solutions from other beams if scattering of radiation is included. This requires that a system of equations be set up on a grid of spatial, angle, and wavelength coordinates. On a 3D spatial grid consisting of $100 \times 100 \times 100$ space points, 100 angles, and 10^6 wavelength points, matrix inversion will take $O(10^{42})$ operations! This is avoided through less expensive, iterative techniques derived in the 1D case, but which are difficult to scale to 3D.

[3] The full solution to the RTE in the general case requires that the integrals in Equation (2.6) be evaluated along the entire length of the beam. Furthermore, the angular variation of the radiation field arriving at a point is important (even if

it is simply averaged), particularly in 3D. In practice, however, the emissivity and extinction coefficients are known only at discrete points, and in reality a correct solution requires that they be known (literally) at all points along all beams. Clearly, spatial, angle, and wavelength resolution must be maximized. Some interpolation techniques can mitigate this problem, but they introduce problems of their own.

These obstacles in the path to solutions of the model atmospheres problem are well-known. The complexity scale required to overcome them is magnified in the case of moving 3D model atmospheres. This suggests that we might make some progress if we adopt a sensible approximation method for solving the problem until the method can be discarded. The technique we choose is well-suited to SN models; the Sobolev approximation, which is both elegant and useful. This method takes advantage of the large scale velocity fields present in the model atmosphere to confine the line transfer problem to physically small scales where its solution is trivial.

In this work we adopt the assumption of pure time-independence. This is not strictly applicable, especially in the moving atmospheres case. While the expansion timescale for a SN envelope is on the order of weeks, the radiation diffusion timescale is on the order of hours to days. Though the diffusion timescale is shorter than the expansion timescale, the two are uncomfortably close to one another. But taking time-independence into account would increase the complexity of the problem when it might not be essential. Our focus is line transfer and line formation in model SN atmospheres, where we regard time-dependence effects as relatively minimal.

2.2 Basic Assumptions and Consequences

The Sobolev method (Sobolev, 1947) of radiative transfer is an example of an *escape probability* technique. It provides approximate solutions to the transfer problem in the case of atmospheres governed by large scale velocity fields with large velocity

gradients. An example of a more accurate method is the comoving frame formalism, as employed in the multipurpose stellar atmosphere modelling code PHOENIX. The Sobolev approximation is usually applied for line transfer problems, though it has been generalized in order to account for continuum effects and polarization (Jeffery, 1989). In fact, several restatements and refinements of the technique have been published (e.g. Castor, 1970; Rybicki & Hummer, 1978; Pavlakis & Kylafis, 1996).

The Sobolev approximation has been used for calculating synthetic spectra for stars with strong winds, radiatively driven winds in accretion disks, and most notably for synthetic SN spectra. Here we present a brief description of the Sobolev approximation, but only as it applies to the situation of line formation in SN envelopes.

2.2.1 Assumptions – The Elementary Supernova Model

For our model SN, we adopt the so-called elementary supernova (ES) paradigm as described by Jeffery & Branch (1990). The simplest conceptual picture of a SN a few days to weeks after explosion consists of an optically thick core or photosphere surrounded by an extended line-forming atmosphere. This picture describes the *photospheric phase* of SN evolution. The techniques described here are most applicable to this phase.

The core is a region of high temperature and ionization resulting in part from the deposition of γ-rays produced by the radioactive decay of freshly synthesized iron-peak elements. In the ES model, we take the core to have a sharply defined interface with the line forming region. This core surface may have a geometry that is spherical, or it may be any other closed surface. In reality, the photosphere geometry arises from the ejecta structure, temperature, and γ-ray-deposition rates. Furthermore, the real photosphere is not so sharply defined; its boundary depends on the wavelength at

which its shape is considered. The core forms a lower boundary to the line forming region, and we assume a diffusive boundary condition. That is, the core is a Lambert radiator, emitting Planckian radiation at some specified temperature.

The initial hydrodynamics of the explosion terminate within a day or so after explosion, so the ejecta settle into homologous expansion. In the ES model, the velocities are high but not so high as to be relativistic (on the order of 10^4 km s^{-1}, but this restriction can be removed – Jeffery, 1993). As the entire SN expands, its density drops as t^{-3} and the core boundary recedes into the depths of the SN ejecta profile. Once the core has become optically thin (at a few months after explosion), the SN has entered the *nebular* phase and the ES description no longer applies.

2.2.2 The Sobolev Approximation and the ES Model

Consider a point R moving with the matter in an ES atmosphere. The velocity field is homologous, so all other points recede from R at rates proportional to their distances from R, as depicted in Figure 2.3. The velocity field relative to R is direction-independent, so points with the same recession rates fall on spheres centered on R. We call the loci of these points *common-point* (CP) velocity surfaces for R.

A monochromatic beam of radiation is directed at R from some other point in the atmosphere. We label the wavelength of this beam in the observer frame moving with R as λ_R. The emissivity and extinction coefficients along the beam-path govern the intensity of the beam on its way to R.

We now define the *comoving frame* as the frame in which, except for the thermal and microturbulent velocities of the gas, the matter is at rest. In this frame, as the beam propagates it redshifts with respect to the matter. This effect is purely a consequence of the Doppler shift imposed by the velocity field shown in Figure 2.3. The observer at R ascribes the wavelength λ_R to the beam, but another observer at

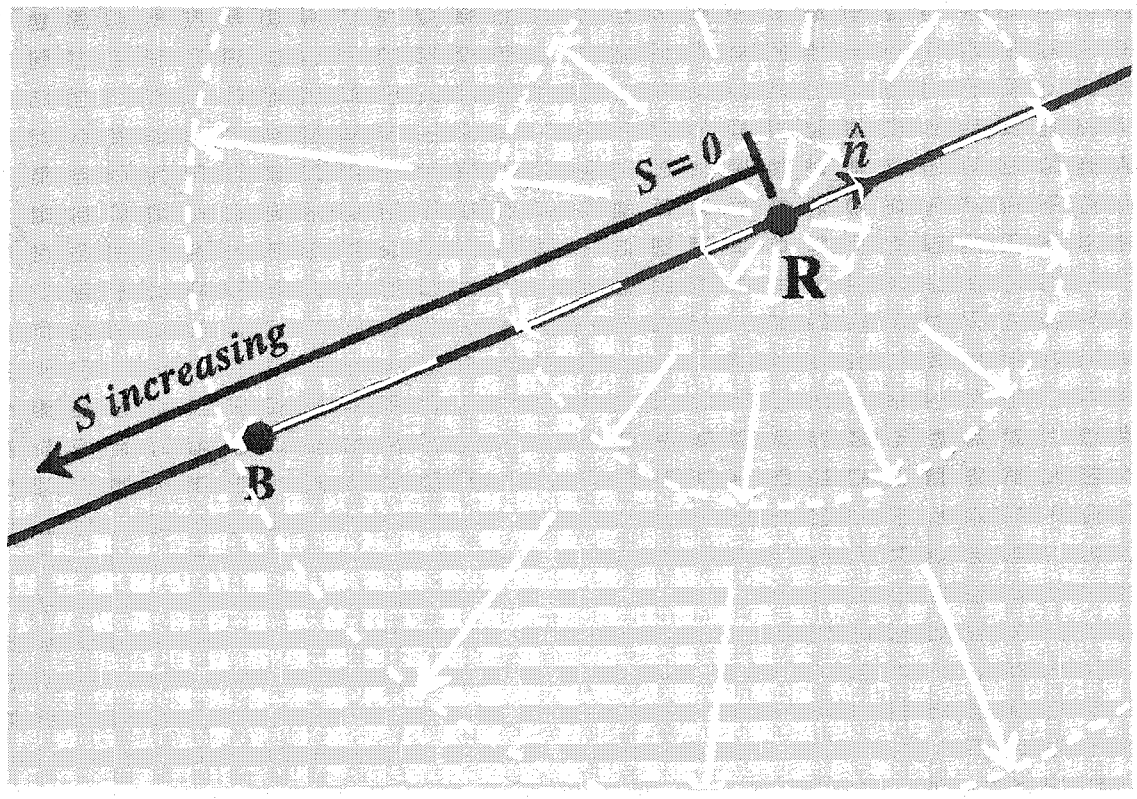

Figure 2.3: Observer frame picture of the ES atmosphere. From the observer frame moving with the point R, the velocity field moves points away from R at rates proportional to distance from R. The matter that the beam encounters as it propagates toward R moves at an increasingly slower and slower rate with respect to R.

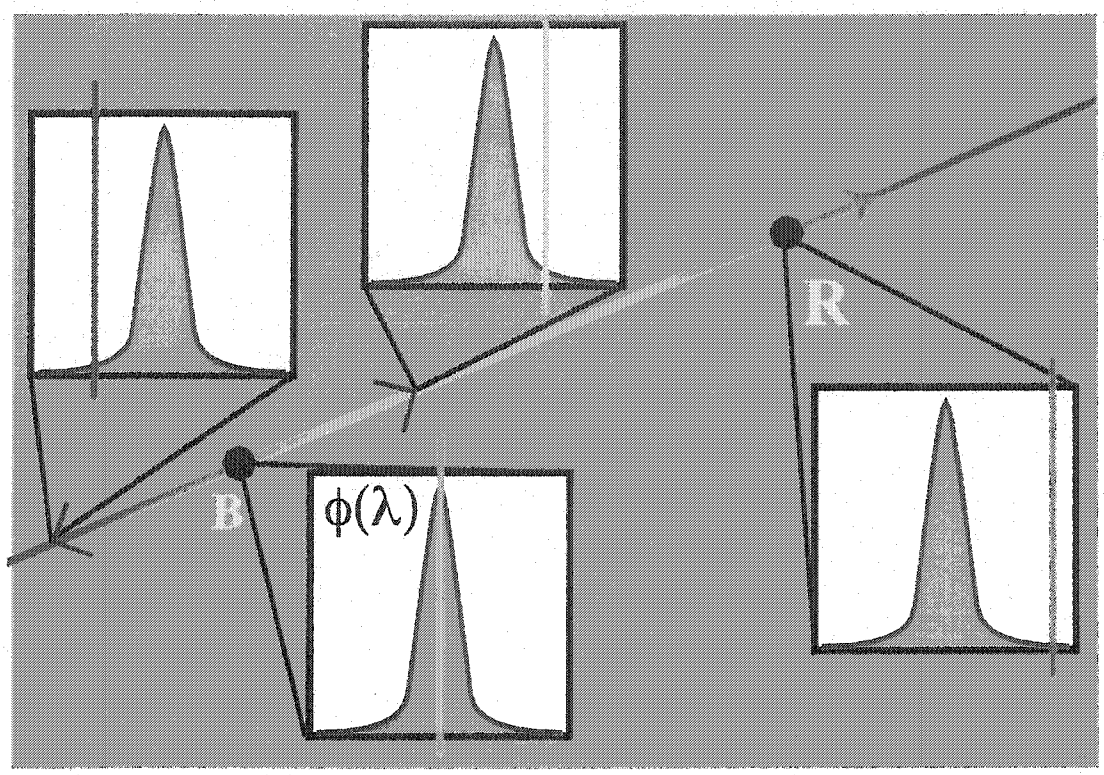

Figure 2.4: Comoving frame picture of the ES atmosphere. In this frame, which is simultaneously at rest with the matter everywhere, the beam redshifts as it propagates. This brings it into resonance with each wavelength at only one point along its length. If that wavelength is in a line, the beam may interact with the line there. Line interactions are confined to beam segments instead of along the entire beam.

B ascribes λ_B. These two wavelengths are related by the first order Doppler formula,

$$\lambda_R = \lambda_B(1 + \Delta v/c) \tag{2.7}$$

where Δv is the velocity separation of the two points B and R. In the comoving frame, the monotonic nature of the velocity field guarantees that the beam wavelength equals λ_R only at the *resonance point* R. The same holds for the wavelength λ_B and its resonance point B. Figure 2.4 depicts the comoving frame situation corresponding to the observer frame shown in Figure 2.3.

Now suppose that in this atmosphere, there is a single atomic line of interest

centered at λ_B. That is, the extinction coefficient is given at the point $\vec{r}$ as

$$\chi(\vec{r}, \hat{n}, \lambda) = \bar{K}_B(\vec{r}, \hat{n})\ \phi_B(\lambda) \tag{2.8}$$

where $\bar{K}_B(\vec{r}, \hat{n})$ is the total integrated line opacity (determined by the matter state variables at $\vec{r}$) and $\phi_B(\lambda)$ is the normalized line profile function. As the beam propagates through the atmosphere, it first resonates with wavelengths in the blue wing of the line, interacting weakly with the line there. It then shifts into the line core (where interaction is the strongest) and then into the red wing (where interaction is weak again). When the beam shifts into resonance with λ_R at R, the beam is *free-streaming* since it is out of the line. We call a region along the beam-path where photons interact with a line a *resonance region* of the line. In Figure 2.4, a resonance region is depicted between angle brackets along the beam-path as the beam interacts with the line profile shown.

The consequences of the Doppler shift on line transfer are clear. In a static line-dominated atmosphere, a beam that is in the line is always in the line, so the beam RTE is completely nonlocal. But in an ES atmosphere, interaction with a line is physically restricted to resonance regions – we need only solve the RTE in these regions since the beam photons free-stream between line interactions.

Furthermore, the larger the velocity gradient, the smaller the resonance regions become. The smaller the resonance regions, the more acceptable it becomes to treat the total integrated line opacities as constant across the resonance regions. In particular, we can approximate these quantities by their line-center resonance point values.

The choice of an homologous velocity field admits a further simplification. In this case, the extent of a resonance region for a given line through a given point is *direction-independent.* Since the Doppler shift incurred from homology is irrotational, each beam intersecting a point encounters the same line profile function no matter

what direction it comes from.

These two implications mean that the solution to the RTE through a resonance point becomes trivial. For a beam passing through a resonance region centered at $s_\star$ with a wavelength $\lambda_\star$, the solution to the RTE may be written

$$I(s_\star^r, \lambda_\star) = I(s_\star^b, \lambda_\star)e^{-\tau(s_\star,\lambda_\star)} + S(s_\star, \lambda_\star)(1 - e^{-\tau(s_\star,\lambda_\star)}). \tag{2.9}$$

The intensity entering the blue side of the line is given by $I(s_\star^b)$ and the emergent intensity on the red side is given by $I(s_\star^r)$. In Equation 2.9, we have introduced the *Sobolev optical depth* $\tau(s_\star, \lambda_\star)$, the integrated extinction coefficient for the line centered at $\lambda_\star$ as computed at $s_\star$:

$$\tau(s_\star, \lambda_\star) = \int_{-\infty}^{\infty} ds\ \bar{K}_\star(\vec{r})\phi_\star(s(\lambda)) \tag{2.10}$$

We will return to the problem of computing Sobolev optical depths from the matter state variables in subsequent chapters. In the Sobolev picture, specific intensity along a beam is unchanged between line interactions, but goes through discontinuous jumps at line center resonance points with nonzero Sobolev optical depth.

Informally, the Sobolev approximation has turned the line profile functions into Dirac δ-functions. Hence, resonance points are practically at $\Delta s = \pm\infty$ to one another. Technically this is not the case, and some work has been done to include the effects of line overlap into the Sobolev approximation (Pavlakis & Kylafis, 1996). However, this problem presents itself mostly in closely situated, strong (i.e.$\tau >>>$ 1) lines where the line optical depth accumulated in the line wings becomes high. A further problem is that using constant integrated line opacities across resonance regions could introduce errors into the emergent intensities. If a great number of interactions with strong lines occurs, these errors could build up.

The Sobolev approximation reduces the transfer problem to calculating optical depths and radiatively coupling loci of resonance points. The transfer problem under the Sobolev approximation is thus purely geometrical in nature. To find the specific intensity $I(\vec{r}, \hat{n}, \lambda)$, we begin with the inital intensity directed at $\vec{r}$ from $s = \infty$. For a beam intersecting the core, this initial intensity is just the photospheric specific intensity. For other beams, this is zero.

As s decreases along the beam line to the point $\vec{r}$, its intensity remains unchanged between line interactions, and changes at resonances. For all beams arriving at $\vec{r}$ for the same wavelength, these resonances will fall on CP surfaces situated to satisfy the Doppler resonance condition expressed in Equation (2.7): spheres. These concentric CP surfaces for a few lines are depicted in 3D (with an arbitrary matter distribution in the form of clumps), in Figure 2.5. It is apparent then that the bluer lines *feed* redder lines in homologous expansion.

To find the emergent intensity for some observer in some direction, we again find surfaces of common Doppler shift with respect to this observer frame. We note that the plane perpendicular to the line of sight that bisects the atmosphere has no shift toward or away from the observer. Homology dictates that surfaces with common velocity relative to the observer form planes perpendicular to the line of sight. We call these planes *common-direction* (CD) surfaces. As depicted in Figure 2.6, for a given wavelength, resonance points fall on these CD surfaces. To compute the emergent flux in the direction of the observer, we may recursively apply Equation (2.9) starting at the far side of the envelope and follow beams through blue lines toward red toward the observer. Doing this for a number of such *characteristic beams* delivers the flux in a given wavelength toward the observer.

The procedure for computing a synthetic spectrum from a given distribution of line optical depth is thus quite simple. After the optical depths are (somehow) specified, the radiation field everywhere is calculated using the results of the Sobolev

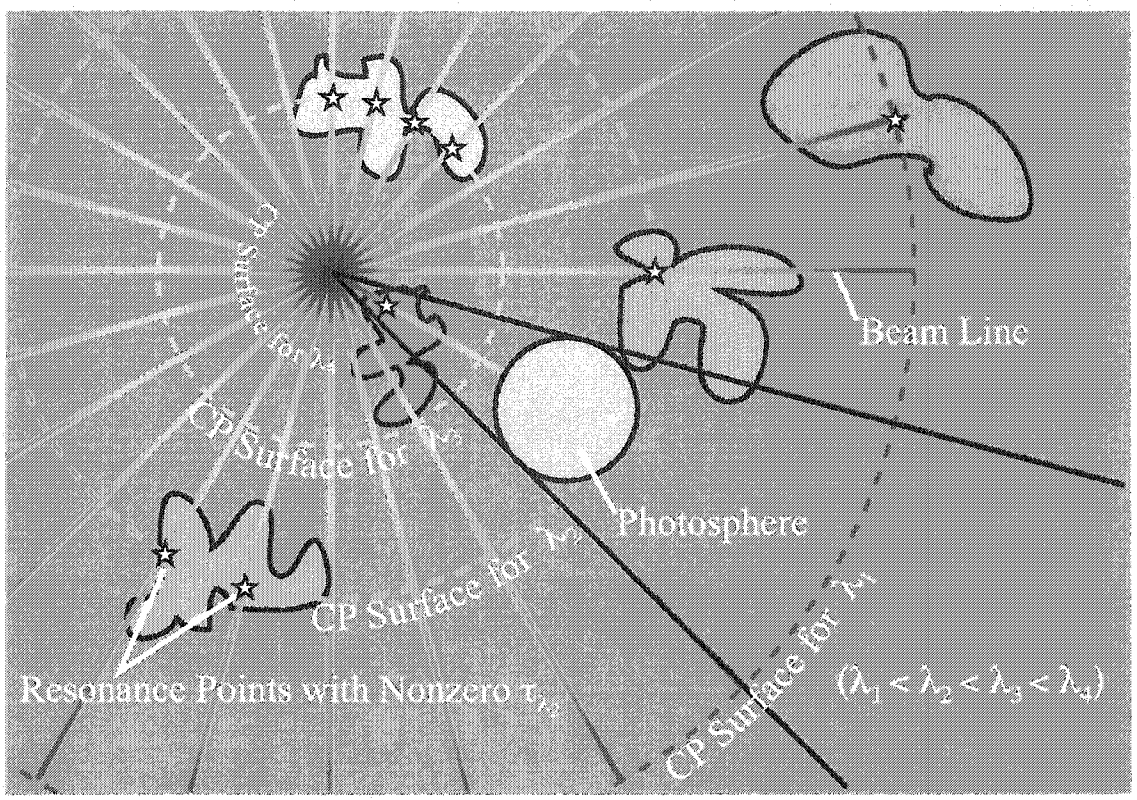

Figure 2.5: CP surface in 3D atmosphere geometry. The CP surfaces are spheres centered on the point in question. Their radii are determined by the first order Doppler formula and the wavelengths of bluer lines which feed the point scattered line radiation.

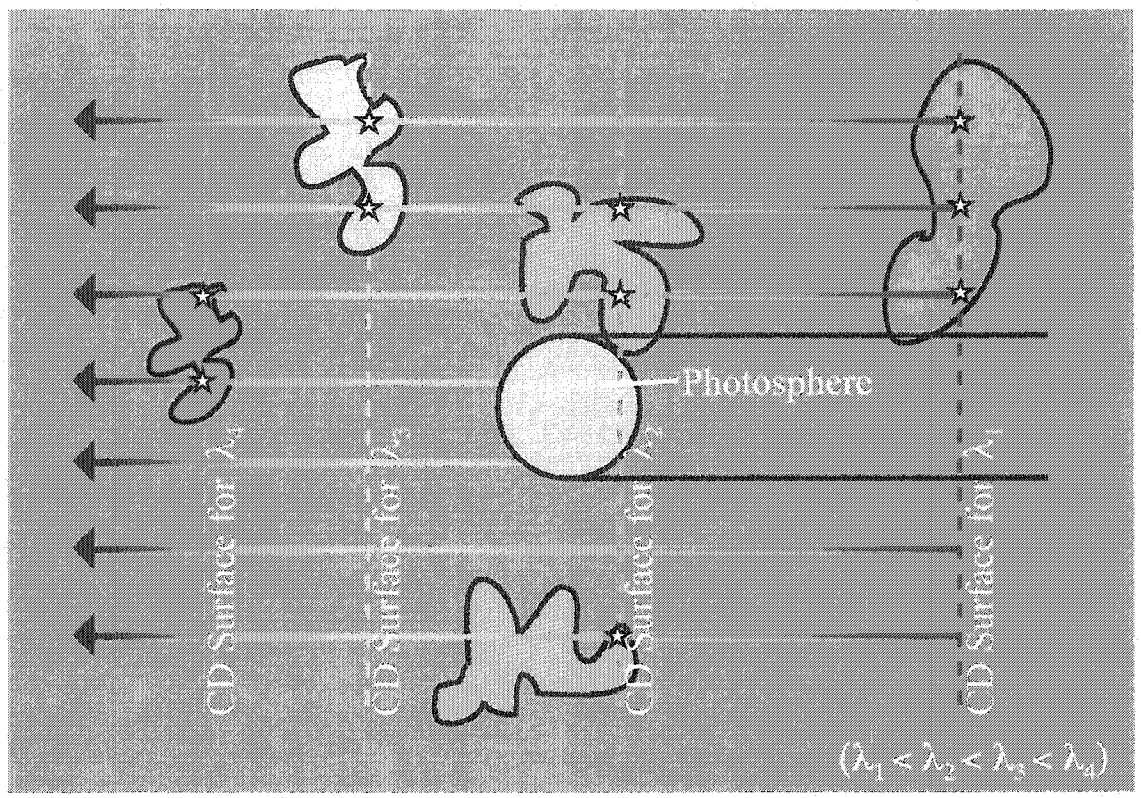

Figure 2.6: CD surface in 3D atmosphere geometry. In homology, the surfaces with constant velocity with respect to an observer at ∞ are planes perpendicular to the line of sight. We integrate the RTE using the Sobolev approximation with interaction points falling upon these planes for given lines.

approximation. Observer directions are chosen, and emergent flux in each of these directions is computed for each wavelength, generating a synthetic spectrum for each observer.

Chapter 3

Line Formation in 3D SN Models

Based on a set of 111 SNe Ia, Richardson et al. (2002) derive a mean peak absolute magnitude of $\langle M_B \rangle = -19.46$ and a modest intrinsic dispersion of $\sigma = 0.56$ (much of which is due to errors in photometry and distances). This combination of a very high luminosity and a very low intrinsic luminosity dispersion makes these events good standard candles – objects of known intrinsic brightness whose observed fluxes may be used to derive distances. Through the use of an empirically determined relationship between peak brightness and light curve morphology (e.g. Phillips, 1993), this dispersion can be reduced further to make SNe Ia even better standard candles. The homogeneity in luminosity of these objects makes them useful for plotting Hubble curves to constrain cosmological parameters (Perlmutter et al., 1999; Riess et al., 1998).

A large fraction of SN Ia spectra look alike. This subset of SNe Ia we call *spectroscopically normal* or Branch-normal, after the criteria set forth by Branch et al. (1993, hereafter BFN); those events with spectra resembling those of SNe 1981B, 1989B, 1992A, and 1972E. By contrast, a SN Ia is called *spectroscopically peculiar* if it has feature strengths and expansion velocities different from the norm; such as SN

1991T (extremely weak Si II), or 1991bg (prominent Ti II). BFN considered a large set of SN Ia spectra and concluded that 83% to 89% of SNe Ia are spectroscopically normal. Since then, the occurence ratio of normal to peculiar SNe Ia (and its implications for progenitor models) has become the subject of much debate (e.g. Li et al., 2001b; Branch, 2001). Nevertheless, it is clear that a good fraction of SNe Ia are spectroscopically normal.

The luminosity/spectroscopic homogeneity of normal SNe Ia suggests a standard progenitor. The "standard model" of a SN Ia is the explosion of a nearly Chandrasekhar-mass carbon/oxygen (C/O) white dwarf brought on by the accretion of matter from a donor companion. In some scenarios, the explosion is a *deflagration*, meaning that the burning front propagates through the white dwarf at subsonic speeds. In others, the explosion is a supersonic *detonation* of the white dwarf. Still other models are a mixture of the two, such as delayed detonation where a deflagration wave becomes a detonation wave at some specified transition density.

In 1D models, the burning physics must be parameterized; the real flame surface must be an inherently 3D phenomenon. Despite this, many 1D explosion models result in synthetic spectra consistent with observed ones (notably, deflagration model W7 – Nomoto et al., 1984; Branch et al., 1985). Still, recent advances in computer science permit explosion modellers to try to include the 3D nature of the flame front in their simulations, in an effort to simulate more physically the explosions of white dwarfs (Khokhlov, 2000; Reinecke et al., 2002; Gamezo et al., 2003, – all deflagrations).

One feature of these new 3D deflagration models is large scale mixing of ashes with fuel in an inhomogeneous way. Plumes of burned material shoot upward from the star's center, while unburned material sinks down between the plumes. But since none of the models has been carried forward to the free expansion phase, it is not clear that these characteristics will persist to make spectroscopic signatures in the photospheric phase.

Even so, the models motivate us to consider some general questions about 3D line formation in SNe in general, and in spectroscopically normal SNe Ia in particular. The answers will guide explosion simulations toward those models which produce normal synthetic SN Ia spectra. The most obvious question to ask relates to the issue of spectroscopic homogeneity in normal SNe Ia. What scales and classes of nonsphericity may occur in SN Ia atmospheres which do not undermine spectroscopic homogeneity? More generally, what kinds of line profile phenomena can we expect from model SN atmospheres with nonsphericities in them?

Inherent in the discussion of the compatibility of nonsphericity with spectroscopically normal SNe Ia is an assumption about the overall geometry of these events. Making an assumption is inescapable, unless a spectroscopically normal SN Ia is observed in proximity so that its geometry may be resolved. One possible assumption (the "global sphericity" assumption) is that normal SNe Ia are spherically symmetric on large scales and their deviations are so "minor" that they may fail to contribute observable signatures to flux spectra. An alternative is to assume that SNe Ia are all nonspherical in a global way (e.g., they are all dominated by oblate ellipsoid geometry), and that the division between normals and peculiars reflects a distribution of random orientations. The most radical assumption is to suppose that normal and peculiar SNe Ia come from completely disparate progenitor scenarios, but this moves us away from the standard model without clear supporting evidence. For the sake of discussion, we adopt the first assumption and try to constrain what the term "minor deviation" means. How large can perturbations in SN atmospheres be that fail to undermine spectroscopic homogeneity?

Even if the assumption of global sphericity eventually proves incorrect, the results will still be interesting for two reasons. First, the nonsphericity constraints apply in general to any class of SN characterized by a certain spectroscopic alikeness. Second, the results are also interesting from a general line formation point of view, and cannot

be obtained through mere intuition.

We begin by considering what SN Ia spectra might look like if the assumption of spherical symmetry is dropped. This motivates us to consider some general questions about line formation in 3D that provide us with some illustrative examples. In the end, we produce a kind of constraint on the size that "clumps" of material can have and still preserve spectroscopic homogeneity.

3.1 Spectra from Clumpy SNe Ia

Our first task will be to modify the direct analysis code `Synow` in such a way that we can begin to address the question of what SN Ia spectra look like if their atmospheres have nonsphericities present. A complete description of `Synow` and its feature set appears in Fisher (2000). Building on the discussion of the Sobolev method described in Chapter 2, we will discuss here only the background necessary to understand the modifications made to allow `Synow` to produce spectra from model envelopes without spherical composition symmetry.

3.1.1 Synow and ClumpySyn

In its simplest form, `Synow` relies on all of the assumptions of the ES model outlined in Chapter 2. An homologously expanding envelope is assumed, and line formation takes place in an atmosphere surrounding a sharply defined photosphere which provides continuum radiation. Line formation is treated under the Sobolev approximation. Since `Synow` is a direct analysis code for empirical spectrum fitting, Sobolev line optical depth is *parameterized* as opposed to *derived* from model atmosphere matter state variables. We begin by defining which quantities are parameterized and the method by which this is accomplished.

In the ES model implementation of the Sobolev approximation, line optical depth for an atomic transition from a lower level l to an upper level u is given by (Jeffery & Branch, 1990)

$$\tau_{lu} = \frac{\pi e^2}{m_e c} f_{lu} \lambda_{lu} n_l t \Big(1 - \frac{g_l n_u}{g_u n_l}\Big). \tag{3.1}$$

Here, f_{lu} is the oscillator strength of the transition, λ_{lu} is its wavelength, n_u and n_l are the electronic level populations of its upper and lower states (g_u and g_l are the corresponding statistical weights), t is time since explosion, and the other symbols have their usual meanings. In this case, the matter state variables of interest are the atomic level populations n_u and n_l.

Generally, these state variables are related in a very complicated way, and there are literally millions of them to manage. A simplifying assumption is that of *thermodynamic equilibrium* (TE), in which case we may relate the level populations through a Boltzmann factor containing some excitation temperature. That is,

$$\frac{n_i}{n} = g_i \frac{\exp(-E_i/kT)}{Q(T)}, \tag{3.2}$$

where n is the total number density of the ion in question, $Q(T)$ is the ion's partition function, and E_i is the excitation energy of level i measured from the ground state. Hence, under the assuption of TE, Equation (3.1) becomes

$$\tau_{lu} = \frac{\pi e^2}{m_e c} g_l f_{lu} \lambda_{lu} n \frac{\exp(-E_l/kT)}{Q(T)} \Big(1 - \exp(hc/\lambda_{lu} kT)\Big). \tag{3.3}$$

Now we make an adjustment to the notation. The subscript l we now use to denote the l-th line of a set of L lines ($1 \leq l \leq L$). Dropping the u leads to no ambiguity, since the wavelength of the line λ_l always implies the same upper level. Replacing

constants, Equation (3.3) becomes

$$\tau_l = 2.292 \times 10^{-5} (gf)_l \lambda_l^A n t_d \frac{\exp(-E_l/kT)}{Q(T)} \Big(1 - \exp(\xi/\lambda_l^A T)\Big), \tag{3.4}$$

where $(gf)_l$ is the weighted oscillator strength (more often tabulated than f_l), λ_l^A is the transition wavelength in Angstroms, t_d is time since explosion in days, and the quantity $\xi \equiv 10^8 hc/k$. The atomic transition constants $(gf)_l$, λ_l and E_l for millions of lines of many ions are available in electronic format (Kurucz, 1993).

The assumption of TE permits us to determine Sobolev optical depth in a line given the number density of the parent ion and an excitation temperature. But for empirical analysis, the number density is an inconvenient quantity to work with. It is far easier to scale all the line optical depths of an ion relative to an arbitrarily chosen *reference line* optical depth τ_R. Though the optical depth in the reference line is prescribed *ad hoc*, its choice is generally chosen based on experience and on the published atlas of SN signatures (Hatano et al., 1999b). The scaling permits us also to dismiss the partition functions and the time in days since explosion from consideration:

$$\tau_l = \tau_R \frac{(gf)_l \lambda_l^A}{(gf)_R \lambda_R^A} \frac{\exp(-E_l/kT)}{\exp(-E_R/kT)} \frac{[1 - \exp(\xi/\lambda_l^A T)]}{[1 - \exp(\xi/\lambda_R^A T)]}. \tag{3.5}$$

Equation (3.5) encodes the line optical depth parameterization as a function of wavelength.

Since `Synow` is a 1D code, reference optical depth is spatially parameterized in terms of spherically symmetric functions of velocity relative to the origin (center) of the model SN, v,

$$\tau_R(v) = \tau_R(v_0)\psi_1(v). \tag{3.6}$$

The form of the radial contrast function $\psi_1(v)$ is purely a matter of choice, but is usually motivated by a decrease in density in the outer layers. An example would be an exponentially decreasing optical depth profile

$$\psi_1(v) = \exp([v_0 - v]/v_e), \tag{3.7}$$

where v_e is an e-folding velocity and it is clear that v_0 is a "reference velocity" where we anchor the $\tau_R(v)$ distribution. This is an example of a *single-component* optical depth profile.

An example of a *multi-component* optical depth profile would be a combination of single-component optical depth profiles such as

$$\tau_R(v) = \begin{cases} \tau_R(v_{0,1}) \exp([v_{0,1} - v]/v_{e,1}) & v_{l,1} < v < v_{u,1} \\ \tau_R(v_{0,2}) \exp([v_{0,2} - v]/v_{e,2}) & v_{l,2} < v < v_{u,2} \\ \vdots & \vdots \\ \tau_R(v_{0,n}) \exp([v_{0,n} - v]/v_{e,n}) & v_{l,n} < v < v_{u,n} \end{cases} \tag{3.8}$$

For either the single-component or multi-component optical depth distributions, spherical symmetry with respect to the origin supports an azimuthal symmetry with respect to any rotation axis through the origin. This simplifies the computation of the angle-averaged or mean intensity J arriving at a point in some wavelength λ:

$$J(v, \lambda) = \frac{1}{4\pi} \oint d\Omega(\hat{n})\ I(v, \hat{n}, \lambda) = \frac{1}{2} \int_{-1}^{+1} d\mu\ I(v, \mu, \lambda), \tag{3.9}$$

where $I(v, \mu, \lambda)$ is the intensity as given by the Sobolev approximation for the beam along the direction cosine μ. The cylindrical symmetry in both the optical depth

distributions and initial conditions on $I(v, \mu, \lambda)$ result in cylindrical symmetry in $I(v, \mu, \lambda)$.

A special case of Equation (3.9) occurs if there is no optical depth in lines bluer than the wavelength of interest at λ. The expression for the mean intensity is then determined entirely by the radiation arriving from the core. Assuming the core to also be spherically symmetric, we integrate over the projected surface area of the core as seen from v to obtain

$$J(v, \lambda) = W(v_{ph}; v) I_{ph}(\lambda), \tag{3.10}$$

where $W(v_{ph}; v)$ is the core's *geometrical dilution factor*, or the fraction of all solid angle the core subtends as seen from v. In spherical symmetry, it is just

$$W(v_{ph}; v) = \frac{1}{2}\left(1 - \sqrt{1 - v_{ph}^2/v^2}\right). \tag{3.11}$$

We call this case the *single scattering* case, when the specific intensity carries no terms from interaction with bluer lines. Two important limits of $J(v, \lambda)$ in the single scattering approximation are

$$J(v, \lambda) = \begin{cases} I_{ph}(\lambda)/2 & v = v_{ph} \\ v_{ph}^2 I_{ph}(\lambda)/4v^2 & v >> v_{ph} \end{cases} \tag{3.12}$$

`Synow` works by combining reference line optical depth profiles such as in Equation (3.8) with chosen excitation temperatures for individual ions. This determines spatial optical depth profiles for all lines of a given ion by means of Equation (3.5). Taking advantage of the azimuthal symmetry of the optical depth distribution, `Synow` constructs $J(v, \lambda_l)$ for all lines $1 \leq l \leq L$ where λ_l increases as l increases. `Synow` assumes *pure resonance scattering* (i.e., $S(\lambda) \equiv J(\lambda)$), further simplifying the Sobolev

integrations.

If we wish to modify Synow to handle spatial reference optical depth distributions without spherical symmetry, we generalize Equation (3.6):

$$\tau_R(\vec{v}) = \tau_R(\vec{v}_0)\psi_3(\vec{v}). \tag{3.13}$$

In analogy to the 1D case, $\vec{v}_0$ is an anchoring 3-velocity for the function $\tau_R(\vec{v})$ and the function $\psi_3(\vec{v})$ is a contrast function. Again, the form of $\psi_3(\vec{v})$ is a matter of choice, such as linear combinations of spherical harmonics times some constant.

Without an obvious symmetry in $\psi_3(\vec{v})$ to exploit, the assumption of cylindrical symmetry in the calculation of $J(\vec{v}, \lambda)$ is no longer supported, and Equation (3.9) must be generalized. In practice this is not as easy as it seems. To numerically evaluate the integral with a sampling error of only 1% requires 10^4 sampling beams. For 10^6 gridpoints, this means a total of 10^{10} sampling beams, each interacting with possibly several dozens of blueward line center resonance points along their length, *per line*. Furthermore, many of these beams will coincide with completely uninteresting directions, increasing inefficiency. An adaptive integration technique is not feasible; generally such techniques rely on the assumption that the function being integrated is well-behaved or smooth. We have no way of guaranteeing that this condition will be met for $I(\vec{r}, \hat{n}, \lambda)$ in 3D.

An obvious solution is to simply ignore other lines when computing $J(v, \lambda)$ for a given line. That is, we may approximate the value of $J(v, \lambda)$ by its single scattering value. This is a particularly poor assumption in the case of strong multiple scattering among closely spaced lines (a case which often occurs in the ultraviolet spectra of SNe Ia). For now, to see the first order effects, we will adapt Synow to use $\psi_3(\vec{v})$ functions and compute the mean intensities using the single scattering approximation. The Sobolev formal integration procedure described at the end of Chapter 2 is still used

to compute spectra, though the characteristic beams cannot be defined in a simple cylindrical $p-z$ coordinate system. Instead, a rectangular system $p_x - p_y - z$ is used to set up a grid of characteristic beams.

The particular form we choose for $\psi_3(\vec{v})$ is a superposition of spherical "clumps" of reference optical depth. To differentiate the code with these modifications (clumpy $\psi_3(\vec{v})$ instead of $\psi_1(v)$, single scattering instead of full multiple scattering source functions) from normal `Synow`, we designate this new code as `ClumpySyn`. We confine species to the clumps by setting the reference optical depths to zero outside of the clumps, but we use a radial profile ($\tau_R \propto \exp(-v/v_e)$) to determine optical depth within clumps.

3.1.2 `ClumpySyn` Spectra

An example of a clump configuration is shown in Figure 3.1. Here, we place an upper velocity boundary at 25000 km s^{-1}. We allow the clumps to overlap and have radii in velocity space between 5000 and 6000 km s^{-1}. The fraction of the volume taken up by clumps in the envelope (between the photosphere at 11000 km s^{-1} and the upper boundary) in Figure 3.1 is about 66%. Several such models were generated with different volume filling factors, and model output spectra were computed from several lines of sight with `ClumpySyn`. The photospheric and maximum velocities chosen are typical for a SN Ia near maximum light, but the clump size choices are arbitrary but motivated by 3D explosion modelling (Khokhlov, 2000).

Motivated by Figure 12 of Khokhlov (2000), we partition the clumps into two parts. In the inner part of the clumps, we place Fe II ions. In the outer part, we place intermediate mass ions (Si II, Ca II, S II). Outside the clumps, we place O I. The choice of these particular ions is partially motivated by a maximum light fit of SN 1994D Hatano et al. (1999a).

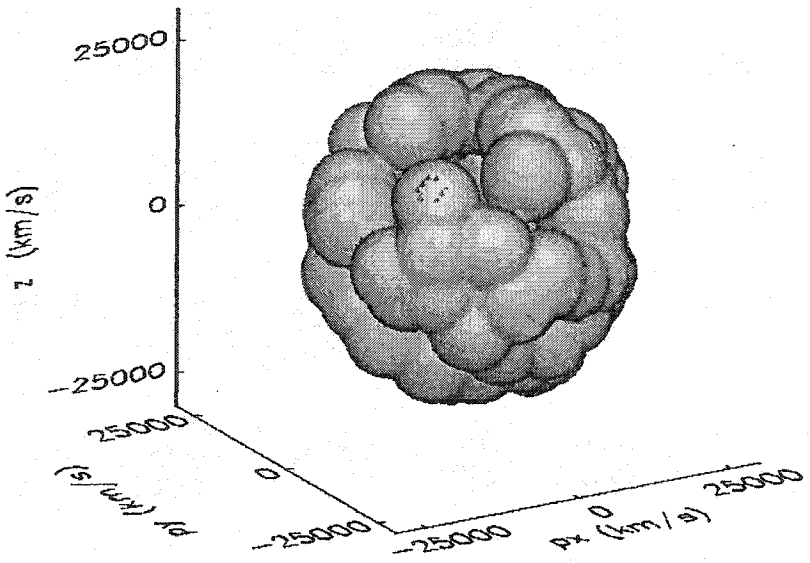

Figure 3.1: A sample clumpy model with 66% of the envelope filled.

Figures 3.2, 3.3, 3.4, and 3.5, present synthetic spectra from models with different envelope filling factors. Each graph displays four spectra, one each of four different lines of sight spaced 90 degrees apart about the equator. We note that higher volume filling factors cover the photosphere more effectively and the spectra are quite similar along all lines of sight. At lower filling factors, perspective-dependent spectroscopic diversity begins to creep in, particularly in absorption features.

3.2 Single Scattering Line Profiles in 3D Models

It is helpful to take a step back from the `ClumpySyn` spectra and consider some first principles of SN line formation in 3D models. The geometry described in Chapter 1 for the formation of P-Cygni lines assumes spherical symmetry in the expanding material. But in 3D, the line optical depth becomes thick or thin in a way that may not lend itself to intuition when considering line formation.

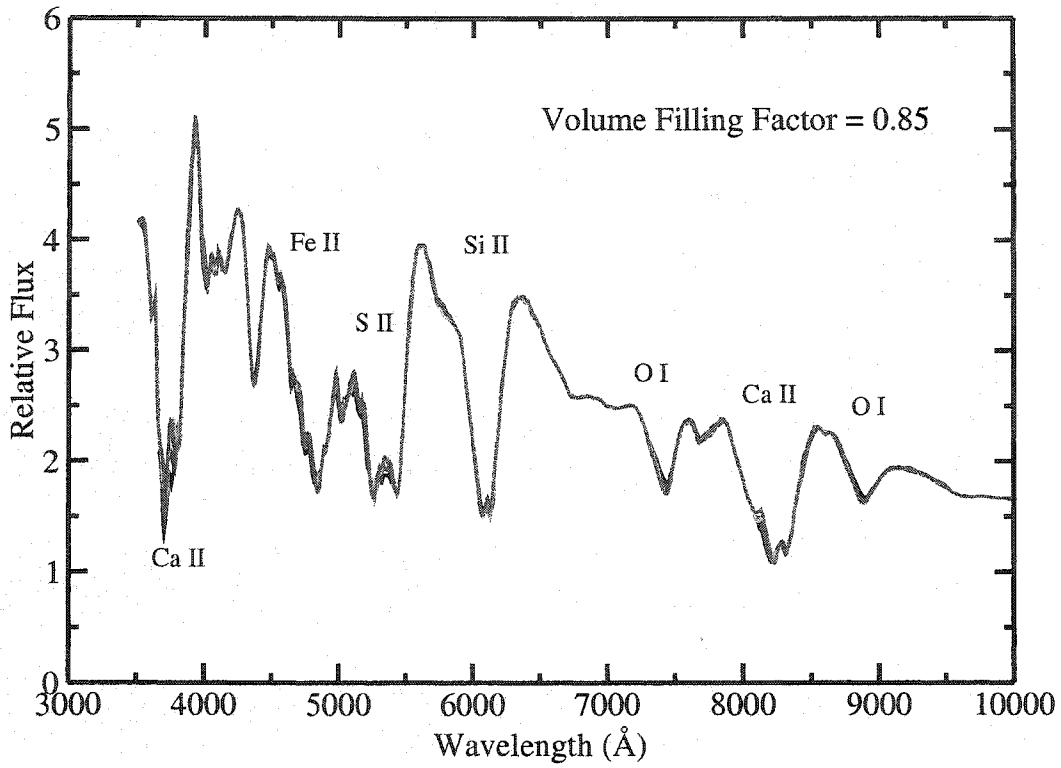

Figure 3.2: `ClumpySyn` calculations for volume filling factor 0.85. Four lines of sight are plotted together.

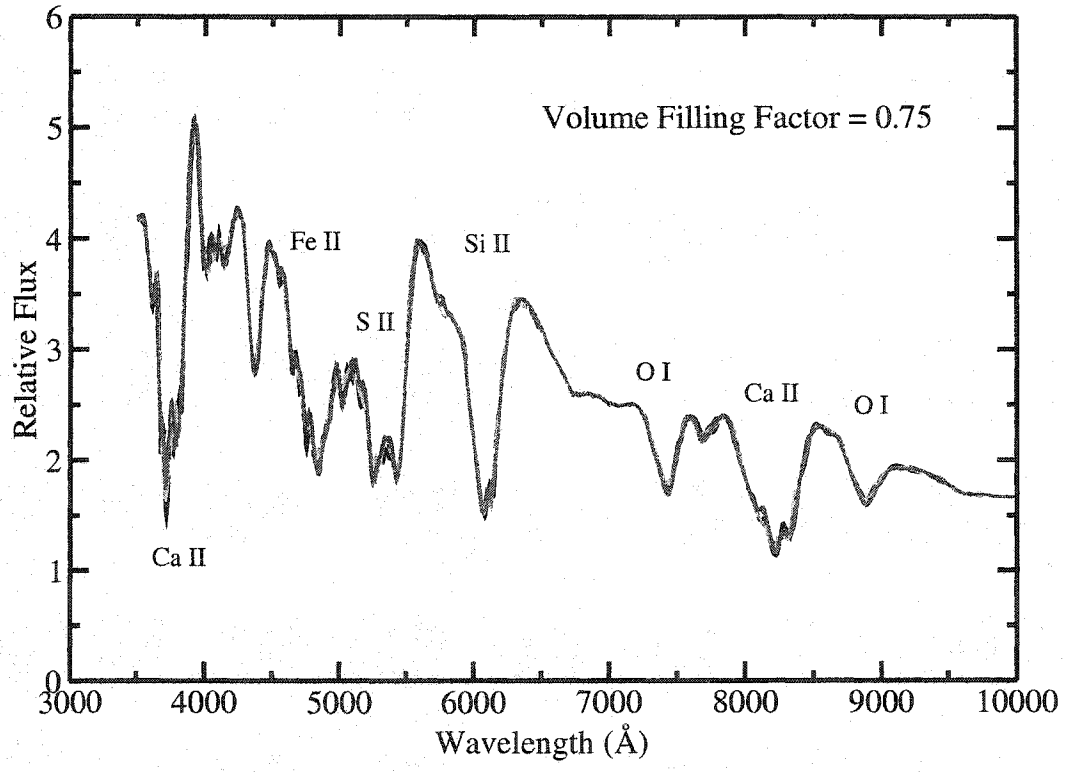

Figure 3.3: Same as Figure 3.2, except for volume filling factor 0.75.

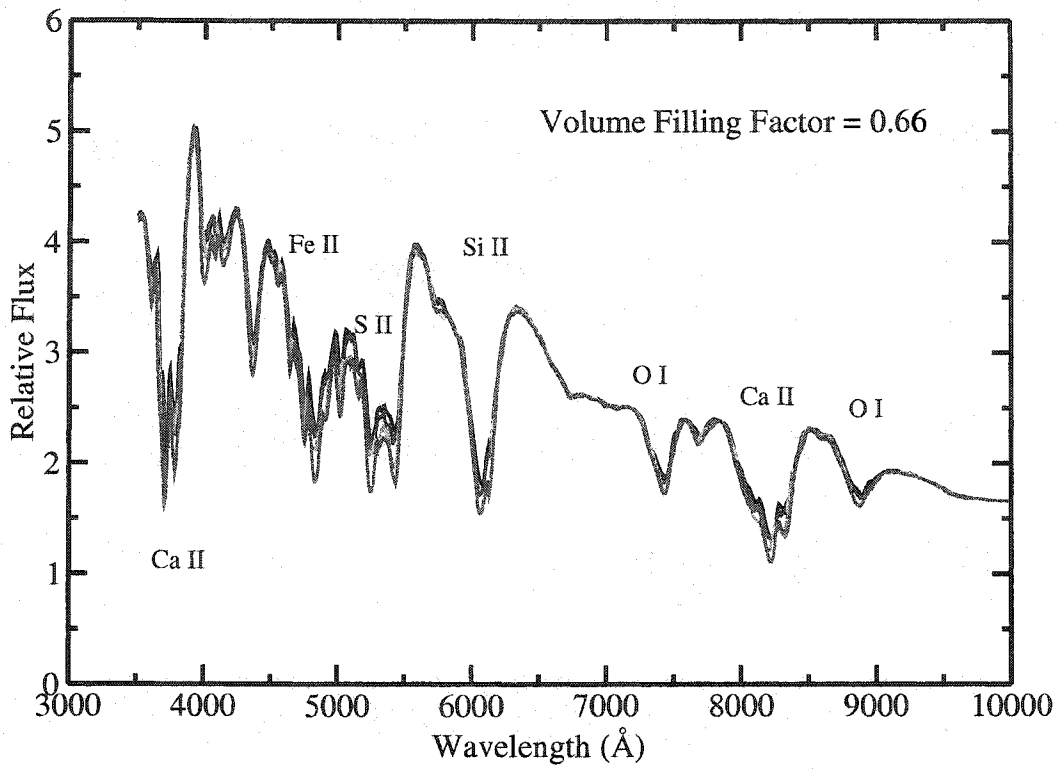

Figure 3.4: Same as Figure 3.2, except for volume filling factor 0.66.

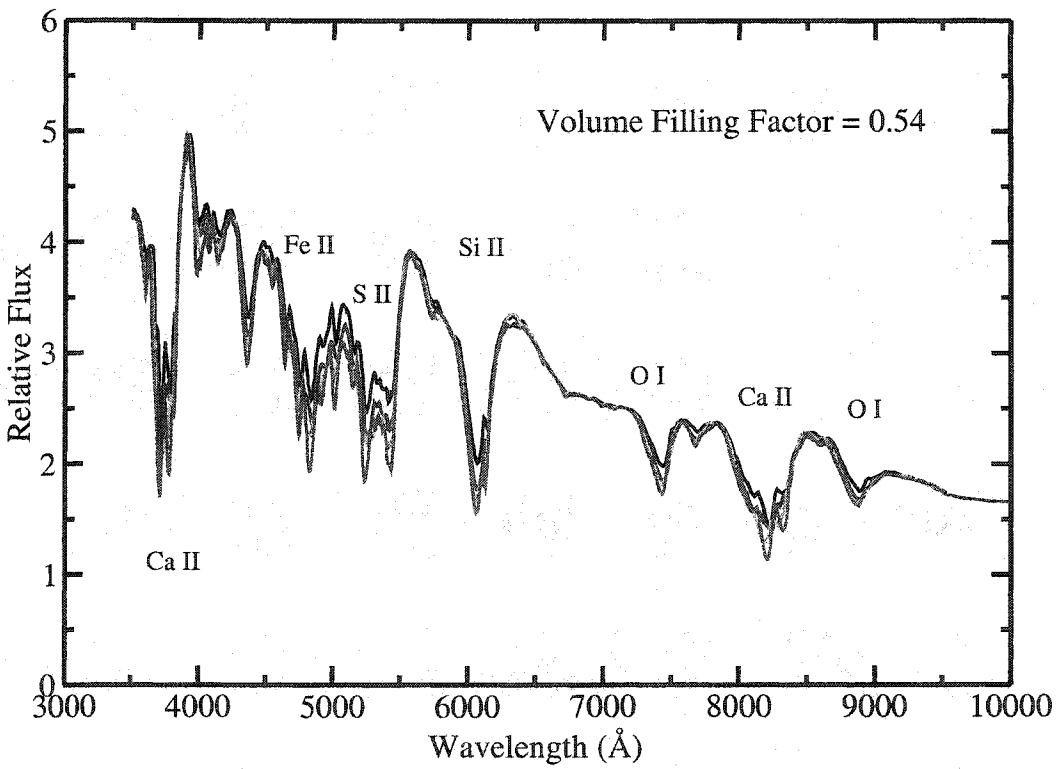

Figure 3.5: Same as Figure 3.2, except for volume filling factor 0.54.

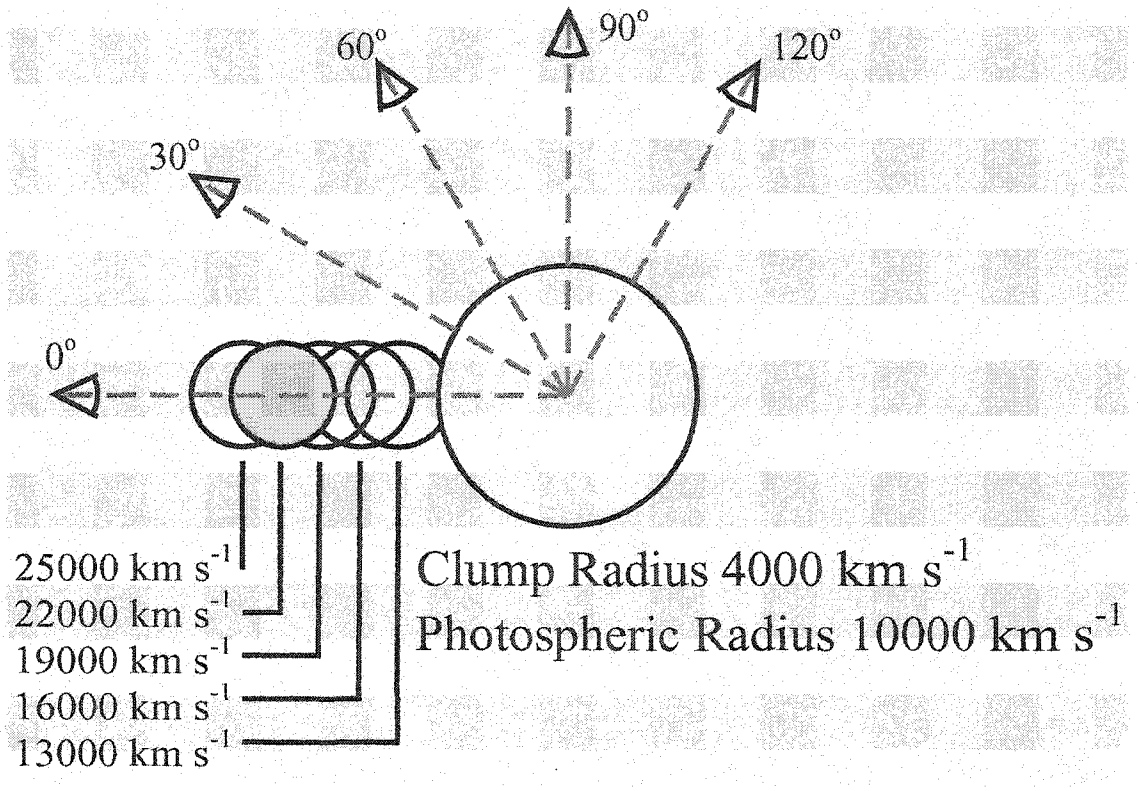

Figure 3.6: Layout for clump examples.

For simplicity, we consider a few configurations of a single clump of line optical depth. Inside the clump, we again use an exponential profile to determine optical depth. In Figure 3.6, the geometry we consider is shown. The clump is placed at different radii and line profiles from five lines of sight are calculated per clump placement. We examine two single scattering cases. The first case is a single line forming in the clump, assuming pure resonance scattering. In the second case, we again consider a single line but suppose that some source of local emission is contributing to line formation.

In Figure 3.7, line profiles from five lines of sight per clump position are plotted. The placement of the clump center is marked by each set of line profiles. The most obvious trend is that, assuming pure resonance scattering, absorption signatures due to the clump are more distinct than emission signatures. When the clump is eclipsing

the photosphere (black and red profiles, and the blue profile when the clump center is at 13000 km s^{-1}) the line optical depth scatters some of the light away from the line of sight to the observer. But when the clump is situated such that it is in the emission lobe with respect to the observer, its contribution from scattering is meager compared to the direct light from the photosphere, since $S << I_{ph}$ for the clump.

Another effect to consider in the clump model is due to the *covering fraction* of the photosphere due to the clump. Even if the optical depth in an eclipsing clump is infinite, the ratio of the depth of the corresponding absorption feature to the local continuum cannot exceed the covering fraction. To be concise, we define the covering fraction of the photosphere for a CD plane depending on where optical depth in the line exceeds unity. That is, for a CD plane in front of the photosphere at v_z, the covering fraction is a simple ratio:

$$f_c(v_z) = \frac{\int_{A_{ph},\tau(v_z)>1} dA}{\int_{A_{ph}} dA}, \tag{3.14}$$

where A_{ph} is the projected area of the photosphere as seen from the line of sight in question.

In some cases, the assumption of pure resonance scattering is not applicable to a line. An excellent example is Hα, which is most always seen in net emission in SNe II. In Figure 3.8 we show the effect that such net emission may have on the same line forming in the same clump. We adopt a rather extreme case, since here we have taken $S = I_{ph}$ in the line, so the photosphere blocking signature of the clump in Figure 3.7 completely disappears. In general, the net emission source function in a line is completely decoupled from the photospheric intensity, so the emission features from the clump for non-eclipsing lines of sight can be appreciable. This is a definite contrast to the emission feature situation in pure resonance scattering lines.

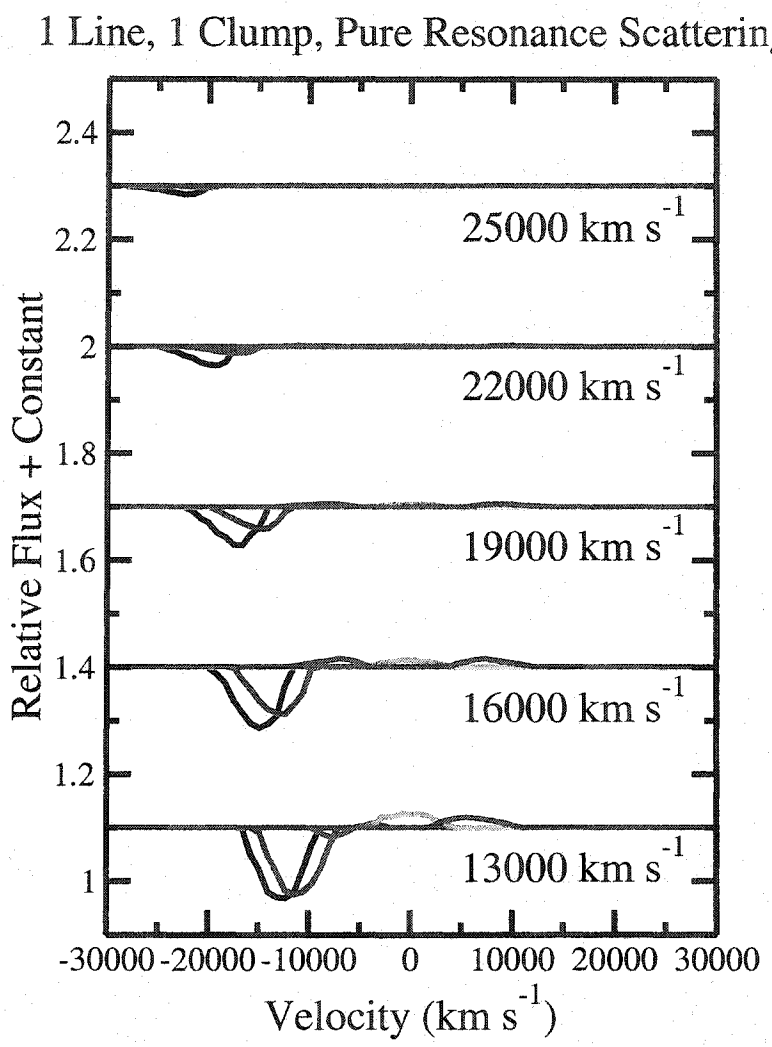

Figure 3.7: Single line profiles forming in a single clump, assuming pure resonance scattering. For each clump-center velocity, line profiles for five observers (black - 0 degrees, red - 30, blue - 60, brown - 90, violet - 120) are superimposed.

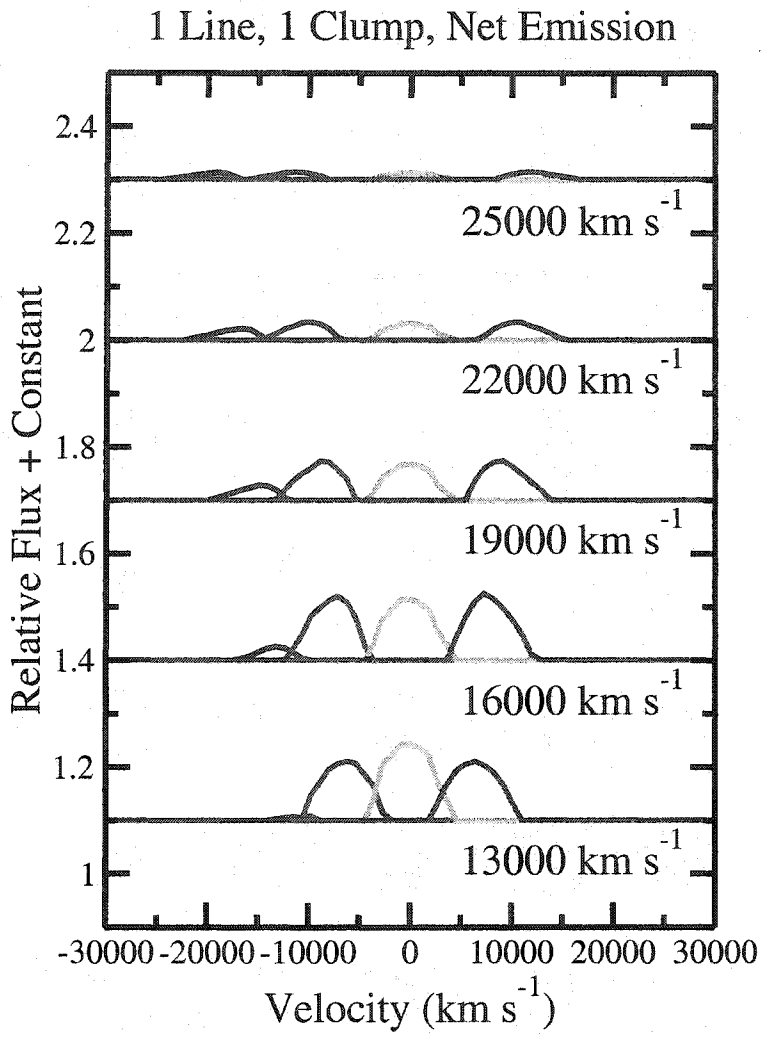

Figure 3.8: Single line profiles forming in a single clump, assuming net emission. For each clump-center velocity, line profiles for five observers (black - 0 degrees, red - 30, blue - 60, brown - 90, violet - 120) are superimposed.

3.3 Multiple Scattering Line Profiles in 3D Models

To maximize confidence that the radiation fields we compute are correct enough to generate reliable synthetic spectra, we must take into account multiple scattering of radiation from all the line interactions considered. This will account for the amplification and attenuation of the mean intensity with respect to its single scattering value.

The traditional means of doing this is described in Chapter 2, and this system of integration is best applied to situations of high symmetry in the optical depth distribution. To overcome the angular resolution, efficiency, and code architecture issues involved in 3D, we opt for a passive approach to feeding blue radiation to successively redder lines: the Monte Carlo (MC) technique.

The development of the MC technique is usually attributed to Ulam and von Neumann at Los Alamos during World War II. The first implementation of the method was to the problem of neutron transport as a part of the effort to build the atomic bomb. Individual energy-dependent probabilities for various neutron reactions were known (i.e., cross sections for elastic or inelastic scattering, and absorption), but conventional mathematical methods of combining these to compute penetration probabilities were useless. Ulam and von Neumann solved the problem by simulating trajectories of neutrons by random-walk. At each possible interaction, a random outcome was determined probabilistically. This new technique solved the problems of neutron transport accurately. Since its first application over 50 years ago, the MC technique has been applied to other problems of transport, including particle physics simulations, nuclear reactor design, traffic flow, and even the study of the theory of evolution. Our motivation for choosing the MC technique is that it is *geometrically generic*. We need not rely on symmetries of any kind to solve the transfer problem.

The application of the MC technique to the problem of ES modelling is straight-

forward. Simulated photons emerge from the core with wavelengths determined by a spectral energy distribution (e.g., the Planck function, now represented by a probability distribution). Each photon moves from one interaction to the next until it either escapes through the top of the atmosphere or is resorbed when intersecting the core. Interactions will occur only at resonance points; in the comoving frame the photons redshift as described earlier. At each line interaction, a random outcome will be selected based on the Sobolev optical depth. For example, if we assume pure resonance scattering, a line with optical depth τ_l will scatter a photon if $-\ln(\Re) < \tau_l$, where $\Re$ is a uniformly chosen random deviate between 0 and 1.

This technique averts two problems that we would encounter in the deterministic method of computing line source functions. The first is the problem of resolution. To increase angular resolution of the radiation field in the deterministic method, more and more sampling beams are required. The sampling beam directions for a large number of beams cannot be determined without annealing. In principle, the problem could be solved, but the MC technique provides an elegant solution: More photon trajectories mean more angular resolution of the radiation field. The second problem averted is that of sampling uninteresting directions. Photons will not scatter from uninteresting directions precisely because there is nothing there to scatter them. Both effects are illustrated by Figure 3.9. The MC technique also lends itself quite easily to parallelization; since the photon trajectories are completely independent of one another, communication among processors is minimized.

To capitalize on the power of the MC method, we use an innovative equal energy packet (EEP) formalism developed by Leon Lucy and implemented in 1D SN problems a few years ago (Mazzali & Lucy, 1993; Lucy, 1999a,b, 2002, and references therein). Our implementation is the first to apply it to multidimensional SN problems. The EEP implementation of the MC technique has many benefits which we will point out along the way. Our 3D MC SN spectrum code we have named `Brute`, and

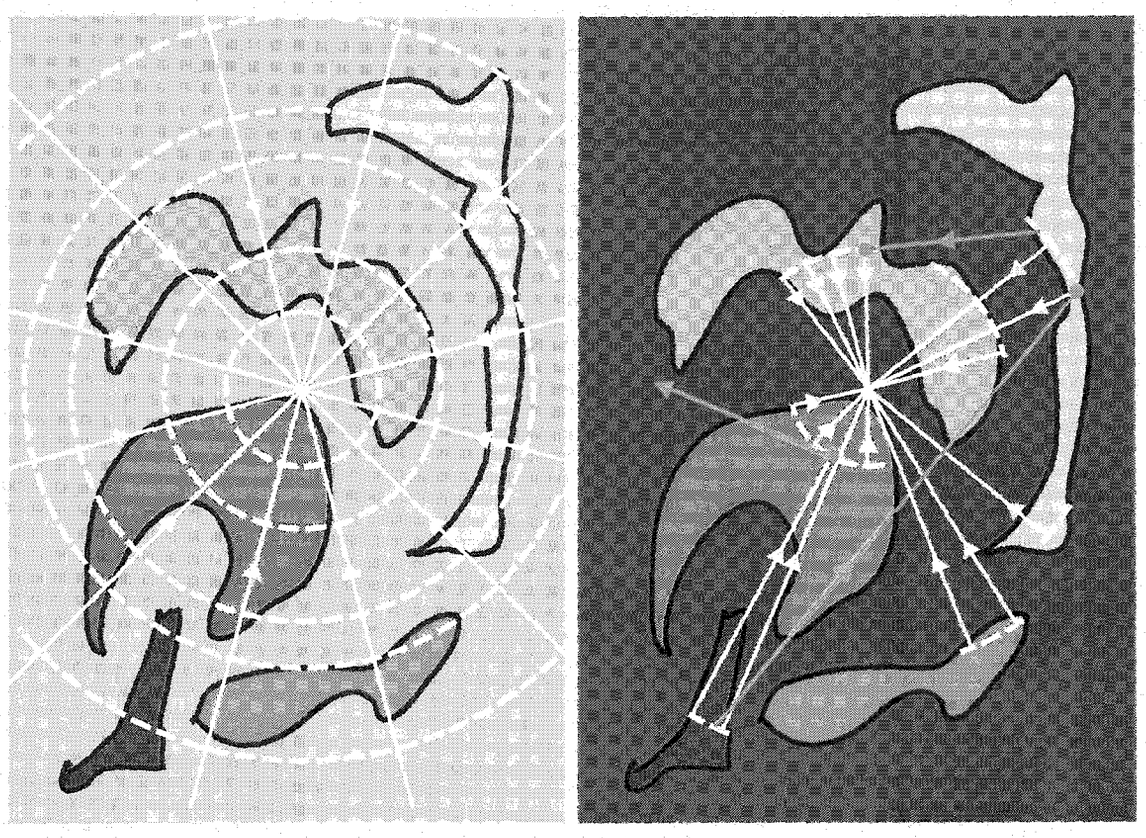

Figure 3.9: Computing J without and with Monte Carlo. On the left, sampling beams used for computing J from radiation arriving at the point at the center are shown. Note that the red blob is completely unsampled unless the angular resolution is increased. On the right, some photon trajectories are shown. In this case, the red blob is sampled, and to increase the angular resolution for computing J, we need only increase the number of packets followed.

the architectural details of its three versions are described in the Appendices. The remaining line profiles in this chapter are computed using the simplest version of `Brute`, which we call `tauBrute`.

Instead of simulating the photon trajectories individually, we group them together into *packets* of equal energy. The number of photons in a packet n_γ is related to the packet energy ϵ_γ by

$$\epsilon_\gamma = \frac{n_\gamma hc}{\lambda}. \tag{3.15}$$

Packets are not split upon interactions. Rather, as the number of packet trajectories simulated approaches infinity, the individual photon results for scattering proportions are recovered. Until the relative number of packets launched which escape is known, the value of ϵ_γ is unconstrained. After the simulation is complete, the energy per packet is normalized according to

$$L_* = N_* \frac{\epsilon_\gamma}{\Delta t}, \tag{3.16}$$

where L_* is *either* the core luminosity *or* target (observed) SN luminosity, N_* is *either* the number of packets launched from the core *or* the number which escape the atmosphere. The Δt factor is the "duration" of the Monte Carlo experiment, which is unconstrained; in all radiation field and absorption rate estimators we use Equation (3.16) to eliminate $\epsilon_\gamma/\Delta t$ which appear there.

In all versions of `Brute`, the line forming atmosphere is broken into cells. The size of the cells is chosen to be as small as possible, so that the optical depth and radiation field functions are resolved adequately. Opacity and emissivity are quantized in wavelength according to a velocity scale taken to be smaller than the cell size by at least a factor of 10. We refer to the units of wavelength quantization as "bands."

Every time a packet encounters a possible resonance in a given cell, a correspond-

ing cell packet-in-resonance tally is incremented for the interaction band. This occurs whether or not a scattering occurs, since the energy carried by the packet contributes to the cell's energy density in any case. At the end of the simulation, we convert raw packet-in-resonance tallies into an estimate of $J(\lambda)$ for each band with nonzero optical depth in each cell.

We arrive at the mean intensity estimate in an oblique but geometrically generic way. Instead of integrating the arriving intensity over all solid angle, we exploit the relationship between the mean intensity $J(\lambda)$ and energy density $u(\lambda)$:

$$\frac{4\pi}{c} J(\lambda) d\lambda = u(\lambda) d\lambda. \tag{3.17}$$

At any given instant, a packet contributes its energy to the energy density of a band in the enclosing cell. Thus, using N_λ for the total number of resonances in the band and V for the volume of the enclosing cell,

$$u(\lambda) d\lambda = \epsilon_\gamma \frac{N_\lambda}{V} \frac{\delta t}{\Delta t} \tag{3.18}$$

where δt is the time of flight through the band, so the time-averaged energy contribution to the band is $\delta t / \Delta t$. Notice that by keeping the packet energy constant as it propagates, we are ignoring a slight effect of energy change as packets shift frames. Combining Equations (3.18) and (3.17) yields

$$J(\lambda) d\lambda = \frac{\delta t}{4\pi} \frac{N_\lambda}{V} \frac{\epsilon_\gamma}{\Delta t}. \tag{3.19}$$

Since the opacity has been quantized into bands of constant velocity width Δv, and the velocity field is homologous, then we may replace the time of flight, $\delta t = \Delta v t / c$, where t is the time since explosion. Using the packet energy normalization condition

Equation (3.16), and the relationship between band wavelength and velocity widths $d\lambda = \lambda \Delta v/c$, we obtain an estimate of the mean intensity,

$$J(\lambda) = \frac{ct}{4\pi\lambda} \frac{N_\lambda}{N_*} \frac{L_*}{V}. \tag{3.20}$$

This gives us the prescription needed to turn the MC packet tallies into mean intensity, and thus include multiple scattering into our 3D models of SN spectrum formation.

We may now consider the signature of line blends arising from clumpy material. We perform analogous experiments to those described in the previous section for a single line. However, this time we assume pure resonance scattering in both cases and change the spacing of the lines.

In the first case, the lines are separated by 50 Å, and the result of the calculation is in Figure 3.10. At high velocity, the lack of substantial optical depth prevents blending of the two absorptions into one. Again we see that emission features are harder to pick out than absorption features for the same reason that in pure resonance scattering, $S << I_{ph}$.

If we separate the lines by 150 Å, a wavelength corresponding to a CD plane velocity separation larger than the clump diameter, the two lines trace out individual copies of the same clump. This is illustrated in Figure 3.11. If the material were placed into a spherical shell, the bluer line would work to wash out the redder line to some extent.

Considering the covering fraction limit on absorption feature depth for two lines from the same ion has an interesting consequence. Suppose that two such lines originate in an ion and share the same lower level. Then according to Equation (3.5), the ratio of the optical depths is simply (neglecting the corrections for stimulated emission)

$$\frac{\tau_1}{\tau_2} = \frac{\lambda_1}{\lambda_2} \frac{(gf)_1}{(gf)_2}. \tag{3.21}$$

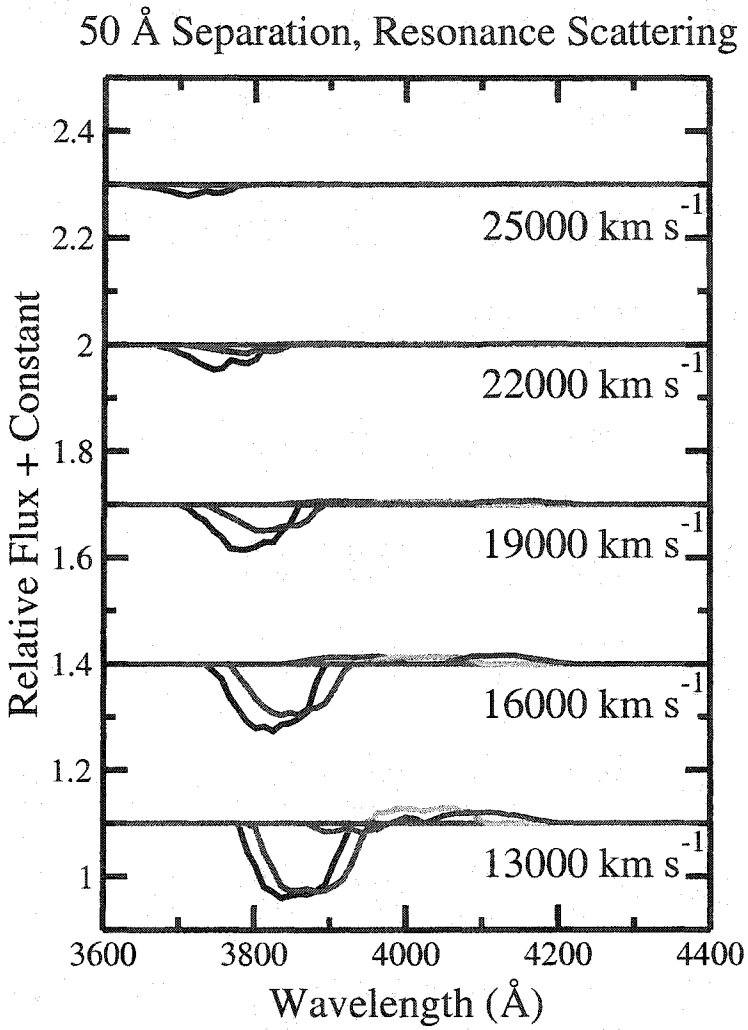

Figure 3.10: Line formation in a clump, small separation case. The two lines are 50 Å from one another.

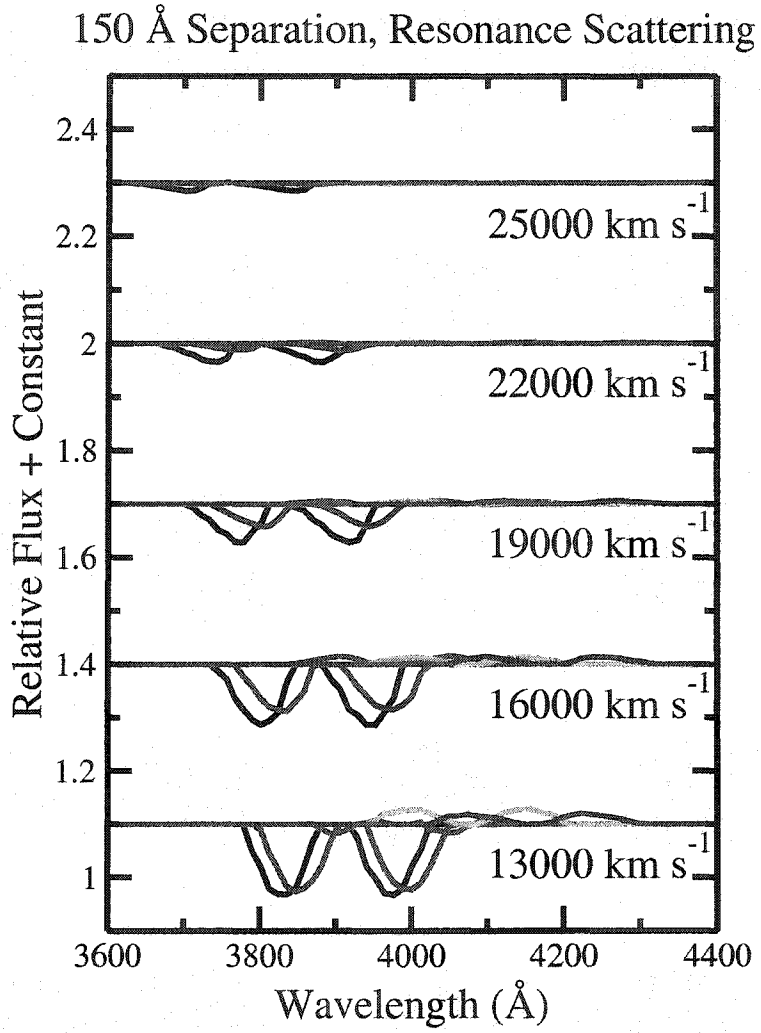

Figure 3.11: Line formation in a clump, large separation case. The two lines are 150 Å from one another. Two distinct notches are visible.

Suppose that one line is much stronger than the other. If this line is optically thick, then the corresponding absorption feature depth relative to the local continuum will equal the covering fraction. As we increase the optical depth in both lines, the absorption feature strength of the stronger line will remain mostly unchanged as a consequence of partial covering. Eventually the weaker line absorption catches up. This implies that the ratio of the weaker line's absorption feature to that of the stronger (due to partial covering) may exceed that possible in the full covering case. This phenomenon requires that the particulars of the optical depth distribution are such that the clump boundary is rather sharp.

3.4 Role of Perspective-Dependence in Spectroscopic Diversity

Let us return to the question of how much and what kinds of deviation from spherical symmetry are permissible in the atmospheres of spectroscopically normal SNe Ia. Our preliminary analysis has taught us that the effects of nonsphericity are most easily detected in the absorption features of the P-Cygni profiles when the lines in question are scattering lines. The 6100 Å Si II feature so prominent in SN Ia spectra is generally very similar from event to event. Can we place a constraint on the nonsphericity of silicon in the SN Ia atmosphere based on the apparent lack of profile diversity?

To investigate the effects of such composition clumping on line formation, we again consider the formation of a single line. We employ the standard assumptions of the ES model, and assume a pure resonance scattering source function using the `tauBrute` code. We characterize the degree of clumpiness with two parameters. The first represents the size of the perturbations with respect to the core, and the second controls the sparsity or density of the perturbations themselves. We will vary these

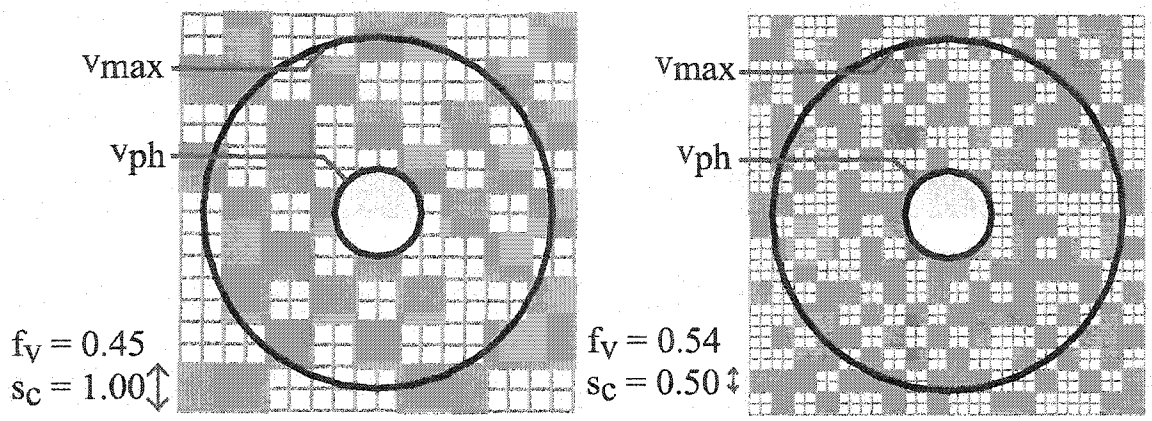

Figure 3.12: White noise parameterization. Two quantities are varied: The size of the chunks in units of photospheric radius, s_c, and the volume filling factor (fraction of the chunks turned on) f_v.

parameters and compute line profiles from a large number of randomly chosen lines of sight, searching for the dependence of line profile diversity on these parameters. In general, we expect that when these two parameters conspire to produce significant perspective-dependent covering fractions $f_c(v_z)$, absorption features will exhibit *perspective-dependent diversity.* Our goal is to constrain the term "significant."

The perturbations themselves are simply cubical "chunks" within which we may turn optical depth on ($\tau = 280 \exp(-v/3000)$) or off ($\tau = 0$). The first perturbation parameter is the chunk size parameter s_c, the length of a cube along one of its edges in units of core radius. The second parameter is the volume filling factor f_v, corresponding to the fraction of cubes within which line optical depth is turned on. The turning on and off of optical depth is reminiscent of static, so we call these models "white noise" models. Two example white noise models are represented in Figure 3.12. A representation of a white noise optical depth distribution ($c_s = 0.53, f_v = 080$) appears in Figure 3.13. In all of these white noise simulations, the photospheric velocity $v_{ph} = 10000$ km s^{-1}, typical of a SN near maximum light.

An example of a set of line profiles and covering fractions computed for 100 randomly chosen lines of sight is shown in Figure 3.14. The lower portion of the figure is



Figure 3.13: An example optical depth distribution for white noise experiments.

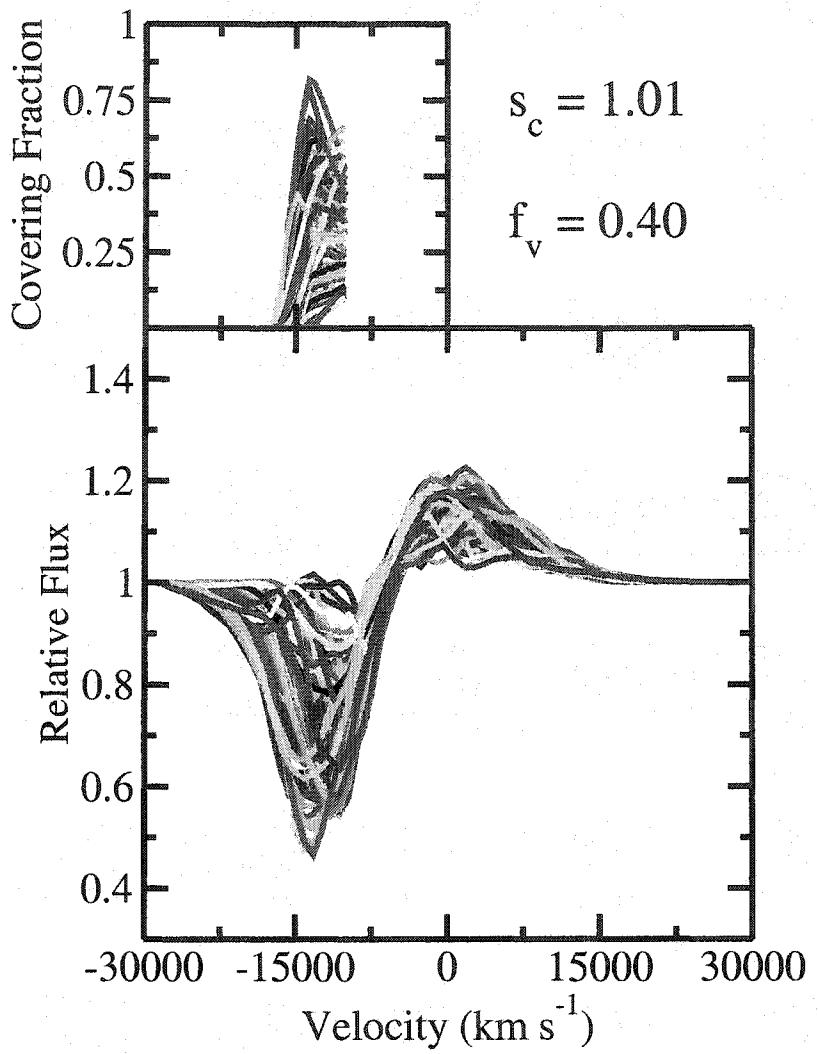

Figure 3.14: Example white noise line and covering fraction profiles for clump size parameter $s_c = 1.01$ and envelope filling factor $f_v = 0.40$. Results from 100 lines of sight are plotted.

the set of line profiles, plotted one on top of the other in Doppler space. The upper portion of the figure includes the corresponding fractions of the photosphere obscured by line optical depth exceeding unity in terms of Doppler velocity. The velocity axes for the upper and lower plots match. In this particular example, the chunks have edge length $1.01 v_{ph}$, and 40% of them have nonzero optical depth set.

The plots in Figure 3.14 are too busy for us to interpret. Instead of plotting 100 line profiles and covering fraction curves for each pair of (s_c, f_v), we plot the average

profiles and typical deviation from that average. In particular, for each Doppler velocity we compute the standard deviation over all lines of sight for both the line profile and covering fraction. Each diversity plot then includes the average profile and two curves which represent that average curve plus or minus the standard deviation. These profile diversity plots appear in Figures 3.15 through 3.19.

The general trend in the diversity plots is as expected: Larger variations in covering fraction as a function of perspective lead to larger variations in the absorption features of the corresponding line. In fact, a plot of the dispersion in the line profiles at 10000 km s^{-1} versus that in the covering fractions at the same velocity shows that they are linearly related (Figure 3.20).

Of course the results summarized in Figure 3.20 cannot be immediately applied to observations because of the particulars of the parameterization chosen. In order to quantitatively evaluate the connection, a more systematic (but less obvious!) way of varying the covering fraction must be used, and many more realizations are needed. But we can interpret Figure 3.20 as clearly demonstrating the relationship between gross perspective-dependence in covering fraction and line absorption profiles.

The appearance of the trend suggests that we may reverse engineer some ideas about composition clumping in spectroscopically normal SNe Ia. At maximum light, the depth of the Si II feature due to the doublet $\lambda\lambda$6347, 6371 Å does not vary appreciably as a function of the line of sight. A few examples in the wavelength range of interest appear in Figure 3.21. From a sample of good quality maximum light spectra obtained over the past two decades, we determine an average value of the absorption relative to the continuum of 0.67, and a standard deviation of 0.06. If we interpret these observations under our assumption of global sphericity, then the lack of substantial scatter in the depth of the absorption feature suggests that the clumping scale of silicon in spectroscopically normal SNe Ia is small. If we were to belive Figure 3.20, the variations in line of sight covering fraction in the Si II line

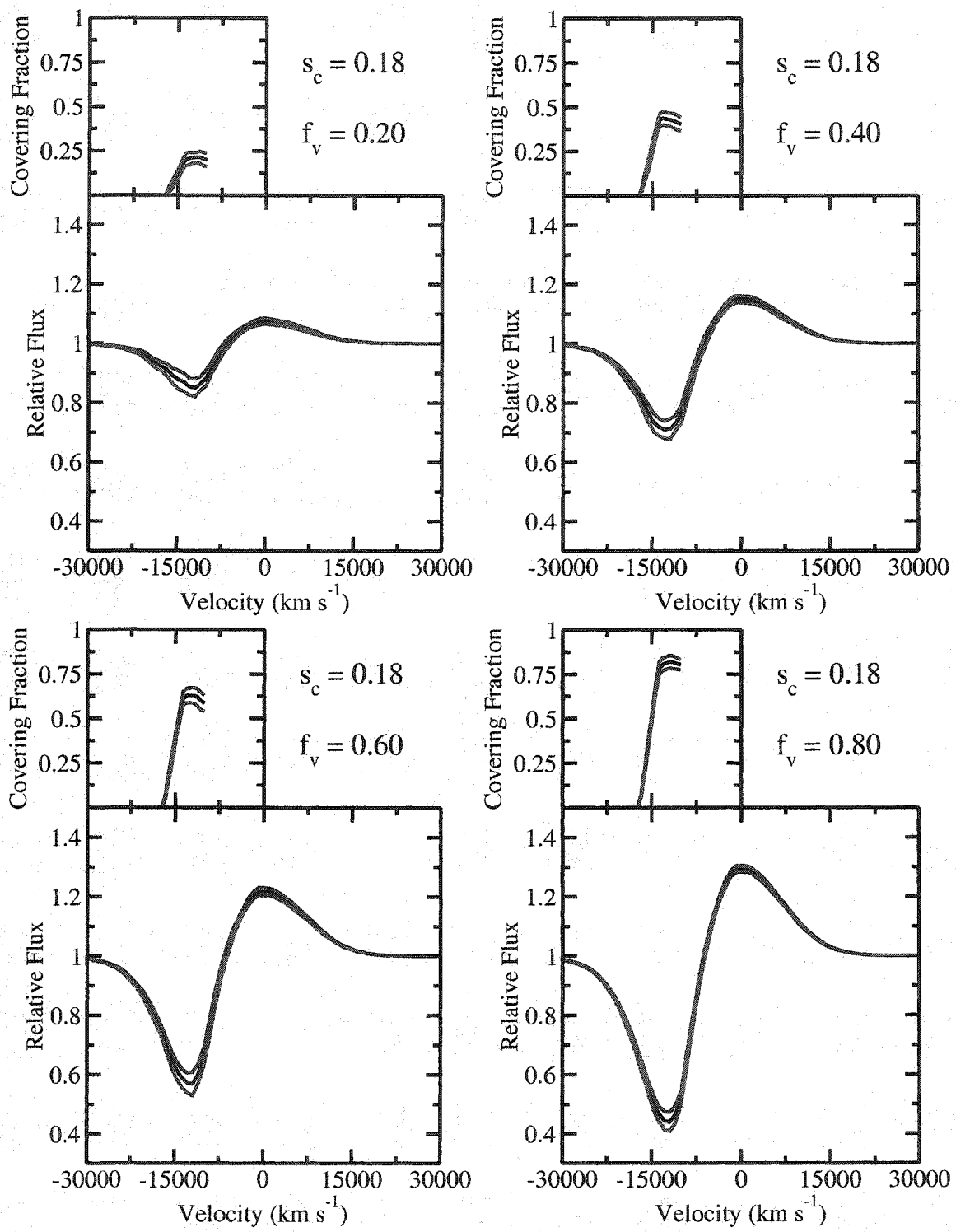

Figure 3.15: White noise profile diversity plots for $s_c = 0.18$. The black line profile and covering fraction profile are the averages over 100 random lines of sight. The red curves on either side are the average curve plus or minus σ.

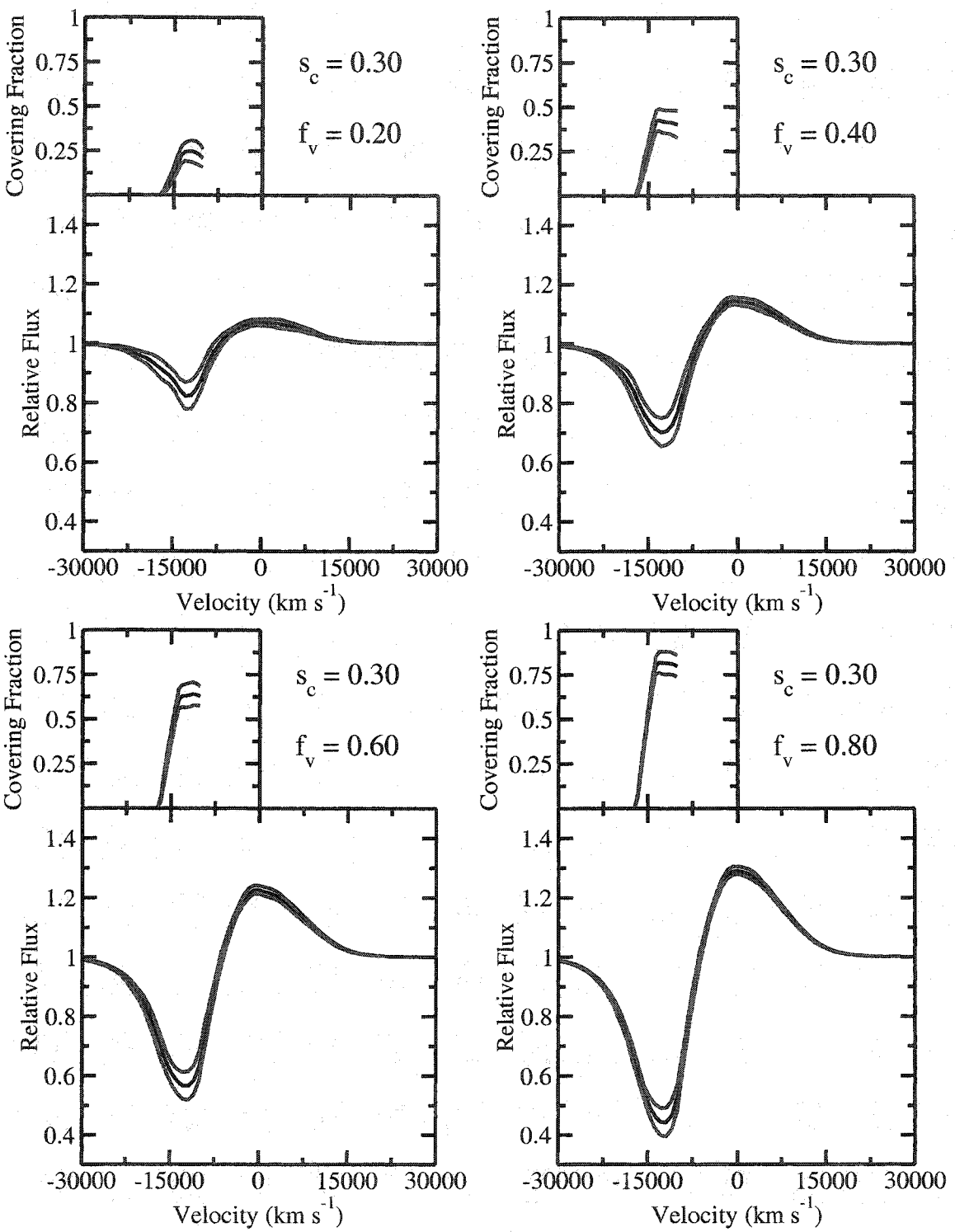

Figure 3.16: Same as Figure 3.15, except $s_c = 0.30$.

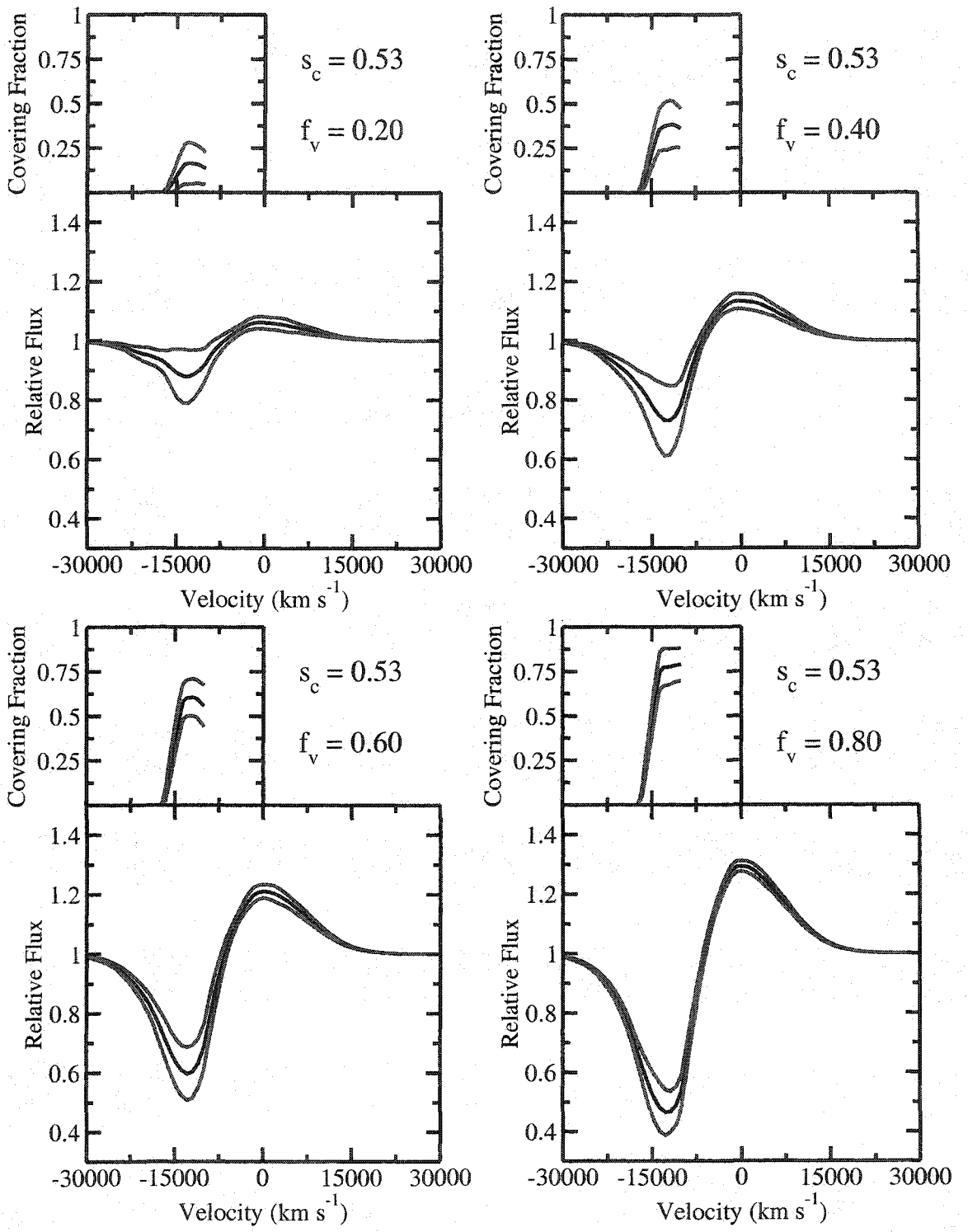

Figure 3.17: Same as Figure 3.15, except $s_c = 0.53$.

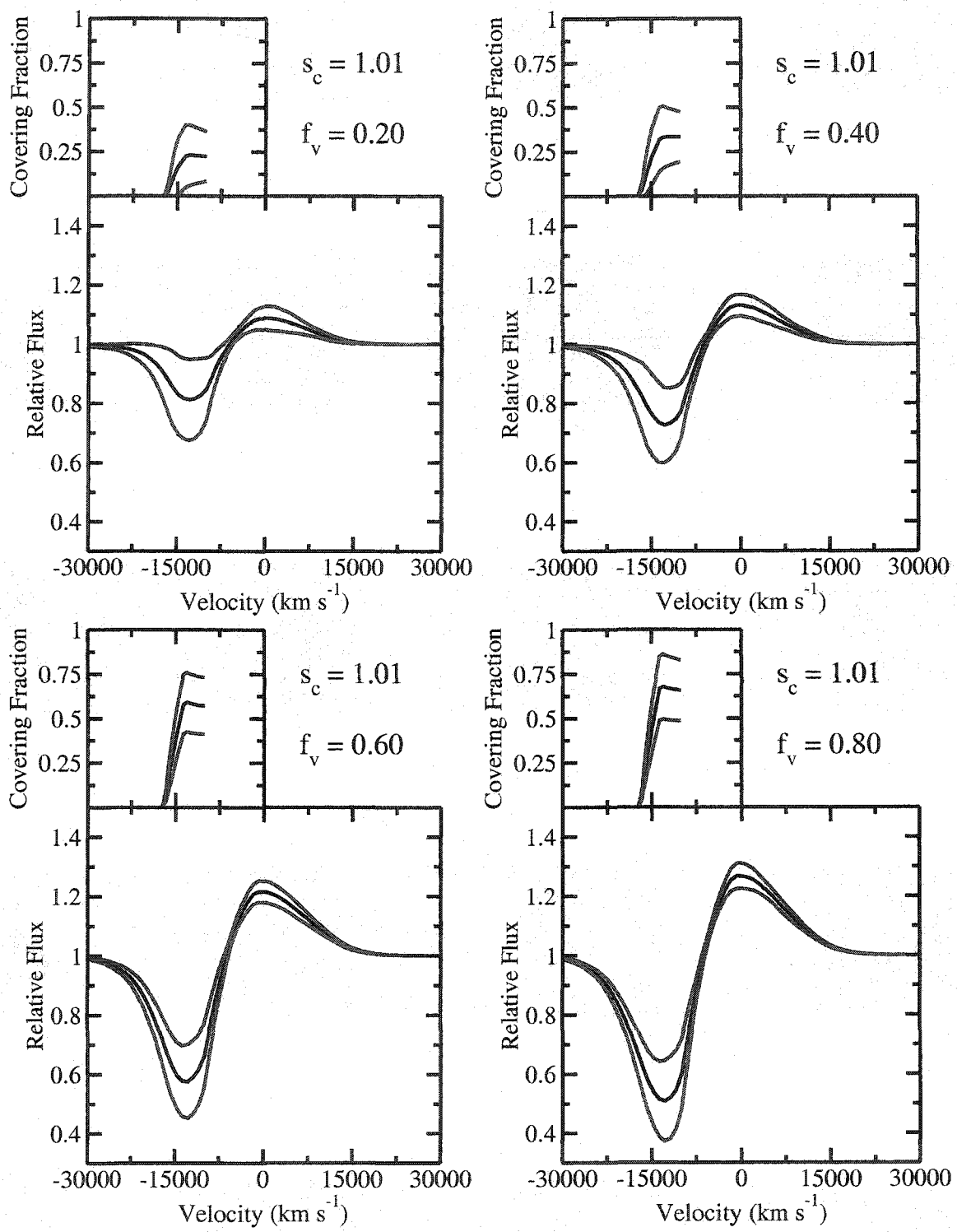

Figure 3.18: Same as Figure 3.15, except $s_c = 1.01$.

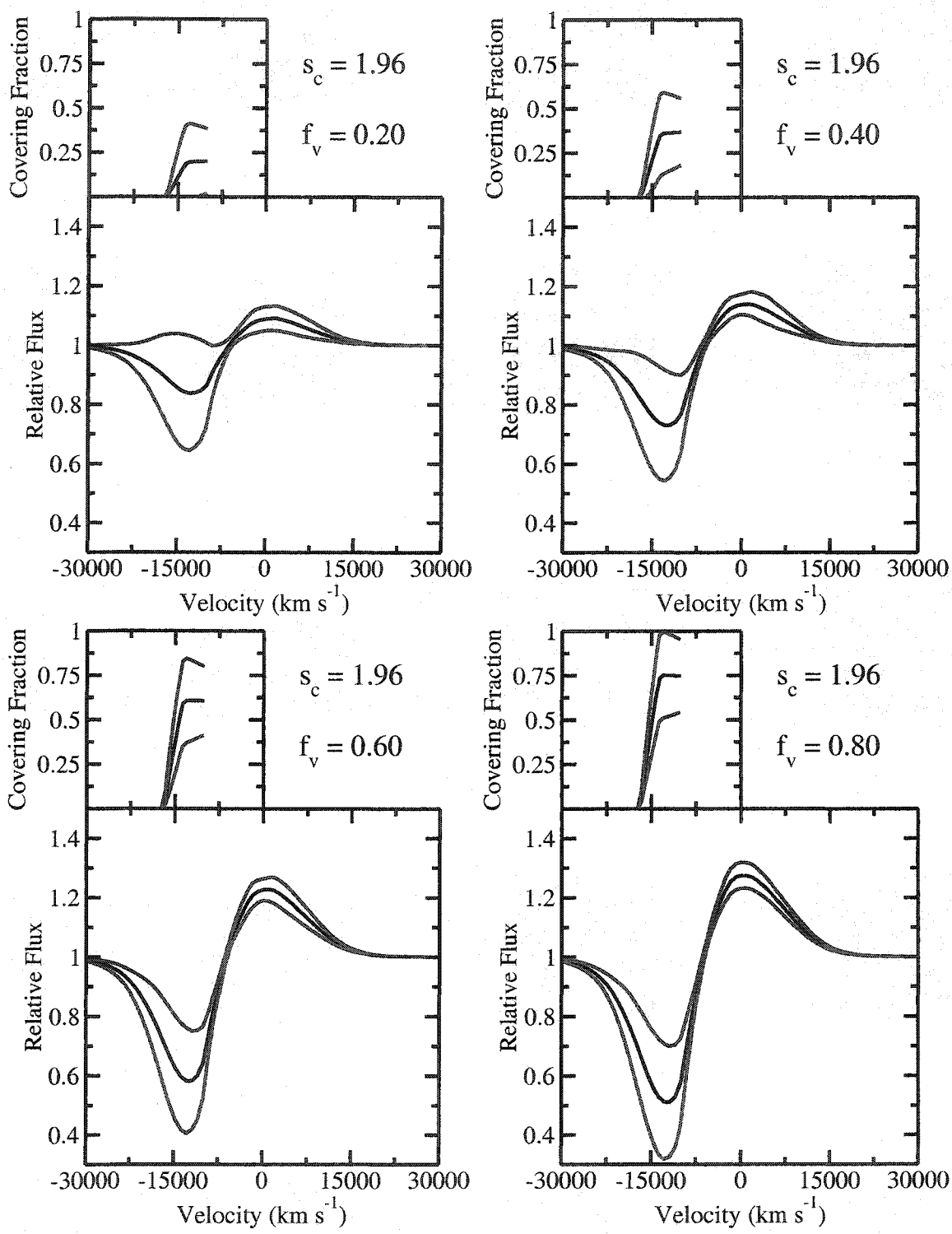

Figure 3.19: Same as Figure 3.15, except $s_c = 1.96$.

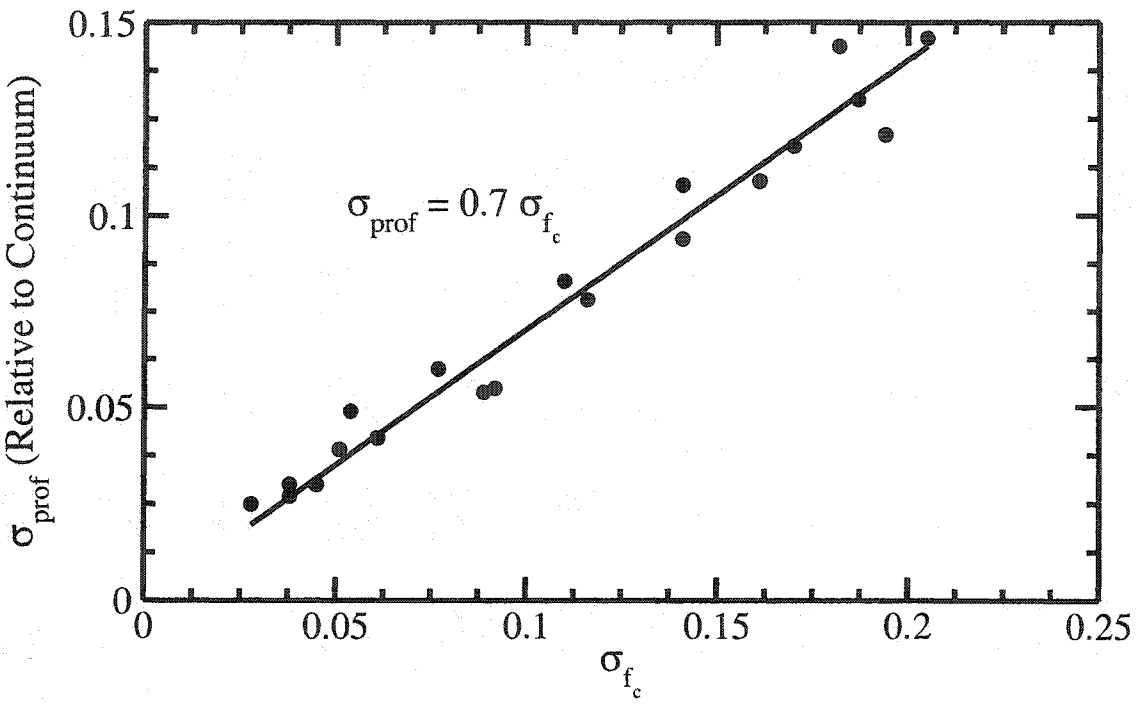

Figure 3.20: Line profile standard deviation as a function of covering fraction standard deviation. The deviation plotted is that for which $v_z = 10000$ km s^{-1}.

should be less than about 0.1.

3.5 Summary

By effecting minor modifications to the direct analysis code `Synow`, we have produced `ClumpySyn`, a code that can generate spectra from compositions without spherical symmetry. Based on a simple parameterization, we suggest that the important factor for spectra from events lacking a spherical composition is the fraction of the photosphere covered by clumps. If the clumps are large compared to the size of the photosphere, inhomogeneity in unblended line absorption manifests itself. Below a threshold scale, these clumps only weaken absorption along different lines of sight by the same amount. Absorption strength accounted for by spherically symmetric compositions can be recovered in clumpy models by increasing optical depth, but only to

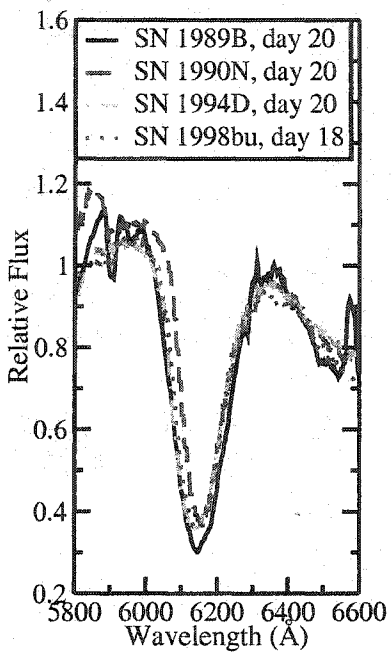

Figure 3.21: Si II absorption features in maximum light SNe Ia.

an extent.

In addition, we suggest that the robustness of absorption depth measurements in the Si II feature in normal Type Ia SNe implies that any perturbations in composition away from spherical symmetry are smaller than the threshold scale. From this, one might conclude that if a general characteristic of deflagration models is the formation of large clumps of silicon and iron, then spectroscopically normal SNe Ia cannot be the result of C/O white dwarf deflagrations. More conservatively, we suggest that explosion models must avoid generating large-scale bubbles or clumps in composition to recover normal SN Ia spectroscopic homogeneity.

Chapter 4

High-Velocity Ejecta in the Peculiar SN Ia 2000cx

Recent polarization observations of the SNe Ia 1999by (Howell et al., 2001) and 2001el (Wang et al., 2003; Kasen et al., 2003) indicate that at least some SN Ia envelopes deviate from spherical symmetry. The strongest case for such deviation appears in the Ca II lines of SN 2001el. This event exhibits an unusual Ca II infrared (IR) triplet in its flux spectrum about a week before maximum brightness. Two triplets are evident: One corresponds to photospheric-velocity (PV) material and the other to higher-velocity (HV) material. In the polarization spectrum, the HV feature coincides with significant intrinsic net polarization. Kasen et al. (2003) investigate a number of envelope models to account for the HV feature. Generally, they conclude that (1) incomplete covering of the photosphere and (2) some deviation from spherical symmetry are required to produce the HV features. Unfortunately, conditions did not permit simultaneous observation of the blue spectrum so a corresponding phenomenon in the Ca II H&K feature remains unconfirmed.

Another unusual Ca II feature is found in the spectrum of the peculiar SN 2000cx

(Li et al., 2001a). Near maximum light, its ostensible Ca II IR triplet possesses an interesting quadruply notched feature perhaps due to what Li et al. call "some unique distribution of Ca in the ejecta of SN 2000cx," extending to high velocity. The wavelength coverage of the near-maximum light spectra is excellent. Though polarization data in the same wavelengths are not available, simultaneous fits of the H&K and IR triplet features may help constrain at least the HV photospheric covering fraction (if indeed the HV material is not distributed in spherical symmetry).

It remains unclear why clumpy HV ejecta could occur in SNe Ia. Full simulations of synthetic spectropolarimetry have yet to test the existing 3D deflagration models (e.g. Gamezo et al., 2003): These explosion calculations have neither proceeded to the free-expansion phase nor provided abundance distributions required for such analysis. But parameterized, direct analysis of observed SN spectra remain a powerful way of guiding explosion modellers to replicate detected geometrical phenomena in their models.

In the previous Chapter, we discussed some of the general consequences of non-sphericity in SN envelopes for spectrum formation. Here we apply those same ideas to a specific case. The strategy is to analyze the Ca II features in the spectrum of SN 2000cx at a single epoch to constrain the HV ejecta geometry. A separate, multi-epoch, but exclusively 1D analysis of this object is in progress (D. Branch et al., in preparation). That work will address such orthogonal concerns as an exhaustive identification of PV features and the unusual color evolution of this SN. Here, we conduct alternate experiments of fitting the HV features with 1D and 3D parameterizations. At the end of the Chapter, we consider some scenarios that could lead to a 3D HV ejecta distribution.

In this Chapter, we use the parameterized 3D equivalent of `Synow` for the 3D fits. This version of `Brute` we call `synBrute`. The code architecture details on `synBrute` are included in Appendix B.

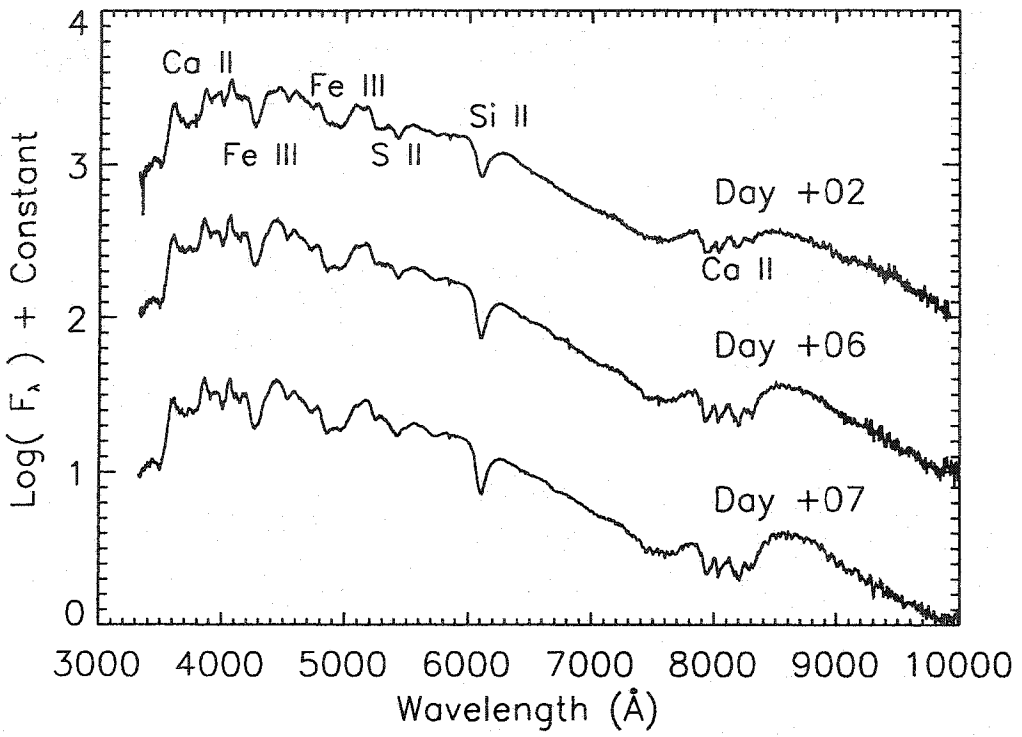

Figure 4.1: Near-maximum light spectra of SN 2000cx (Li et al., 2001a). The epoch relative to maximum light is listed above each spectrum.

4.1 Spectra

In Figure 4.1 are three spectra of SN 2000cx collected near maximum light, originally presented by Li et al. (2001a). The usual SN Ia absorptions from Si II (near 6150 Å) and S II (near 5400 Å) are accompanied by absorptions due to Fe III (near 4300 Å and 5000 Å). There is very little, if any, signature of Fe II. The narrow lines and apparent weakness of many of the usual features qualify this SN Ia as a spectroscopically peculiar event: It is more like SN 1991T than any of the other spectroscopically normal SNe Ia.

Between 7900 Å and 8400 Å are a series of four notches. Usually at this phase, only absorption from the two stronger lines of the triplet ($\lambda\lambda$8542, 8662 — often blended) are visible in this region, and these are the best candidates for the two redder notches.

The two bluer ones are perfectly consistent with a Ca II IR triplet shifted to about 22000 km s^{-1} toward the observer. The bluest and weakest line of the Ca II IR triplet (λ8498) is approximately ten times weaker than λ8542, and is likely heavily blended by that line. Other ions are unlikely to produce the notches; candidates such as O I are unconvincing due to the absence or weakness of concomitant lines in the spectra.

The corresponding Ca II H&K absorption feature (3500 Å to 3800 Å) is wide and flat. A collection of currently unidentified narrow absorption features obliterates its emission peak.

Figure 4.2 displays the Ca II features of SNe 2000cx and 1994D near maximum light in terms of velocity relative to the observer. The top half of each panel is the H&K feature relative to the gf-weighted doublet wavelength (3945 Å), while the bottom half is the IR triplet relative to its gf-weighted wavelength (8579 Å).

The fact that these two features are blends complicates the issue of choosing a reference wavelength for producing Doppler space plots. In a blend of P-Cygni lines, redder components dominate the shape of the aggregate profile if they are strong; they screen out the bluer lines. Nevertheless, the bluer lines must have some effect since they feed radiation to the redder lines. Given these ambiguities, we compromise by using the gf-weighted wavelengths for reference.

Figures 4.2a-c are from SN 2000cx at days 2, 6, and 7 past maximum light, respectively. For comparison, the normal SN Ia 1994D Ca II features at day 3 past maximum appear in Figure 4.2d. Hatano et al. (1999a) use HV Ca II and Fe II to improve their synthetic fits of SN 1994D. In that SN, the effect of the HV Ca II is much less pronounced than in SN 2000cx. In fact, the IR triplet of SN 2000cx has a HV absorption that has a depth relative to the continuum between that of SNe 1994D and 2001el.

Note that the four notches in the SN 2000cx IR triplet absorption do not evolve appreciably in velocity space over time, and that the overall velocity ranges of both

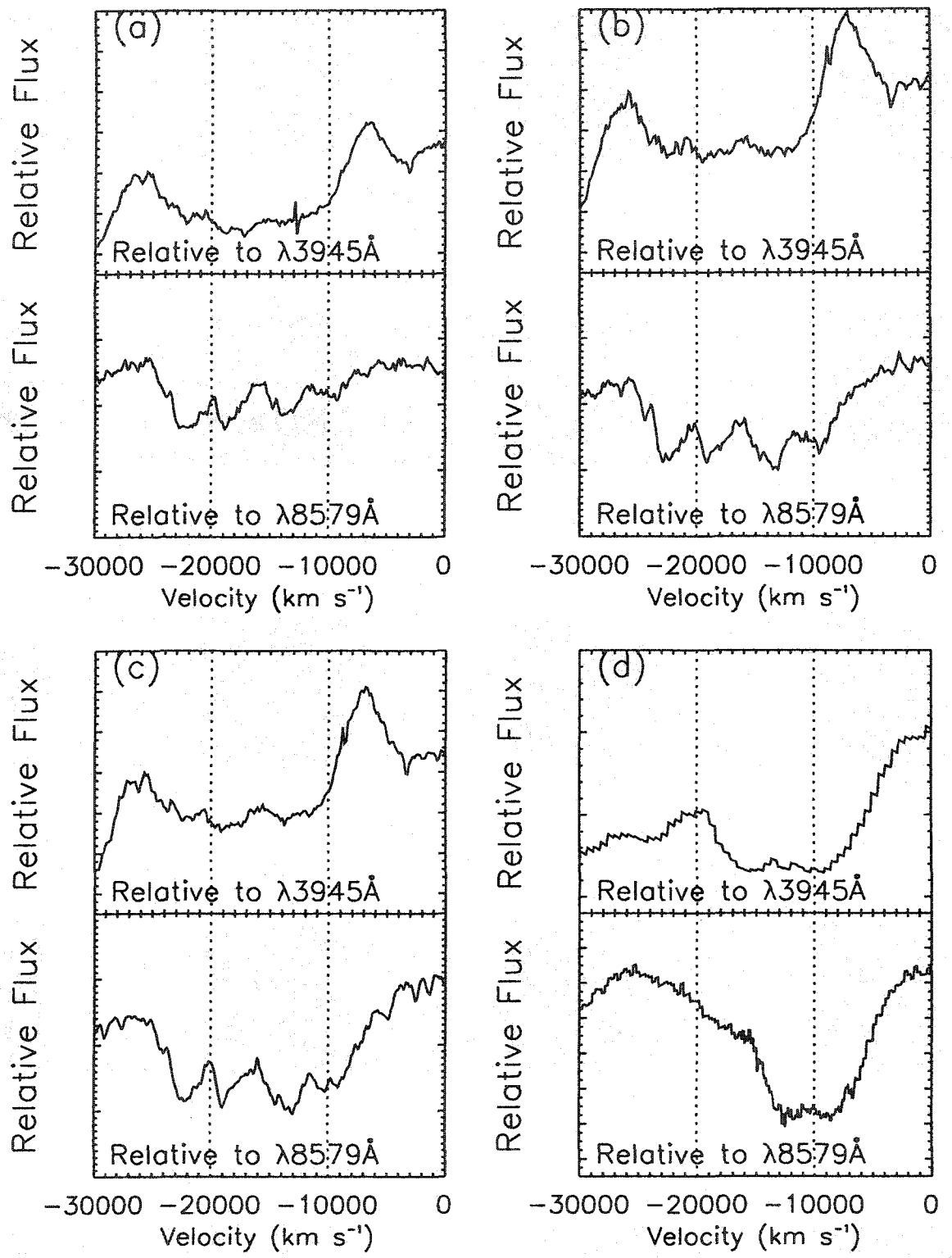

Figure 4.2: Ca II features in SN 2000cx at days 2 (a), 6 (b), and 7 (c) after maximum light, and those in SN 1994D at day 3 (d) after maximum. The features are plotted in terms of velocity relative to the observer, using the gf-weighted wavelengths of the Ca II H&K and IR triplet features.

features match. There appears to be a case for a one-to-one correspondence between notches in the IR triplet and depressions in the H&K absorption, but the blended nature of both features makes absolute confirmation difficult. Furthermore, the mild fluctuations visible in the H&K absorption could easily be due to some weak, narrow lines superimposed on the Ca II feature.

We henceforth designate the parts of the Ca II features forming above 16000 km s^{-1} relative to the gf-weighted wavelengths of H&K and the IR triplet as the HV features. Our fitting strategy will be to concentrate on replicating the velocity range of these features and some of their structure. Since the three SN 2000cx spectra in Figures 4.1 and 4.2 are all quite similar, we restrict the focus of the remainder of this paper to the spectrum obtained two days past maximum light.

4.2 Fits

For our fits, we adopt the parameterized optical depth approach described in Chapter 3. This approach has proved useful for fitting observed spectra to constrain the structure of SN envelopes. This empirical process is called "direct" analysis to distinguish it from "detailed" analysis where the full radiative transfer and non-local thermodynamic equilibrium (NLTE) rate equations are solved (Hauschildt & Baron, 1999). Specifically, the purpose of direct analysis is (1) to determine what species are present in a SN line-forming region and (2) to constrain the velocity space distribution of those species. The assumptions and approximations used generally restrict direct analysis to line phenomena, in particular to the Doppler shifts and overall shapes of absorption features. The results of direct analysis provide useful guidance to detailed spectrum modellers and to explosion modellers as well.

As a 1D direct analysis code, `Synow` has been used to fit many spectra of various types of SNe, e.g., SN Ia 1994D (Hatano et al., 1999a), several SNe Ib (Branch et al.,

2002), SN Ic 1994I (Millard et al., 1999), and SN II 1999em (Baron et al., 2000). As described in the previous Chapter, `Synow` parameterizes optical depth spatially using spherically symmetric contrast functions $\psi_1(v)$. Wavelength parameterization is controlled by reference optical depths and an excitation temperature.

For producing the simple one- and two-line experiments in Chapter 3, we applied spatial parameterization to lines of arbitrary wavelength using contrast functions $\psi_3(\vec{v})$. By coupling the line list of Kurucz (1993) and assuming the same wavelength parameterization technique as used by `Synow`to `tauBrute`, we produce a code we call `synBrute`, the synthetic parameterized version of the 3D SN analysis code `Brute`.

The $\psi_1(v)$ contrast functions were simple to turn into optical depth distributions in 1D, but the process is a little more cumbersome in 3D. The functions $\psi_3(\vec{v})$ are allowed to be completely arbitrary, so 3D reference optical depth templates are created separately and fed to `synBrute` in order to compute synthetic spectra. The storage requirements for `synBrute` models are much higher than for `Synow` models. Additionally, distribution of line opacity takes a long time, so we use parallel processing to accelerate the process. We also use parallel processing to speed up the computation of the MC source functions.

4.2.1 Synow Fits

Here we investigate a few spherically symmetric distributions of Ca II optical depth. The assumption of homology in the SN atmosphere ($v \propto r$) permits us to parameterize Sobolev optical depth in terms of velocity v relative to the explosion center. In spherical symmetry, we may designate domains $v_{min} < v < v_{max}$ within which we define reference line Sobolev optical depth τ_R according to the rule

$$\tau_R(v) = \tau_R(v_{min}) \exp[(v_{min} - v)/v_e] \qquad (v_{min} < v < v_{max}), \tag{4.1}$$

where v_e is an e-folding length. If v_{min} is greater than the velocity at the photosphere v_{ph}, we say the optical depth profile is *detached*. Outside of the domain we may set the reference optical depth to zero, or use another rule for the same reference line to set up a superposition of optical depth profiles. Other line optical depths for the same ion are assigned assuming excitation temperature T_{exc}. The velocity at the photosphere in all the presented Synow fits is $v_{ph} = 12500$ km s^{-1}.

Synow uses a blackbody emitting photosphere, clearly insufficient to account for all real continuum processes at work in the formation of a SN spectrum. This limits the range over which the synthetic continuum level can be made consistent with that observed, making fits of entire spectra extending from 3000 Å to 10000 Å problematic. We adopt a piecewise approach and choose a convenient blackbody temperature applicable for the blue part of the spectrum. Fitting only the major features blueward of 6000 Å (excluding lines of Ca II), we find that a blackbody temperature $T_{bb} = 12000$ K yields a decent fit to this region. Since increasing T_{bb} from this value changes the continuum slope in the neighborhood of the IR triplet only slightly, we choose to merely scale the synthetic spectra down in order to fit that feature.

Except for the optical depth parameters of Ca II, the other parameters (v_{ph}, T_{bb}, and optical depths of ions listed in Table 4.1) stay fixed from fit to fit. Since the Ca II IR triplet may blend with some lines of O I, a small amount of optical depth for that ion is included in the fit, but its presence has little impact on the results. The parameters used for the various Ca II optical depths are listed in Table 4.2.

Ion	$\tau_R(v_{min})$	v_{min} (10^3 km s^{-1})	v_{max} (10^3 km s^{-1})	v_e (10^3 km s^{-1})	T_{exc} (10^3 K)
Fe III	1.5	12.5	∞	1.0	10.0
Si II	3.5	12.5	∞	1.0	10.0
S II	1.5	12.5	∞	1.0	10.0
O I	0.2	12.5	∞	3.0	8.0

Table 4.1: Synow fit parameters for non-calcium ions.

Fit	(Figure)	N_C	$\tau_R(v_{min})$	v_{min} (10^3 km s^{-1})	v_{max} (10^3 km s^{-1})	v_e (10^3 km s^{-1})
1D1	(4.4)	1	1.4	12.5	30.0	20.0
1D1PV	(4.5)	1	10.0	12.5	∞	3.0
1D1HV	(4.6)	1	20.0	24.0	∞	0.5
1D2	(4.7)	2	10.0	12.5	24.0	3.0
			30.0	24.0	25.0	3.0
1D3	(4.8)	3	16.0	13.0	15.1	3.0
			7.0	19.0	23.5	3.0
			12.0	23.5	∞	3.0

Table 4.2: Synow Ca II Fit Parameters.

One-Component Fits

Here we present three illustrative fits of the Ca II features using only one spherically symmetric velocity component in each. Figure 4.3 shows an example of a fit to the entire spectrum range. The observed features between 4500 Å and 6000 Å are fit rather well assuming the parameters for Fe III, Si II, and S II given in Table 4.1.

In Figure 4.4 are close-ups of the H&K feature and IR triplet fits using model 1D1 from Table 4.2. This single-shell model with nearly constant optical depth as a function of radius can reproduce the broad velocity extent of the H&K feature. Yet it cannot reproduce any of the structure present in the IR triplet, so next we consider independent fits to the PV and HV features to investigate this structure.

The appearance of the two strongest IR triplet lines (Ca II $\lambda\lambda$8542, 8662) in the PV feature as two distinct notches presents an interesting problem under spherical symmetry. In general, without assuming $v_{min} > v_{ph}$ or imposing a finite v_{max}, generating such a feature in spherical symmetry is only possible if $v_{ph} \lesssim v_{sep}$, where v_{sep} is the velocity separation of the two lines. To fit the Si II and Fe III features, $v_{ph} = 12500$ km s^{-1} is used, but v_{sep} for the two strongest IR triplet lines is only about 4000 km s^{-1} and both notches have minimum wavelengths consistent with a 12500 km s^{-1} blueshift.

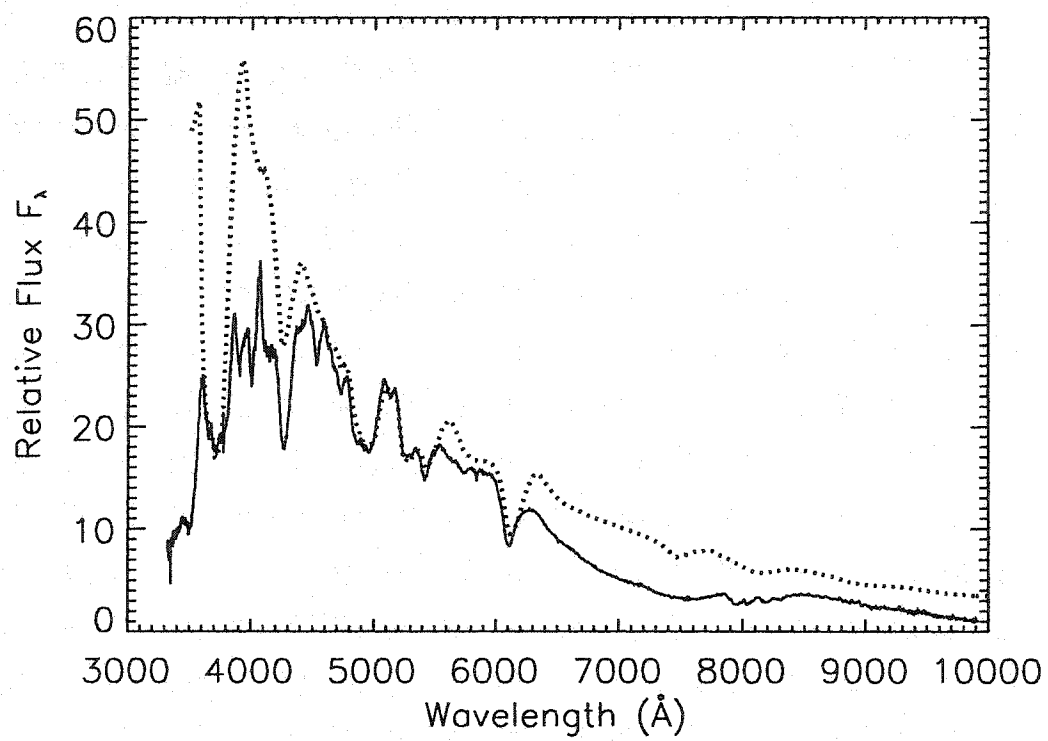

Figure 4.3: `Synow` fit 1D1 (dotted line) of SN 2000cx (solid line) two days after maximum with one Ca II component. Optical depths and excitation temperatures used for the other ions (Fe III, Si II, S II, and O I) are as listed in Table 4.1.

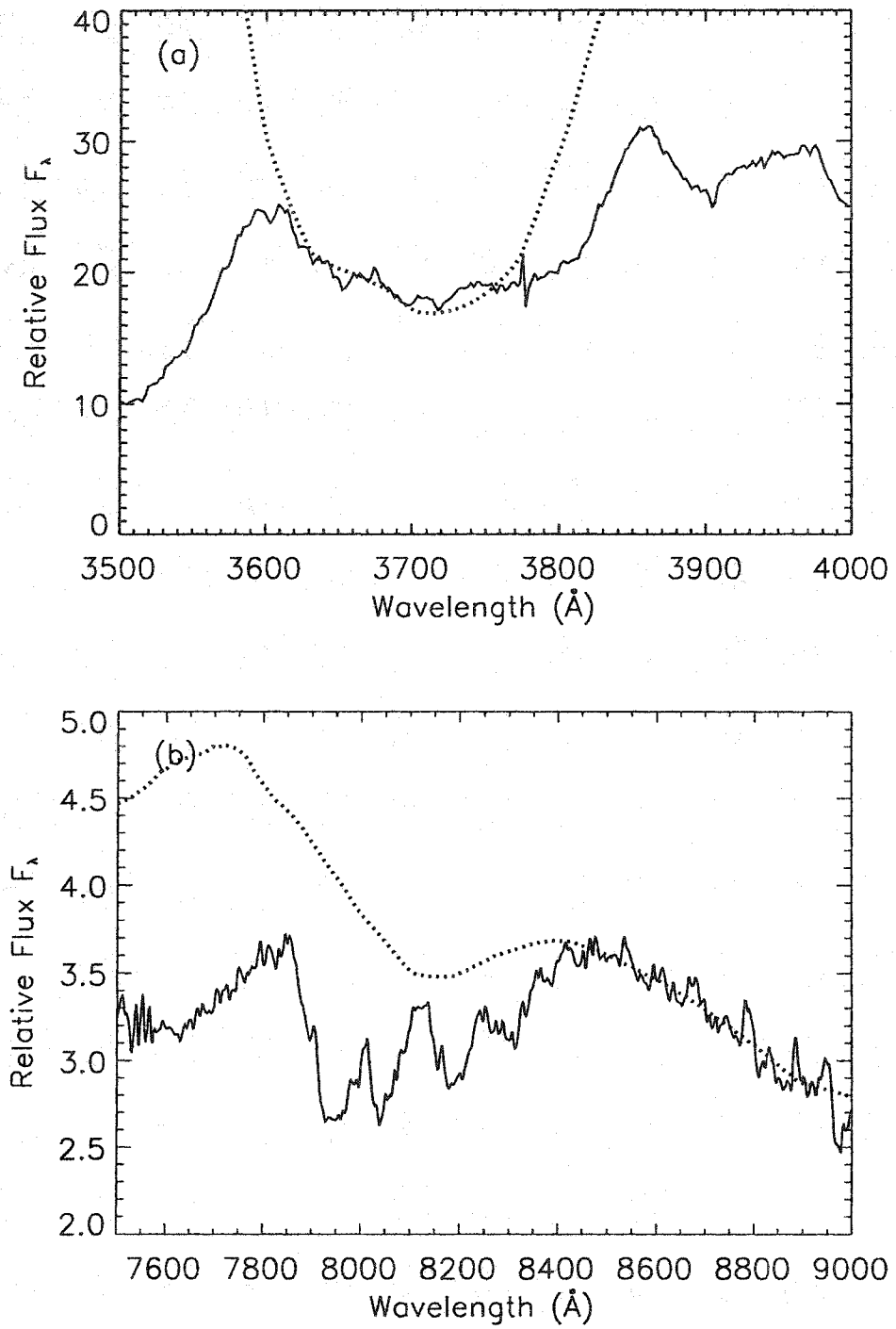

Figure 4.4: Synow fit 1D1 (dotted line) of Ca II features in SN 2000cx (solid line) two days after maximum. A single, nearly constant optical depth shell extending from the photosphere to 30000 km s^{-1} is used. The velocity extent of Ca II H&K is approximately reproduced, but the synthetic IR triplet lacks any of the structure seen in the observed spectrum.

An alternative is to impose a finite v_{max} or small v_e that prevents blending of the two absorptions into one. But this has the undesirable effect of making absorptions with flat bottoms which (when combined together) generate a Ca II λ8542 feature *shallower* than the redder line, even though the former has a higher oscillator strength. For the moment, we allow the features to blend into one absorption, using the parameters listed for fit 1D1PV in Table 4.2 which provide a satisfactory fit to the PV features in Figure 4.5.

Fitting the HV notches with a shell of Ca II optical depth (fit 1D1HV in Figure 4.6) is considerably less problematic than in the case of the PV feature. Using a small v_e or imposing a finite v_{max} prevents blending that would otherwise unite the two bluer notches of the IR triplet feature.

Two-Component Fit

Combining the one-component PV and HV fits described above yields fit 1D2 (Figure 4.7). This fit is satisfactory for the IR triplet, but its major deficiency is that the peak between the two blue notches is higher than observed. Adjusting v_{max} from 25000 km s^{-1} to higher velocity permits the redder feature to weaken this peak, extends the bluest synthetic notch further to the blue than is desired. On the other hand, the synthetic H&K feature appears to need some higher-velocity material to extend its blue edge.

Three-Component Fit

Using three velocity components of Ca II optical depth allows us to fit every notch in the IR triplet absorption by simply overlapping pairs of notches formed by each component. The result of this model (1D3) is displayed in Figure 4.8. For the IR triplet, this appears to be the "best fit" among the 1D models, but the H&K feature

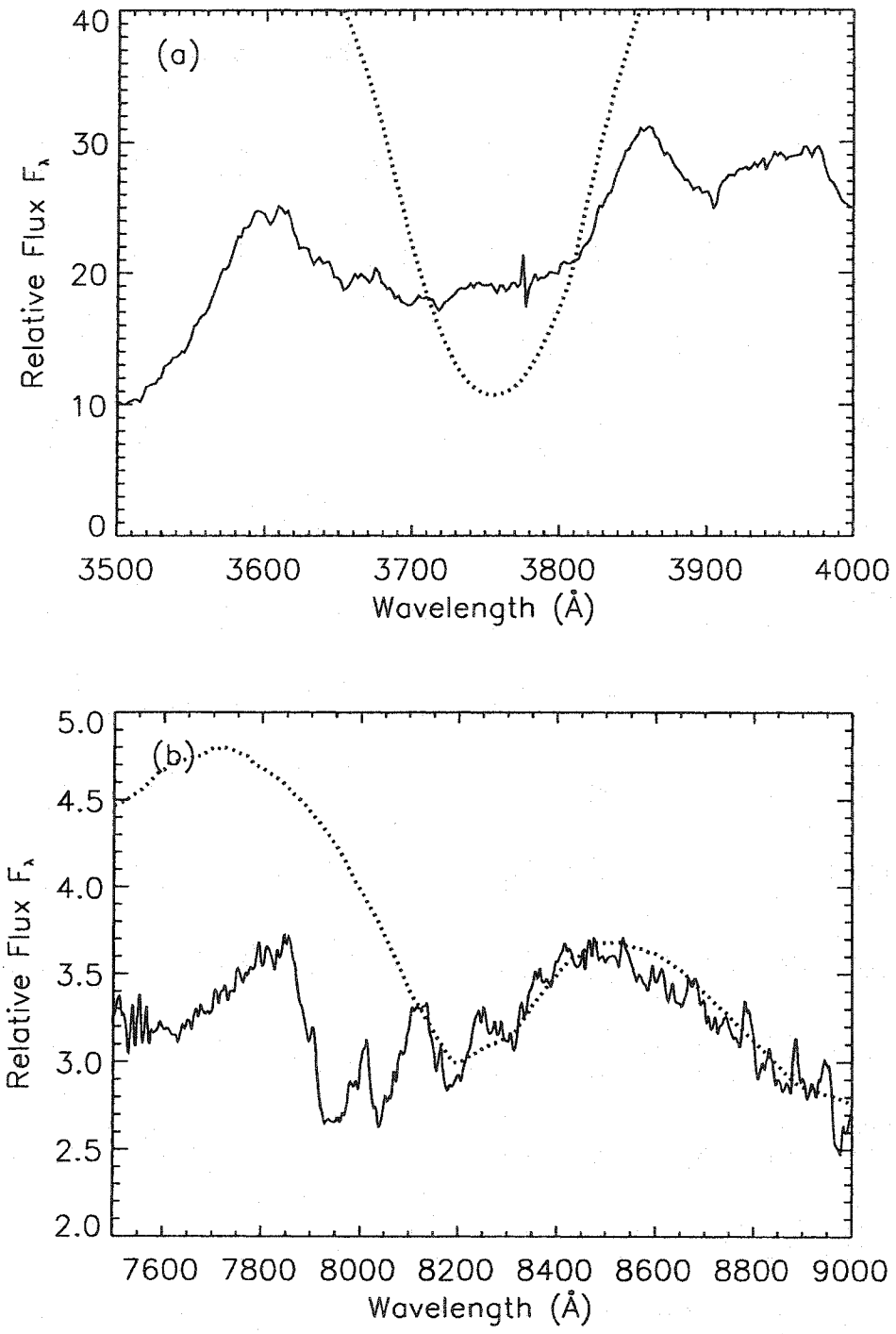

Figure 4.5: Synow fit 1D1PV (dotted line) of Ca II features in SN 2000cx (solid line) two days after maximum. A single, exponentially decreasing optical depth component just above the photosphere is used.

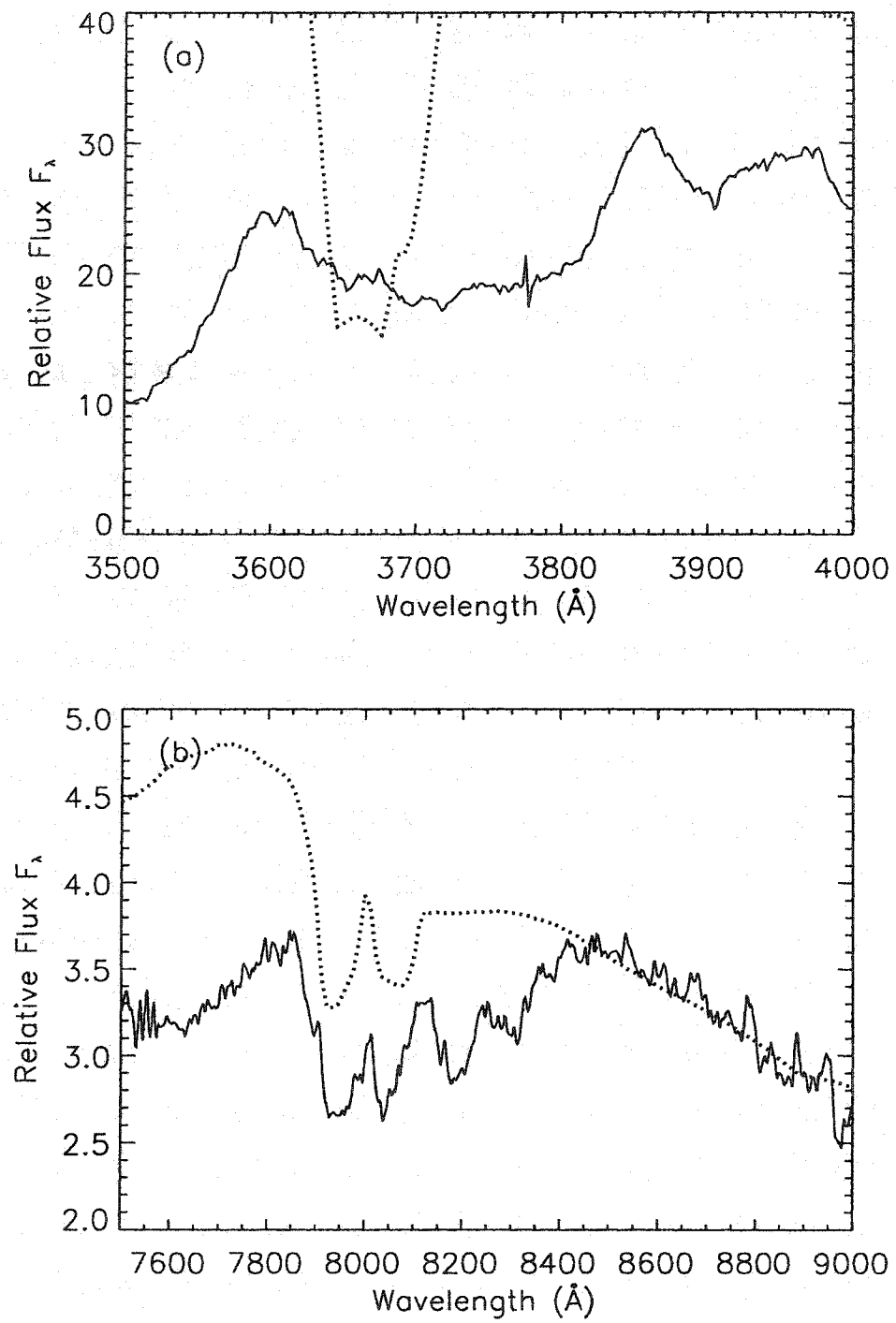

Figure 4.6: Synow fit 1D1HV (dotted line) of Ca II features in SN 2000cx (solid line) two days after maximum. A single, exponentially decreasing optical depth component at 20000 km s^{-1} is used. An extremely small e-folding velocity of 500 km s^{-1} is needed to prevent blending.

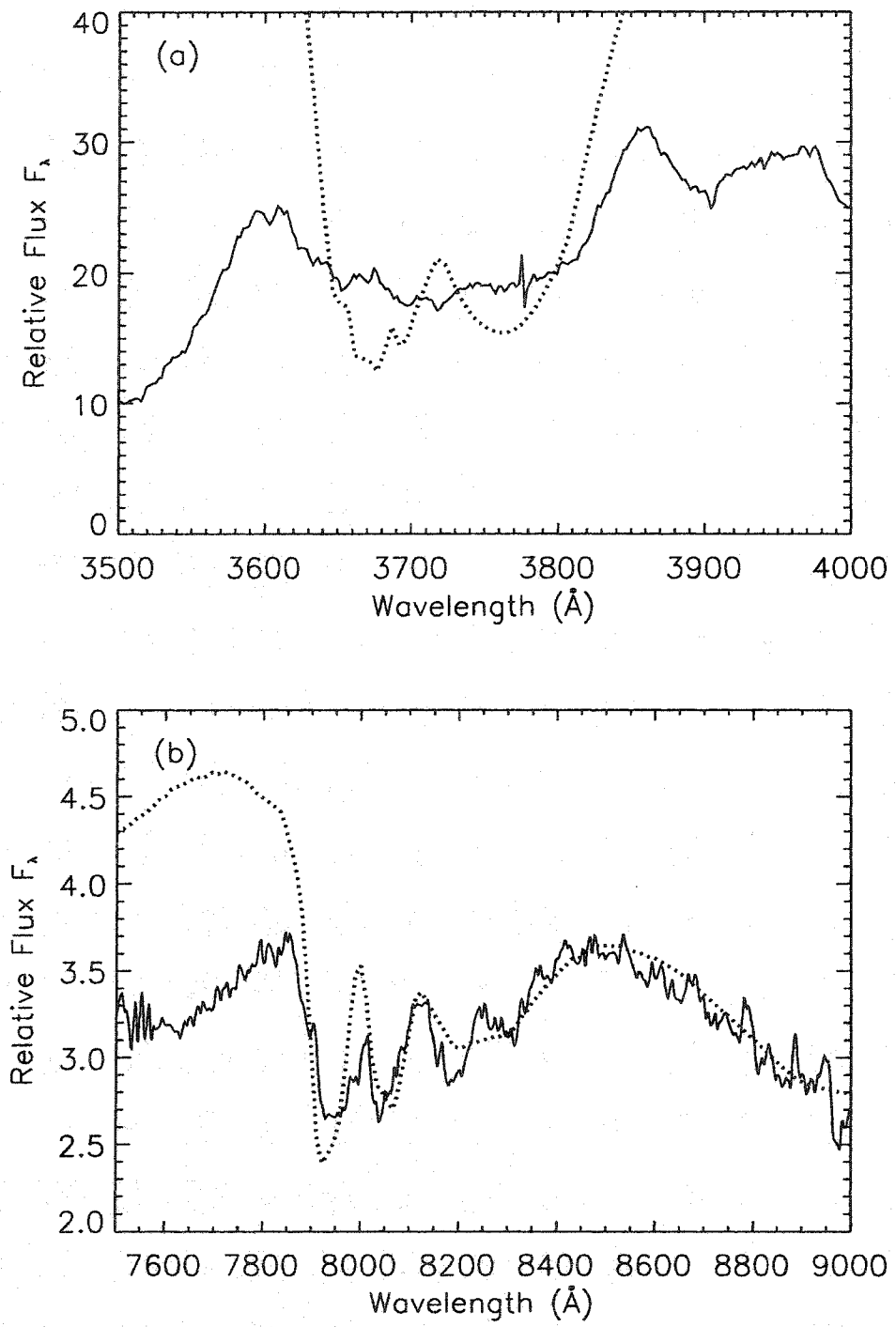

Figure 4.7: Synow fit 1D2 (dotted line) of Ca II features in SN 2000cx (solid line) two days after maximum. Two exponentially decreasing shells of Ca II optical depth are used. One extends from the photosphere to 24000 km s^{-1} and the other from 24000 km s^{-1} to 25000 km s^{-1}.

is too strong in its bluest part. Imposing a finite v_{max} to counteract this HV tail only deepens the synthetic H&K absorption since it removes material that scatters light from the emission lobes of the envelope.

4.2.2 synBrute Fit

The spatial parameterization used for the 3D Ca II optical depth consists of two components. One is spherical (PV material) and the other is not (HV material). The idea is to engineer a simple 3D distribution of optical depth that yields a synthetic spectrum consistent with observation, and fits at least as well as the 1D model.

For the HV material in the 3D fit, we adopt a simple geometry consisting of a circular cylinder of radius 8000 km s^{-1} coaxial with the line of sight to the center of the photosphere. The reference optical depth for Ca II inside the cylinder is assigned according to the rule

$$\tau_R(v_z) = \begin{cases} 0.0225v_z - 441.0 & : \quad 19600 < v_z < 22400 \quad \text{km s}^{-1} \\ -0.0315v_z + 768.6 & : \quad 22400 < v_z < 24400 \quad \text{km s}^{-1}. \end{cases} \tag{4.2}$$

According to this rule, the optical depth in the cylinder reaches a maximum value of $\tau_R = 63$ at the plane $v_z = 22400$ km s^{-1}. Outside the cylinder, the optical depth for the Ca II reference line is prescribed by Equation (4.1) with $\tau_R(v_{min}) = 7$, $v_e = 3000$ km s^{-1}, and $v_{min} = 13000$ km s^{-1}. A plot of reference optical depth along the line of sight is presented in Figure 4.9. The reference optical depths of the other ions are parameterized exactly as in the Synow fits and produce the same features.

The Ca II features resulting from this 3D parameterization are shown in Figure 4.10. The fit to the HV IR triplet is rather good. The synthetic HV H&K is more consistent with the observation than in the 1D2 or 1D3 parameterizations. Since the

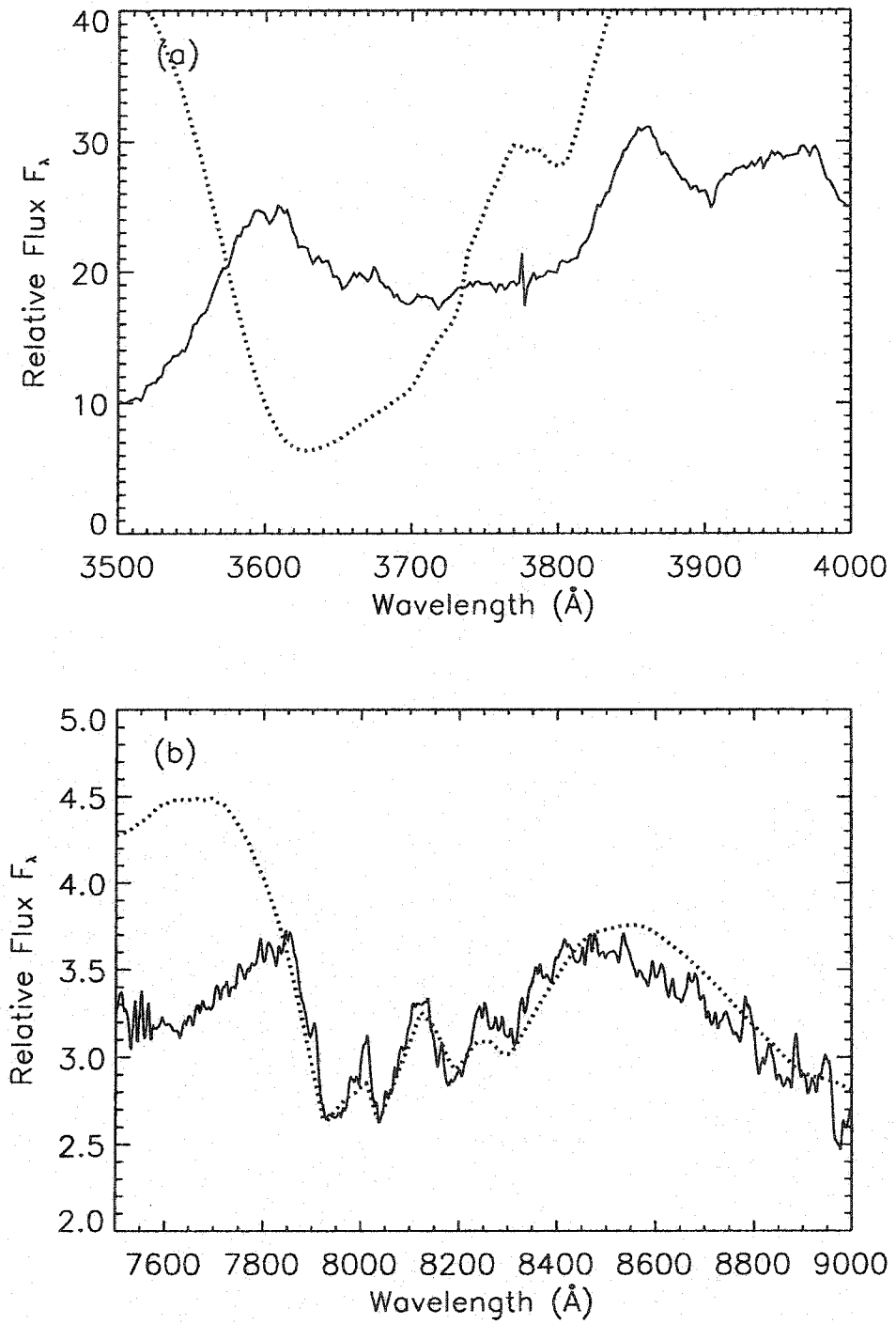

Figure 4.8: Synow fit 1D3 (dotted line) of Ca II features in SN 2000cx (solid line) two days after maximum. Three exponentially decreasing shells of Ca II optical depth are used to generate the peak between the two red notches of the triplet. The synthetic H&K feature is too strong compared to the observed one.

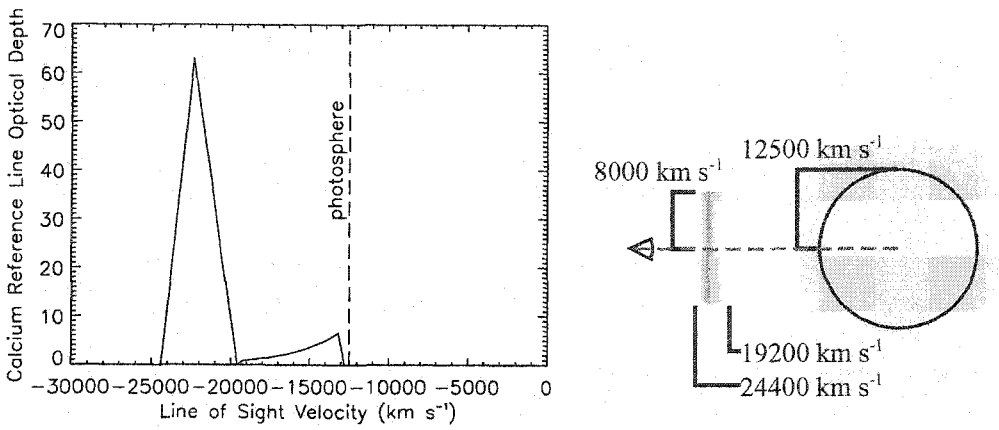

Figure 4.9: Ca II reference line optical depth along the $-z$ axis in the 3D model.

PV Ca II optical depth is distributed much the same as in the 1D2 case, the weak observed peak between the redder notches cannot be reproduced. In the 1D case, this could only be accomplished by adding a third shell of optical depth and tuning its position. We note that in the 3D case, if the PV material is deployed in a nonspherical manner (such that parts of the photosphere shine through) then the peak between the two PV notches can be reproduced quite easily.

4.3 Discussion

4.3.1 HV Ejecta Geometry from the Fits

Reconstructing SN envelope structure from spectra is an ill-posed inverse problem. The problem becomes even more difficult when the assumption of spherical symmetry is relaxed; the presented 3D solution represents but one of many possible solutions.

In fact, to first order, any HV distribution of Ca II optical depth which yields the same photospheric covering factor as a function of v_z will produce the same absorption features. The most promising avenue for breaking this degeneracy is through synthetic spectropolarimetry of high-quality data. The Stokes polarization parameters Q and

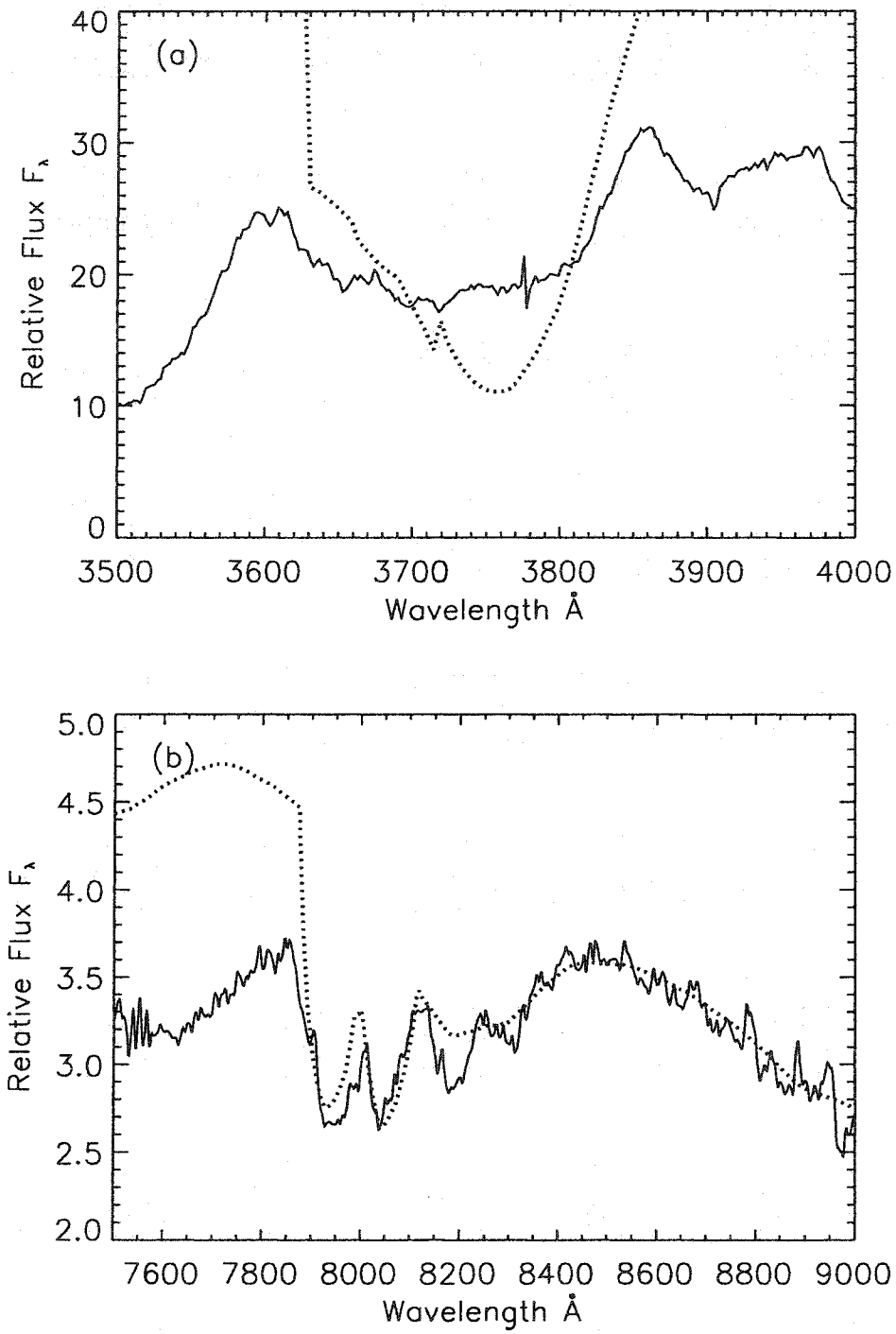

Figure 4.10: `synBrute` fit (dotted line) of Ca II features in SN 2000cx (solid line) two days after maximum. The IR triplet is fit, and the blue edge of the synthetic H&K feature is weakened with respect to fit 1D3.

U for wavelengths covering the Ca II features are required. Such Q-U plots are the means by which the HV ejecta geometry of SN 2001el is constrained (Kasen et al., 2003).

Both that study and the present one focus on the absorption features of Ca II, and ignore the emission features. Generally, emission phenomena are of limited utility in assessing HV ejecta geometry. In spherical symmetry, a HV shell gives rise to a weak, flat-topped emission feature barely detectable in flux spectra. On the other hand, if the HV ejecta are organized into isolated regions of high optical depth, those not covering the photosphere along the line of sight will only contribute individual emission bumps to the spectrum. These weak features are even harder to detect if the PV ejecta are spherically symmetric and contribute significantly to the emission feature.

On the practical side, the peculiarities of the spectrum of SN 2000cx make it impossible to use the Ca II emission features for geometrical analysis. The H&K emission feature is disrupted by a sequence of narrow lines, while the IR triplet emission is plagued by fringing.

These factors (the inherent degeneracies of the problem, the lack of corroborating polarization data, the limited utility of emission features) prevent us from making all but the most conservative statements about the HV ejecta geometry of SN 2000cx. The similarity of the HV IR triplet of SN 2000cx to that of SN 2001el is suggestive, and its geometrical interpretation in the latter event motivates our consideration of a 3D model for SN 2000cx.

From a purely empirical standpoint, none of the presented fits stands out as the "best" overall. Any cosmetic details missed by the synthetic spectra could be tuned away by making minor adjustments to the models. However, the main goal is to simultaneously fit the HV H&K and IR triplet, and the 3D fit seems to do a better job.

Regardless of the details of the true geometry of the HV Ca II in SN 2000cx, the presence of this feature in only some SNe Ia evokes a series of questions to address in the future as high-quality data become available and 3D spectrum analysis techniques improve.

(1) How frequent is HV ejecta clumping in SNe Ia? All SNe Ia might possess HV deviation from spherical symmetry which could escape detection if optically thick parts did not obscure the photosphere. SNe 2001el and 2000cx might be examples where fortuitous orientation of HV ejecta permitted detection. This explanation is bolstered by the otherwise normal appearance of the SN 2001el spectrum. However, the peculiarities of SN 2000cx (the Fe III lines in its spectrum, its unusual light curve and color evolution; Li et al., 2001a) make this hypothesis somewhat problematic.

(2) What implication does the presence of clumpy HV ejecta have for explosion models? If some SNe Ia have nonspherical HV ejecta while others do not, it might imply that more than one progenitor model is needed to explain the SN Ia phenomenon. More conservatively, the clumpiness of the HV ejecta might be a consequence of a so-called second parameter (Branch, 2001).

(3) Does the existence of nonspherical SNe Ia influence the prospects for precision SN cosmology? The most obvious spectroscopic effect would be due to the application of spherical K-corrections to nonspherical events. This effect is probably minor unless the consequences for spectrum formation from geometry appear in more than just a few lines.

Ca II lines are notoriously excitable over a large range of temperature and density. This makes it possible to place limits on the HV ejecta mass, and in turn to constrain future white dwarf explosion models.

4.3.2 HV Ejecta Mass Estimates

Here we make some simple estimates of the HV ejecta mass as constrained by the Ca II features visible in the SN 2000cx spectrum at two days after maximum light. We make two pairs of estimates, each pair consisting of a 1D and 3D measurement. The first pair of estimates is made for the extreme case of a purely calcium HV ejecta composition. The second pair is based on a C/O-rich composition, similar to the outer, unburned layers of a white dwarf. This details of this composition are as listed in the SN ion signatures atlas of Hatano et al. (1999b).

For each pair of estimates, we adopt the 1D2 and 3D parameterization domains for the volume used in calculating the HV ejecta mass. These are

$$\begin{aligned} V_{HV}^{1D2} &= 3.9 \times 10^{46} \quad \mathrm{cm}^3, \\ V_{HV}^{3D} &= 5.0 \times 10^{45} \quad \mathrm{cm}^3. \end{aligned} \tag{4.3}$$

These presented mass estimates are not intended to be exact; in all cases the assumption of thermal equilibrium (TE) is employed. More rigorous constraints on the HV ejecta mass require detailed modelling of the physical conditions in the HV material, and these will be the focus of much future work. The estimates here and in Kasen et al. (2003) are a starting point for that effort.

Pure Calcium Composition

Recall that in the Sobolev approximation, line optical depth for the transition $l \rightarrow u$ in a SN envelope is given by

$$\tau_{lu} = 2.292 \times 10^{-5} (gf)_{lu} \lambda_{lu}^{A} n t_d \frac{\exp(-E_l/kT)}{Q(T)}, \tag{4.4}$$

where we have neglected the correction factor for stimulated emission, replaced the constants with their numerical values, and imposed TE.

If the HV ejecta consist of singly ionized calcium in the ground state, then the optical depth in the Ca II λ3934 transition (the reference line) becomes roughly proportional to the mass density of the HV ejecta. In reality, the gas consists of other ions of calcium and other species, so deriving a mass density assuming a pure Ca II composition provides an extreme lower limit to the HV mass. Substituting $\lambda_{lu}^{A} = 3934$, $(gf)_{3934} = 1.3614$, $E_l = 0$ eV, and $t_d = 20$ into Equation (4.4) gives

$$\tau_{3934} \simeq 2.46 n_{CaII}/Q(T). \tag{4.5}$$

If we assume that the temperature in the HV ejecta is less than 8000 K, we can use the simple approximation $\tau_{3934} \simeq n_{CaII}$ since $Q(T)$ varies slowly from 2 to 3 up to 8000 K.

Now an average mass density for the HV ejecta as derived from the Ca II optical depth can be written

$$\langle \rho_{HV} \rangle \simeq (A_{Ca}/N_{Avo}) n_{Ca} \simeq 6.66 \times 10^{-23} \langle \tau_{HV} \rangle \text{ g cm}^{-3}. \tag{4.6}$$

If we average the reference line optical depths over the 1D2 and 3D parameterization domains, then $\langle \tau_{HV}^{1D2} \rangle = 25.5$ and $\langle \tau_{HV}^{3D} \rangle = 31.5$. Substituting these values into Equation (4.6) and multiplying by the volume in each case,

$$\begin{aligned} M_{HV}^{1D2} &\gtrsim 3.3 \times 10^{-8} M_{\odot}, \\ M_{HV}^{3D} &\gtrsim 5.2 \times 10^{-9} M_{\odot}. \end{aligned} \tag{4.7}$$

These mass estimates are the "rock bottom" numbers required for the observational

signature of the Ca II λ8542 line. The deflagration model W7 (Nomoto et al., 1984; Branch et al., 1985) suggests that the amount of material and the densities in this region should be much higher, on the order of $6.0 \times 10^{-3} M_{\odot}$ in spherical symmetry above 20000 km s^{-1}. Including other species into the mass calculations improves the lower limit, but this requires a choice of a particular composition.

C/O-Rich Composition

A more realistic composition model than that of pure calcium can be used to produce a more meaningful constraint on the HV ejecta mass. Here we adopt the C/O-rich composition from the ion signature atlas of Hatano et al. (1999b) as the candidate model. This composition is representative of the unburned outer layers of an exploded white dwarf.

The procedure for constraining the HV mass density is quite simple. First we solve the equation of state for a range of values of temperature T and density ρ_{tot}. Then we find regions of the $T - \rho_{tot}$ plane for which the optical depth of Ca II λ8542 exceeds unity. The lowest total mass density for which this line has a non-negligible optical depth will provide a lower limit to the HV mass density, and from this we derive a lower limit to the HV ejecta mass.

Contours of $\tau = 1$ for Ca II λ3934 and λ8542 are shown in Figure 4.11. For the C/O-rich composition, the absolute minimum mass for which Ca II λ8542 has a spectroscopic signature is at $\rho_{min}^{C/O} = 2.2 \times 10^{-16}$ g cm^{-3}. This density is marked by a dotted vertical line.

The value of $\rho_{min}^{C/O}$ depends on the choice of T, as does the relative strength of Ca II λ8542 to λ3934. However, since the optical depth of Ca II λ3934 is always much greater than that of the IR line, it is difficult to constrain the exact value of T in the HV ejecta using this technique. As τ in a line approaches ∞, the line profile saturates and the dependence of the absorption feature depth on τ disappears. Rather than

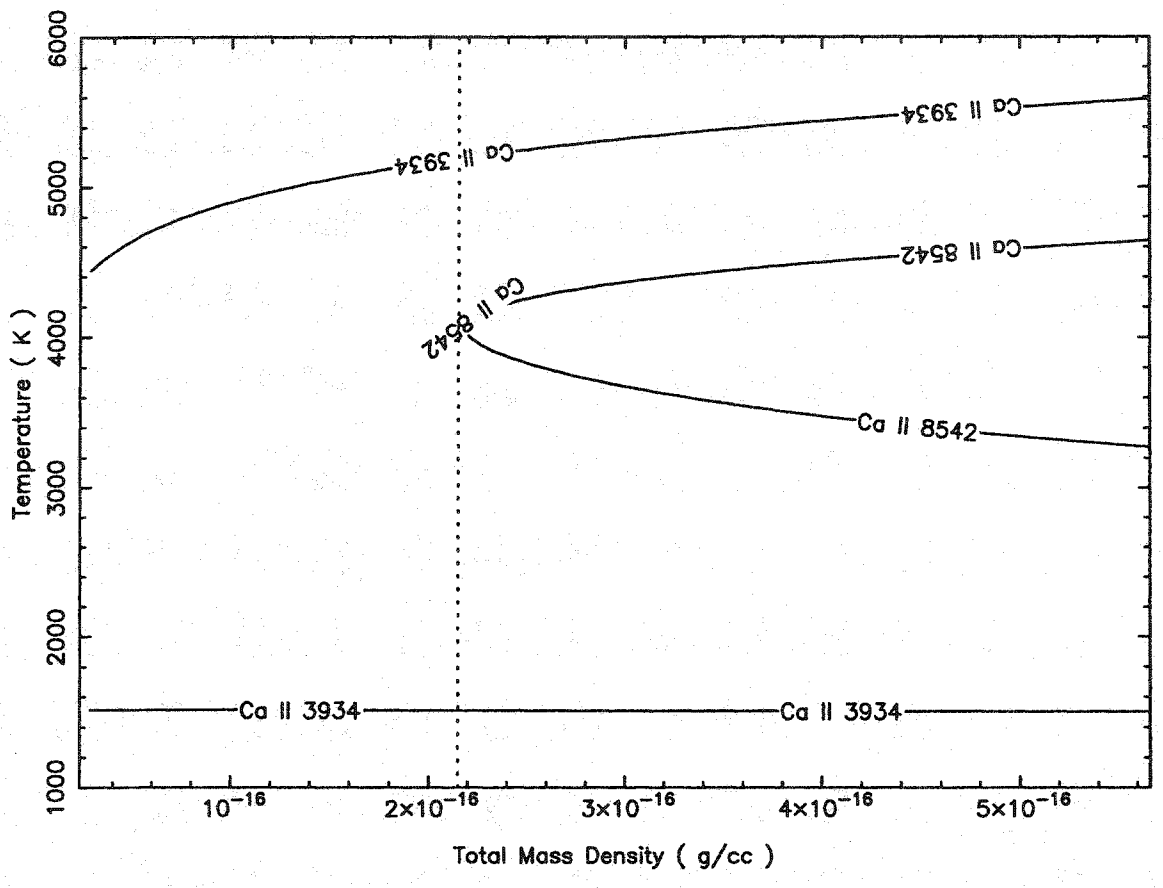

Figure 4.11: Contours of $\tau = 1$ for Ca II λ3934 and λ8542, assuming the C/O-rich composition. The dotted line denotes $\rho_{min}^{C/O} = 2.2 \times 10^{-16}$ g cm^{-3}.

resort to predictions from detailed models for a temperature in the HV ejecta, we adopt the absolute minimum value given above for a conservative estimate of the HV ejecta masses:

$$\begin{aligned} M_{HV}^{1D2} &\gtrsim 4.3 \times 10^{-3} M_{\odot}, \\ M_{HV}^{3D} &\gtrsim 5.5 \times 10^{-4} M_{\odot}. \end{aligned} \tag{4.8}$$

These mass estimates and densities are roughly consistent with the W7 estimate of $6.0 \times 10^{-3} M_{\odot}$ in spherical symmetry above 20000 km s^{-1}. This might suggest that the Ca II signature could arise from primordial material as was suggested for SN 1994D (Hatano et al., 1999a), rather than from freshly synthesized material.

As the density increases from $\rho_{min}^{C/O}$, lines of Ti II, Sr II, and Fe II should appear for higher temperatures, while lines of Fe I and Ca I should appear at lower temperatures, as seen in Figure 4.12. The lower-excitation lines are certainly missing from the spectrum, but the identification of lines from the higher ionization stages is problematic. The Ti II lines could be present to the blue of the 4300 Å Fe III feature, but this identification is uncertain. Sr II lines from HV ejecta blend with the Ca II H&K feature. Fe II lines would be heavily blended with the Fe III features. These uncertainties prevent us from using Figure 4.12 to cap the value of $\rho_{HV}^{C/O}$.

Other Compositions

Marietta et al. (2000) present interesting simulations of the effect that a white dwarf in a binary has on its companion when it explodes. Generally, they note that more evolved companions (with less tightly bound envelopes) are more vulnerable to losing a substantial fraction of their envelope during the explosion. The resulting ejecta distribution includes an evacuated cone in the ejecta behind the companion and some hydrogen with characteristic velocity on the order of 1000 km s^{-1}. However, a small amount of stripped hydrogen (about $10^{-4} M_{\odot}$) could be carried up to velocities ex-

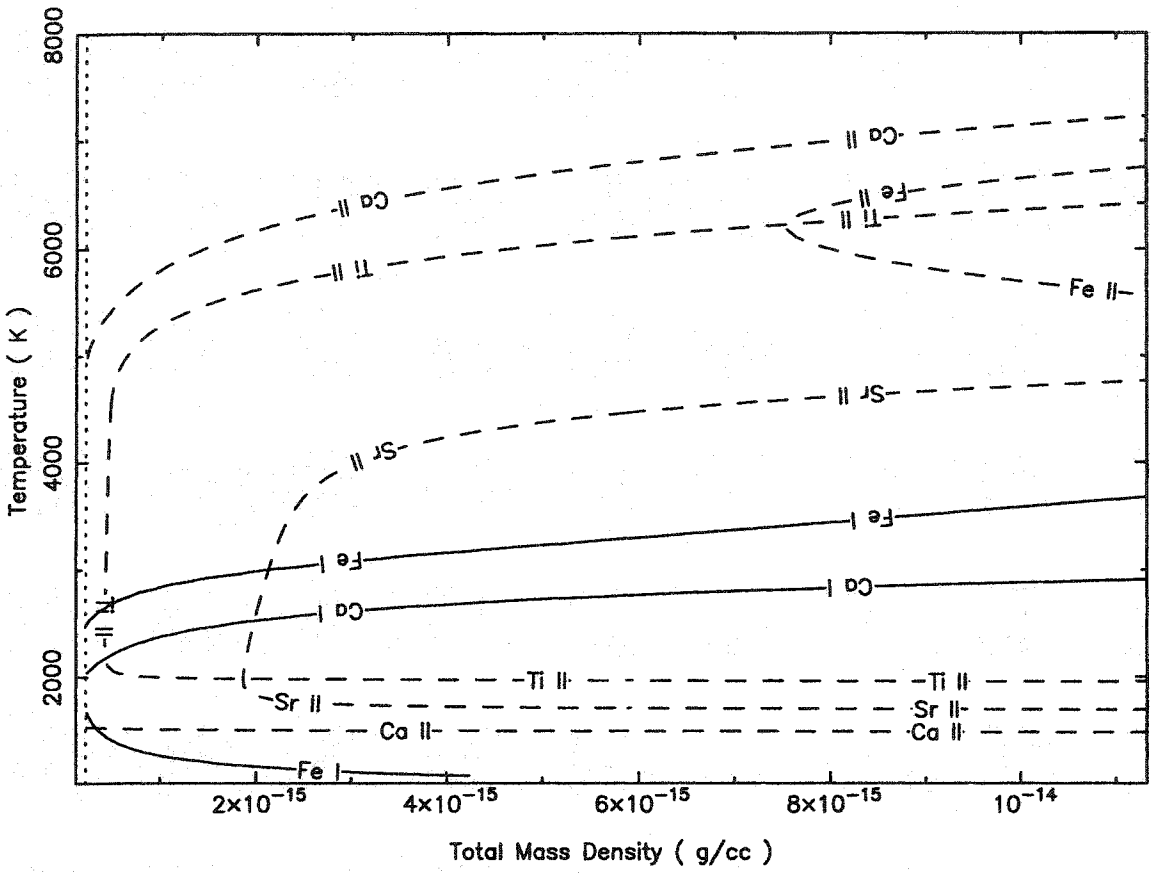

Figure 4.12: Contours of $\tau_R = 1$ of various ions in the C/O-rich composition. Neutral ions are represented with solid contours, and singly ionized ones with dashed contours. The dotted line denotes $\rho_{min}^{C/O} = 2.2 \times 10^{-16}$ g cm^{-3}.

ceeding 15000 km s^{-1}. Could the HV Ca II lines be a signature of this material?

The required minimum density for an optical depth of 1 in Ca II is 45% higher than in the C/O-rich case, and the density for which Hα optical depth becomes unity is only 4 times higher than that. This leaves a rather narrow density window in which to form the HV Ca II without also producing an Hα signature, if the Hα signature were to be produced under the assumption of TE.

It is an observational fact, however, that Hα in SNe II is generally in net or total emission (see, for example, spectra of SN 1999em – Hamuy et al., 2001; Leonard et al., 2002; Elmhamdi et al., 2003), an effect which cannot be replicated by a direct analysis code which uses pure resonance scattering line source functions where line flux is conserved except for occultation effects. However, pure resonance scattering is sufficient for simultaneous, satisfactory fits of Hβ and Hγ in these objects (e.g., Baron et al., 2000, where synthetic Hα is permitted to remain too deep compared to observations in Synow fits of SN 1999em).

If the HV ejecta in SN 2000cx were a clump of HV H-rich material blocking the photosphere, then the usual Hα phenomenon has the interesting consequence described for net emission lines in Chapter 3. Assuming pure resonance scattering for all the Balmer lines, this material would produce HV Hα and Hβ absorption features at the same velocities as the HV Ca II features. The blueshifts are such that the HV Hα absorption falls into the Si II feature near 6100 Å. But the net emission phenomenon will mitigate the strength of the Hα absorption and further conceal the hydrogen signature. We would expect the Hβ feature to remain in absorption, however.

In Figure 4.13, we show a fit to the entire spectrum with hydrogen in the 3D HV ejecta. The hydrogen reference line (Hα) optical depth used for this spectrum has a velocity-space profile similar to that described in Equation (4.2) except that the maximum optical depth at $v_z = 22400$ km s^{-1} is $\tau_R = 4$. As predicted, the

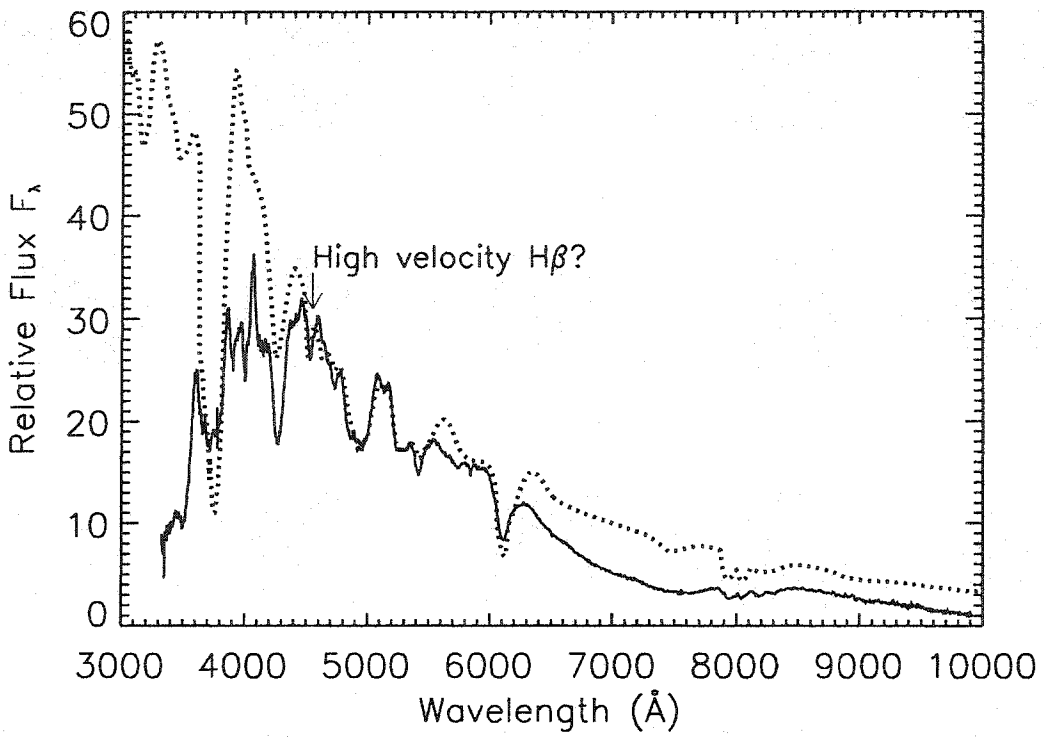

Figure 4.13: `synBrute` fit to SN 2000cx spectrum at two days after maximum, including H optical depth in the HV clump. Hα absorption is concealed in the Si II absorption at 6100 Å, and this could be completely erased by net emission.

assumption of pure resonance scattering produces a readily apparent modification to the Si II absorption feature which would be ameliorated by the net emission effect. Additionally, a previously unidentified feature at 4500 Å is fit by the synthetic HV Hβ.

Note that this signature is only possible if the HV hydrogen is confined to a clump blocking the photosphere. If the HV hydrogen is placed into a HV shell, a strong emission feature centered at Hα will appear. This is clearly not the case in the spectra of SN 2000cx. Other candidate ions for fitting this line simply fail, as discussed in a 1D direct analysis of this object (D. Branch et al., in preparation). This fit is included here since it is contingent upon the 3D distribution of hydrogen at HV we describe.

If the 4500 Å feature is HV Hβ, and we dispense with the assumption of TE for the hydrogen lines, then we see that the lower level of Hβ could potentially be over-populated. This reduces the amount of HV ejecta required to produce an Hβ feature by a factor equal to the departure coefficient of the lower level of this transition. This reduces the gap between the HV masses estimated in this work and those predicted by (Marietta et al., 2000). But can NLTE effects bridge this gap? Future detailed 3D NLTE calculations are required to answer this question.

Another scenario for the production of a SN Ia is through recurrent novae (Starrfield, 2003) or supersoft x-ray sources (Hachisu et al., 1999). These progenitors involve a He-rich (and H-deficient) companion star. Minimum mass estimates for this case suggest HV ejecta masses about the same as in the H-rich case, assuming TE. But since helium stars are more tightly bound than those simulated by Marietta et al. (2000), mass stripping from a He-rich companion seems less likely an origin for the HV material.

Arguments in favor of a circumstellar origin fall short. The spectroscopic signature for that material is completely different from what is seen in the case of SN 2000cx. In that case, we expect a narrow Hα emission spike, not unlike that found in SNe IIn.

4.4 Summary

We have presented several exploratory fits to the unique Ca II features of the unusual SN Ia 2000cx. A 1D shell of material can account for the HV IR triplet feature, but has difficulty doing so for the corresponding H&K feature. In 3D, both HV features can be fit simultaneously with a chunk of material along the line of sight which partially covers the photosphere.

Assuming a C/O-rich composition, mass estimates for the HV ejecta in both geometries discussed are consistent in the lower limit with the W7 model, suggesting

a possible primordial origin. If the HV ejecta is H-rich, however, the mass required at HV to produce the observed Ca II features is somewhat higher. There is circumstantial evidence for the HV ejecta being H-rich, pointing to a signature of stripping from a companion star. This model is more favorable when NLTE effects are taken into account, but confirmation requires detailed 3D spectrum synthesis which is not currently feasible.

Understanding the origin and geometry of the HV ejecta in SNe Ia (and also its frequency and physical conditions) is potentially quite important for future explosion models and for answering the progenitor question. It is clear that better constraints on the HV Ca II phenomenon require high-quality flux and polarization spectra at near-infrared and near-ultraviolet wavelengths.

Chapter 5

3D LTE Modelling

The previous two Chapters discussed parameterized applications of the 3D ES model. In the `tauBrute` code, spatial parameterization of Sobolev optical depth is specified directly for a list of given wavelengths. The `synBrute` code is useful for spectrum fitting without assuming spherical symmetry; it assigns line optical depths for many lines using the Kurucz (1993) line list, assuming TE. The use of such parameterized methods in 1D is well-established; their use in the 3D situation should prove fruitful as well, since they provide a sort of geometrical reality check for multidimensional explosion modellers.

In this Chapter, we discuss some first steps beyond such parameterized 3D methods, with emphasis on theory and implementation. Included are example 1D and 3D results. These steps represent an effort to develop 3D detailed spectrum synthesis techniques for evaluating future explosion models.

The eventual goal is to construct a 3D analogue to the 1D `PHOENIX` code (at least an analogue to its SN mode). This entails the inclusion of all the relevant transfer physics (solution to the full comoving RTE, inclusion of continuum transfer, determination of transition rates and level populations without recourse to approximation).

Many simplifying assumptions currently used in `Brute` will be discarded, including (probably) the Sobolev approximation.

Our first small goal is to dispense with the *ad hoc* assignment of Sobolev optical depths and individual ion excitation temperatures. We seek a more self-consistent approach to modelling the 3D SN atmosphere. Ideally, we should be able to specify an explosion model (density and composition) and a bolometric luminosity. The model atmosphere would then work out the details of the interaction between the matter and radiation field subject to the law of energy conservation.

Computational limitations, however, prevent us from moving away from the assumption of TE. Instead, we fully embrace the more general assumption of local thermodynamic equilibrium (LTE). This permits us to describe the matter state in the model atmosphere with just two state variables (number density and temperature) and a specified abundance. A more accurate (non-LTE or NLTE) treatment of the problem increases the number of state variables to the order of 10^6. Despite the difficulties in reconciling LTE with a real model atmosphere, the assumption of LTE is powerful and sweeping, and permits us to build intuition that will assist us when we move to 3D NLTE modelling.

In fact, for some situations, it turns out that the assumption of LTE is not so bad after all. While core collapse SN spectra are dominated by highly NLTE hydrogen lines, the species contributing to SN Ia spectra can be described well in LTE. The more self-consistent LTE 3D modelling version of `Brute` we call `lteBrute`.

5.1 Radiative Equilibrium

Recall that the time-independent form of the RTE is

$$\hat{n} \cdot \vec{\nabla} I(\vec{r}, \hat{n}, \lambda) = \eta(\vec{r}, \hat{n}, \lambda) - \chi(\vec{r}, \hat{n}, \lambda) I(\vec{r}, \hat{n}, \lambda). \tag{5.1}$$

If we integrate the left hand side over angle and wavelength, we obtain a condition on the total flux,

$$\oint d\Omega \int_0^\infty d\lambda \left\{ \hat{n} \cdot \vec{\nabla} I(\vec{r}, \hat{n}, \lambda) \right\} \equiv 4\pi \vec{\nabla} \cdot \vec{H}(\vec{r}). \tag{5.2}$$

Rewriting the right hand side of the RTE in terms of the source function $S(\vec{r}, \hat{n}, \lambda)$, we have

$$\eta(\vec{r}, \hat{n}, \lambda) - \chi(\vec{r}, \hat{n}, \lambda) I(\vec{r}, \hat{n}, \lambda) = \chi(\vec{r}, \hat{n}, \lambda) \Big[S(\vec{r}, \hat{n}, \lambda) - I(\vec{r}, \hat{n}, \lambda) \Big]. \tag{5.3}$$

Since we are treating line transfer only in the Sobolev approximation, we write the extinction coefficient as a series of non-overlapping line profiles. That is, each line profile function is at effectively $\Delta\lambda = \pm\infty$ to its nearest neighbor lines. We break the extinction into a sum over all lines $1 \leq l \leq L$,

$$\chi(\vec{r}, \lambda) = \sum_{l=1}^{L} \bar{K}_l(\vec{r}) \phi_l(\lambda). \tag{5.4}$$

The assumption of non-overlapping lines permits us to break the wavelength integration of the right hand side of the RTE into a sum of independent integrals.

$$\begin{aligned} 4\pi \vec{\nabla} \cdot \vec{H}(\vec{r}) &= \oint d\Omega \int_0^\infty d\lambda \Big\{ \Big[\sum_{l=1}^{L} \bar{K}_l(\vec{r}) \phi_l(\lambda) \Big] \Big[S(\vec{r}, \hat{n}, \lambda) - I(\vec{r}, \hat{n}, \lambda) \Big] \Big\} \\ &= \sum_{l=1}^{L} \bar{K}_l(\vec{r}) \oint d\Omega \int_0^\infty d\lambda \Big\{ \phi_l(\lambda) \Big[S(\vec{r}, \hat{n}, \lambda) - I(\vec{r}, \hat{n}, \lambda) \Big] \Big\}. \end{aligned} \tag{5.5}$$

In the Sobolev approximation, we take $S(\vec{r}, \hat{n}, \lambda)$ to be constant across the resonance region for λ_l. We label this value as $S_l^\star(\vec{r}, \hat{n})$.

According to Rybicki & Hummer (1978), the profile-weighted integral of the spe-

cific intensity cannot be defined on the large Sobolev scale (where it is an integral of a δ-function times a step function). Applying the expression for the solution to the RTE *inside* a resonance region on small scales, they obtain

$$\int_0^\infty d\lambda \Big\{ \phi_l(\lambda) I(\vec{r}, \hat{n}, \lambda) \Big\} = I_l^\star(\vec{r}, \hat{n}) \beta_l + S_l^\star(\vec{r}, \hat{n})(1 - \beta_l) \tag{5.6}$$

where $I_l^\star(\vec{r}, \hat{n}) = I_\infty(\vec{r}, \hat{n}, \lambda_l)$, the intensity arriving from infinity at the resonance point, and the quantity

$$\beta_l(\vec{r}) = \frac{1 - \exp(-\tau_l(\vec{r}))}{\tau_l(\vec{r})}. \tag{5.7}$$

Substituting Equation (5.6) into Equation (5.5), and using the equivalent two level atom (ETLA) source function in the Sobolev approximation, we obtain

$$\begin{aligned} 4\pi \vec{\nabla} \cdot \vec{H}(\vec{r}) &= \sum_{l=1}^{L} \bar{K}_l(\vec{r}) \beta_l(\vec{r}) \oint d\Omega \Big\{ S_l^\star(\vec{r}, \hat{n}) - I_l^\star(\vec{r}, \hat{n}) \Big\} \\ &= 4\pi \sum_{l=1}^{L} \bar{K}_l(\vec{r}) \beta_l(\vec{r}) \Big\{ S_l^\star(\vec{r}) - J_l^\star(\vec{r}) \Big\} \end{aligned} \tag{5.8}$$

In our parameterized work, we have assumed that the source function is that of pure resonance scattering (i.e., $S = J$). A more general assumption is that it may be written in the form of an *equivalent two level atom* source function, which carries a thermal contribution and a scattering contribution,

$$S_l^\star(\vec{r}) = (1 - \bar{\epsilon}_l(\vec{r})) J_l^\star(\vec{r}) + \bar{\epsilon}_l(\vec{r}) B_l^\star(T(\vec{r})) \tag{5.9}$$

where $B_l^\star(T(\vec{r}))$ is the Planck function evaluated at the line wavelength λ_l for the temperature T given at the point $\vec{r}$. The Sobolev thermalization parameter $\bar{\epsilon}_l(\vec{r})$ is

given in terms of $\beta_l(\vec{r})$ and the usual ETLA thermalization parameter ϵ,

$$\bar{\epsilon}_l(\vec{r}) = \frac{\epsilon}{\epsilon + (1-\epsilon)\beta_l(\vec{r})} \tag{5.10}$$

The ϵ term characterizes the ratio of absorptive extinction to total (absorptive plus scattering) extinction.

Substituting the source function given by Equation (5.9) into Equation (5.8) and replacing the total integrating opacity with the optical depth, we obtain

$$\vec{\nabla} \cdot \vec{H}(\vec{r}) = \sum_{l=1}^{L} \tau_l(\vec{r}) \lambda_l \beta_l(\vec{r}) \bar{\epsilon}_l(\vec{r}) \Big\{ J_l^*(\vec{r}) - B_l(T(\vec{r})) \Big\} \tag{5.11}$$

The condition of radiative equilibrium states that all energy flow is in the form of radiation, and that there are no net sources or sinks of energy at the point $\vec{r}$. In that case, the flux divergence must vanish, and we are left with a condition on the radiation field and optical depth for the condition of RE to be satisfied:

$$0 = \sum_{l=1}^{L} \varpi_l(\vec{r}) \Big\{ J_l^*(\vec{r}) - B_l(T(\vec{r})) \Big\}. \tag{5.12}$$

where the weight $\varpi_l(\vec{r})$ is given by

$$\varpi_l(\vec{r}) \equiv \tau_l(\vec{r}) \lambda_l \beta_l(\vec{r}) \bar{\epsilon}_l(\vec{r}) \tag{5.13}$$

5.2 Application

In general, we cannot know *a priori* what the correct temperature structure $T(\vec{r})$ is that will produce the right opacity distribution and radiation field to satisfy radiative

equilibrium. There are two approaches to this problem. The first is to directly incorporate the condition of radiative equilibrium into the transfer problem. The second, less conceptually difficult method is to approach the correct temperature structure proceeding from an initial guess using temperature corrections, such as Λ-iteration.

The historic problems with Λ-iteration are well-known. In principle, the scheme works, but it works very slowly. The problem is that each iteration permits adjustments of the radiation field to propagate only about one mean free path. This has very dubious consequences for conditions at depth, where $S = J = B$; there the corrections vanish, leading to pseudo-convergence or stabilization at the wrong temperature structure.

However, Lucy (1999a) pointed out a very interesting consequence of the EEP formulation of the MC method. Recall that in the EEP formulation, packet energy is conserved no matter what; absorption followed by re-emission may change the wavelength of the packet, but the total energy is constant. This constancy implies that the MC radiation field lacks divergence, so for a given opacity distribution the value of $J_l^\star(\vec{r})$ is correct (provided the number of packets is large). This means that adjustments to the opacity distribution on subsequent iterations propagate everywhere, not just one mean free path. We expect this to make the coupling of Λ-iteration with the EEP MC method work well to obtain RE temperature structures.

In practice, we begin with some temperature distribution as a guess. This is used to solve the LTE equation of state at all points throughout the envelope, which determines the ionization fractions and electron densities. These are used to compute the Sobolev optical depths, Sobolev thermalization parameters and emissivity tables everywhere. A MC realization is then performed to establish an estimate of the radiation field. This in turn is used to solve Equation (5.12) for a new temperature estimate. We then repeat this sequence of events for some number of iterations, until

the changes to the temperature structure (or better yet, mean intensities) become small. The procedure is spelled out diagrammatically in Equation (5.14).

$$\begin{array}{ccc} T(\vec{r}) & \xrightarrow{EOS(n,C,T)} & f(Z,I,\vec{r}), n_e(\vec{r}) \\ {\scriptstyle Rad\ Eq}\uparrow & & \downarrow{\scriptstyle LTE} \\ \bar{J}_l(\vec{r}) & \xleftarrow[Monte\ Carlo]{} & \tau_l(\vec{r}), \tau_e(\vec{r}), \varpi_l(\vec{r}) \end{array} \tag{5.14}$$

5.3 Continuous Opacity

Since we have some idea now of what the real distribution of the electron density is like, for the sake of consistency, we can include the effect of electron scattering into the transport. The optical depth due to electron scattering comes from just Thomson scattering.

$$\tau_e(s) = \int_0^s ds' \left\{ \sigma_T n_e(s') \right\}. \tag{5.15}$$

In practice, all the quantities (optical depths, number densities) are constant within a given cell, so the electron density does not vary along the path length of the packets within a given cell, $n_e(s) \equiv n_e$.

The only modification this introduces into the implementation is that in addition to possible line scatterings, packets may interact with electrons as well. But instead of interacting at isolated resonance points, packets scatter off electrons at a point where the accumulated optical depth equals $-\ln(\Re)$ where $\Re$ is a uniform random deviate between 0 and 1.

The inclusion of other wavelength-dependent continuum sources (bound-free, free-free) is also possible. Jeffery (1989) has described the use of discretized continuous opacity (DCO) to handle continuum opacity in the Sobolev approximation. Unlike electron scattering (which is pure coherent scattering), continuum processes are more like line processes in that they can thermalize packets and re-emit them at another

wavelength. However, at this point, we do not include continuous opacity; the general wavelength dependence increases the storage required for running a model in 3D.

5.4 Equivalent Two Level Atom

By including a thermal contribution to the source function, we have permitted the possibility that packets are destroyed on interaction and then re-emitted at another wavelength. In pure resonance scattering, this is not the case; such scattering is coherent.

In terms of the MC calculation, this means that we must, upon an absorption, determine a new wavelength for the cell to re-emit the packet in. This is obtained by inverting the following equation for λ

$$\Re = \Big(\int_0^{\lambda} d\lambda\ \chi(\vec{r},\lambda)\bar{\epsilon}(\vec{r},\lambda)B(\vec{r},\lambda)\Big) / \Big(\int_0^{\infty} d\lambda\ \chi(\vec{r},\lambda)\bar{\epsilon}(\vec{r},\lambda)B(\vec{r},\lambda)\Big), \qquad (5.16)$$

where again $\Re$ is a uniform random deviate between 0 and 1.

In practice, however, the form of $\chi(\vec{r},\lambda)$ is that dictated by the non-overlapping line assumption. The integrals then simply become sums over individual lines l. This means that in each cell, we tabulate the right hand side values as a function of λ_l and choose an entry using a roulette-wheel selection. That is, a line which dominates a large fraction of the total emissivity is more likely to re-emit than a weaker one.

5.5 1D Example - Mixed W7

To illustrate the convergence properties, we elect to simulate the W7 white dwarf deflagration model. Above 9000 km s^{-1}, we mix the composition so that it is uniform in relative abundances. The density of the envelope falls off with an exponential folding

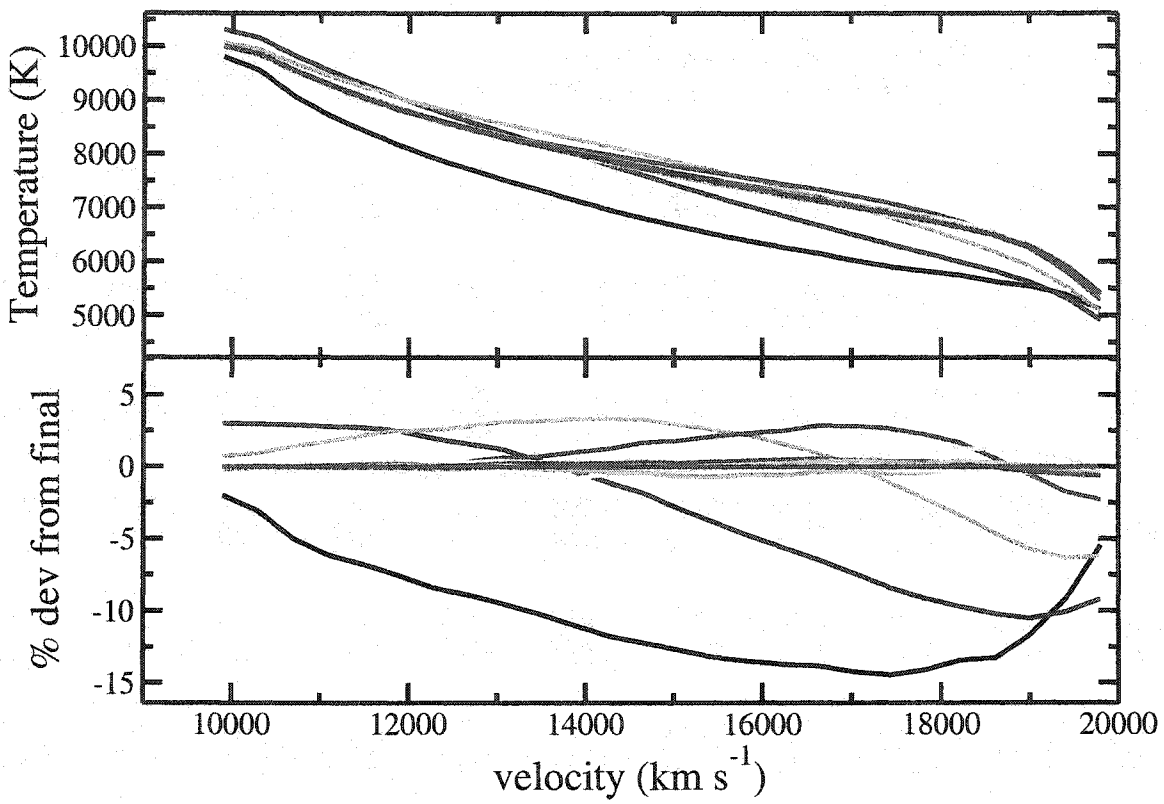

Figure 5.1: One zone mixed W7 temperature structures without e^-. The first four iterations (black, red, green and blue) show the most change. After those iterations, the temperature structure settles down.

velocity of 2500 km s^{-1}. The temperature structures (temperature as a function of velocity) from 10 iterations are shown in Figure 5.1. For the value of ϵ we choose 0.1.

The initial temperature guess was an isothermal 9000 K, and the photospheric temperature was held fixed at 10000 K. In principle, the energy scale should be set at a target bolometric luminosity, but for simplicity we elected to use the photospheric luminosity instead. The convergence properties are quite remarkable. In four iterations the temperature stops changing more than 1%.

Spectra corresponding to certain selected iterations are shown in Figure 5.2. The behavior of the spectra echo that of the temperature structure; they stop changing after the first few iterations.

An example set of spectra with electron scattering included is provided in Figure

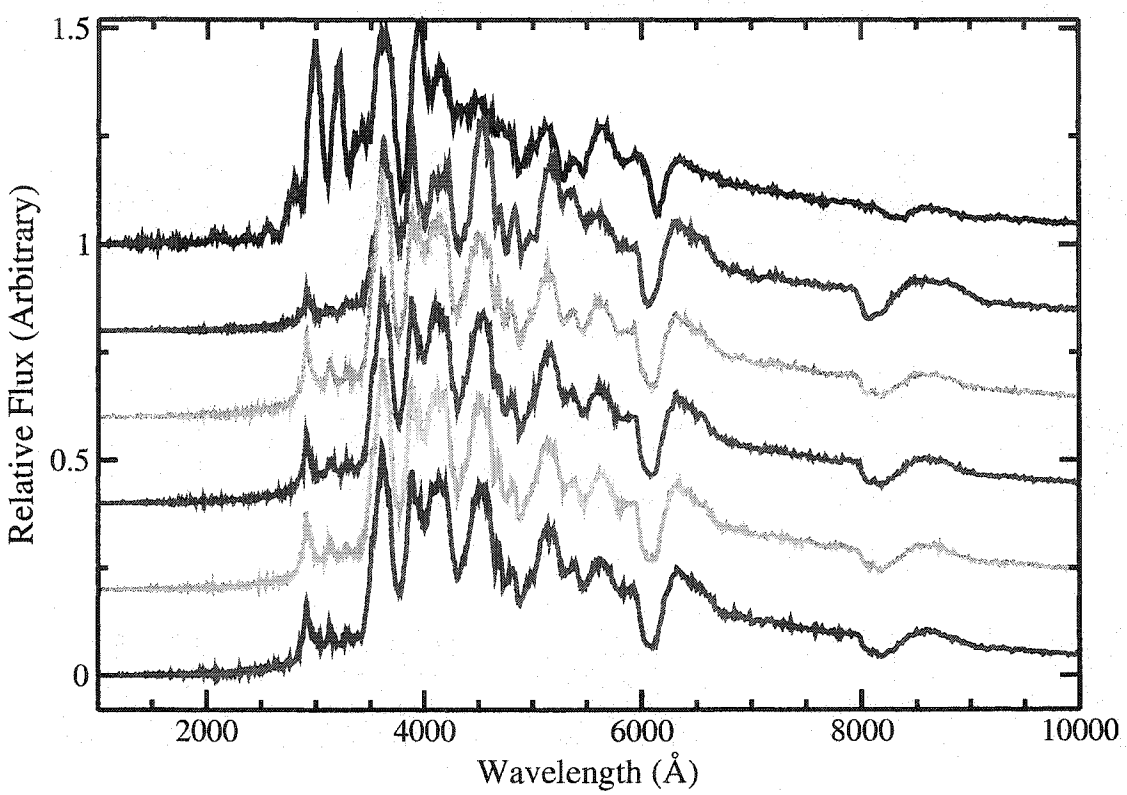

Figure 5.2: One zone mixed W7 spectra without e^-. Iterations 1, 3, 5, 7, 9 and 10 are shown (top to bottom).

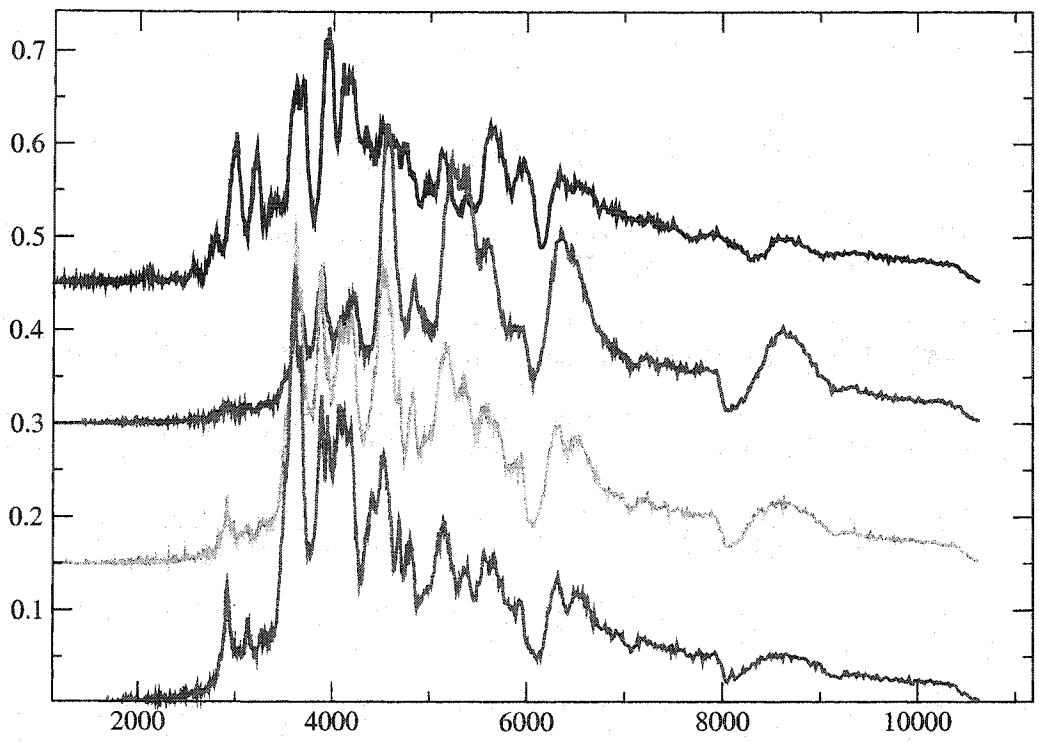

Figure 5.3: One zone mixed W7 spectra with e^-. Iterations 1, 2, 3, 4 are shown (top to bottom).

5.3. The photospheric velocity is reduced to 7000 km s^{-1} and the electron distribution is permitted to set up its own photosphere of sorts. The spectra look a little unusual, in part because the composition used below 9000 km s^{-1} is somewhat incorrect.

Computing the transport of models with electron scattering involved takes more time. The convergence properties are similar to the case without electron scattering included.

5.6 3D Example – W7 with HV Clump

The 1D models run in a matter of minutes, and are compact enough to be computed on a single computer. On the other hand, the requirement that we store optical depths, mean intensities and other quantities for about 500000 cells increases the memory requirements tremendously.

The computation of the optical depths for this many cells presents a serious problem. If 10^6 lines are loaded, computing optical depths will require of order 10^{11} exponentials be calculated, which is very slow. To combat this problem, we are implementing a hybrid OpenMP-MPI structure to parallelize opacity distribution across processors on multiple nodes. The memory requirement for very big models approaches 30 GB. So in order to compute some simple 3D models, for now we must place a limit on the (gf) value of lines we choose. This will make us miss some important lines, but we can at least start to compute some 3D models this way.

The 3D model we compute is a combination of the mixed W7 model computed in the previous section with a HV clump not unlike that used in the 3D HV fits of Ca II in SN 2000cx. In the same velocity range as in the case of SN 2000cx, we scale the density of W7 up by a factor of 100 and compute spectra for several lines of sight. Our goal here is just to see what changes occur as a function of line of sight. The results are in Figure 5.4.

The first spectrum is computed looking down through the clump toward the photosphere. The most notable features appearing include a HV Si II feature and some unusual features in the IR clearly originating in the HV ejecta (identifiable because of the shape of their profiles). The slightly peculiar shape of the spectrum is due to the fact that we cut back on the number of lines used to compute opacity distribution in a reasonable amount of time. Further parallelization will ameliorate this problem.

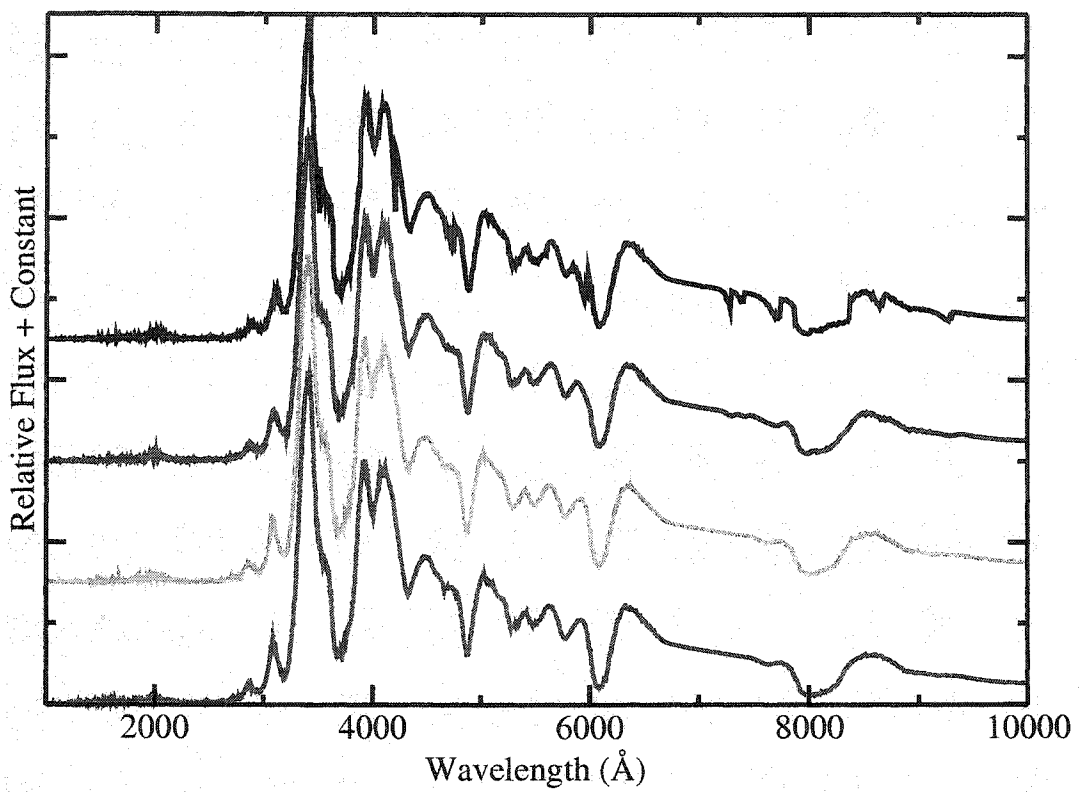

Figure 5.4: One zone mixed W7 spectra, with HV clump. From top to bottom, the formal spectra from 0, 30, 60 and 90 degrees with respect to the clump/photosphere axis are shown.

5.7 Summary and Conclusion

We have taken some very small steps away from purely parameterized models by engineering 3D radiative equilibrium SN atmospheres. At present, these 3D models are impeded by computational limitations. The immediate goal is to overcome these problems by parallelization, which is trivial for MC simulations. By including more line opacity and continuous opacity, we can construct more reliable radiative equilibrium models.

More long term goals include relaxing the assumption of LTE, and including NLTE effects such as branching. This will require an incremental approach, including NLTE treatments for individual ions one at a time.

Chapter 6

Summary and Conclusions

In this dissertation, we have described the development and application of techniques for spectrum synthesis of 3D SN models. Some of the techniques and tools developed are useful as pedagogical tools for thinking about SN line feature formation without relying on spherical symmetry (`tauBrute`). More sophisticated tools include the empirical analysis code `synBrute`. The first small steps toward self consistent modelling useful for testing theoretical explosion models are embodied in the `lteBrute` code. Hopefully, the future will provide opportunities to expand upon these tools to include more and more physics.

Directions for future work are divided mainly into applications and extensions of the work discussed here. Extensions include implementing polarized transport, some limited NLTE effects (at first), and a more realistic means of treating the inner regions of the ES model atmosphere. Indeed, the hope is to progressively relax the assumptions of the ES model and move towards a more accurate modelling code.

[1] **Polarization transport.** Deriving envelope structure from flux spectra is an ill-posed inverse problem. At best, flux spectra from a code like `Brute` can only constrain photospheric covering fractions through absorption features. These constraints

are important for hydrodynamical explosion modellers, but including polarized transfer into Brute will add a new dimension for reconstructing ejecta distributions in SNe. Though plots of theoretical and observed Stokes parameters Q and U will not fully solve the problem of ejecta structure, they complement results derived from flux spectra. If the goal is to constrain the importance of 3D geometry in any type of SN, Brute must include polarized transfer. This is done by propagating along with packets their Stokes vector components. During the line interactions, packets become depolarized (since the "stored" polarization state is destroyed through atomic collisions), but electron scatterings select a new Stokes vector. In principle, the inclusion of this effect is simple, but it does add overhead. In particular, these simulations require a high degree of spatial resolution in order to replicate analytical results.

[2] NLTE effects. Assuming LTE in Brute for computing SN Ia spectra is not as problematic as it is for other types of SNe. In order to more confidently model core collapse events (which also generally exhibit more polarization than do SNe Ia), NLTE effects will be included into the code. This will mean a full implementation of packet branching and the solution to the rate equations on a large 3D grid. The rewards include the ability to produce more self-consistent models of core collapse SNe, and close in on the answer to the mystery of whether or not these events are related at all to GRBs. In principle, the NLTE branching scheme requires a rate matrix for every grid point. Probably the best approach is to begin by including the most important NLTE species while leaving others in LTE. This technique has worked well for PHOENIX, and is especially suitable in this case since the memory requirements for NLTE will be much higher in 3D than in 1D.

[3] Replacement of the lower boundary. The currently implemented "lower boundary" in a Brute model atmosphere is an artificial, sharp, Lambert radiator surface. This implementation of the photosphere is acceptable for purposes of empirical spectrum analysis and line identification, but insufficient for fully detailed synthetic

spectra. Instead, a γ-ray-deposition function or γ-ray transport (and more sophisticated continuum processes) in the inner reaches of model SNe would more closely resemble that in the physical situation.

All of the improvements discussed to make `Brute` into a detailed SN spectrum synthesis code require *significant* and *superior* computational methods and facilities. The `tauBrute` and `synBrute` versions of the code currently run on a desktop PC or workstation class machine. More complicated parameterized models require that `synBrute` take advantage of parallelization to run in a reasonable amount of time. For a full temperature structure calculation with `lteBrute`, the memory requirements are significantly higher. A full opacity grid for 3D SN Ia model requires about 30 GB of memory in a grid of 500000 cube cells.

Fortunately, the MC approach makes the parallelization of the code trivial, and `synBrute` and `lteBrute` currently incorporate OpenMP directives to improve small-loop performance. On a larger scale, both codes use the hybrid OpenMP-MPI paradigm to both improve packet statistics and to parallelize opacity deployment on a distributed network of shared-memory multiprocessors. But larger-memory nodes are often difficult to come by, so running the code on a cheaper network like a Beowulf cluster increases communication demand in the face of domain decomposition. But in general, as computer technology and techniques improve over the next few years, more powerful computers will allow us to compute more powerful models.

There are three major parts to solving the puzzle of SN geometry. On one hand there are the observations, the quality of which is destined to improve as new telescopes are built and SN surveys take shape. On the other are the theoretical explosion models, which attempt to unify the fields of hydrodynamics, nuclear physics, and even general relativity. The point of contact between these two models is spectrum modelling. When these three efforts are aligned, there is hope that we may understand the root causes and dynamics of SN explosions even better than we do now.

Bibliography

Anderson, M., Jones, T., Rudnick, L., Tregillis, I., & Kang, H. 1994, ApJ, 421, L31

Auer, L. 2003, in Stellar Atmosphere Modeling, Proceedings of an International Workshop held in Tübingen, Germany, 8-12 April 2002, 3

Baron, E., Branch, D., Hauschildt, P. H., Filippenko, A. V., Kirshner, R. P., et al. 2000, ApJ, 545, 444

Branch, D. 2001, PASP, 113, 169

Branch, D., Benetti, S., Kasen, D., Baron, E., et al. 2002, ApJ, 566, 1005

Branch, D., Doggett, J., Nomoto, K., & Thielemann, F.-K. 1985, ApJ, 294, 619

Branch, D., Fisher, A., & Nugent, P. 1993, AJ, 106, 2383

Burrows, A., Hayes, J., & Fryxell, B. 1995, ApJ, 450, 830

Castor, J. 1970, MNRAS, 149, 11

Chevalier, R., & Klein, R. 1978, ApJ, 219, 994

Collins, G. 1989, The Fundamentals of Stellar Astrophysics (New York: W. H. Freeman)

Cordes, J., & Chernoff, D. 1998, ApJ, 505, 315

Decourchelle, A., et al. 2001, A&A, 365, L218

Elmhamdi, A., et al. 2003, MNRAS, 338, 939

Fassia, A., et al. 1998, MNRAS, 299, 150

Fesen, R., & Gunderson, K. 1996, ApJ, 470, 967

Fisher, A. 2000, PhD thesis, University of Oklahoma

Gamezo, V., Khokhlov, A., Oran, E., Chtchelkanova, A., & Rosenberg, R. 2003, Science, 299, 77

Hachisu, I., Kato, M., Nomoto, K., & Umeda, H. 1999, ApJ, 519, 314

Hamuy, M., et al. 2001, ApJ, 558, 615

Hatano, K., Branch, D., Fisher, A., Baron, E., & Filippenko, A. V. 1999a, ApJ, 525, 881

Hatano, K., Branch, D., Fisher, A., Millard, J., & Baron, E. 1999b, ApJS, 121, 233

Hauschildt, P., & Baron, E. 1999, J. Comp. Applied Math., 109, 41

Houck, J., & Fransson, C. 1996, ApJ, 456, 811

Howell, D., Höflich, P., Wang, L., & Wheeler, J. 2001, ApJ, 556, 302

Hwang, U., Holt, S., & Petre, R. 2000, ApJ, 537, L119

Jeffery, D. 1989, ApJS, 71, 951

—. 1993, ApJ, 415, 734

Jeffery, D., & Branch, D. 1990, in Supernovae, Jerusalem Winter School for Theoretical Physics, 149

Kasen, D., et al. 2003, ApJ, submitted

Khokhlov, A. 2000, astro-ph/0008463

Kifonidis, K., Plewa, T., Janka, H.-T., & Müller, E. 2000, ApJ, 531, L123

—. 2003, A&A, submitted

Kurucz, R. 1993, CD-ROM 1, Atomic Data for Opacity Calculations (Cambridge: Smithsonian Astrophysical Observatory)

Leonard, D., Filippenko, A., Barth, A., & Matheson, T. 2000, ApJ, 536, 239

Leonard, D., et al. 2002, PASP, 114, 35

Li, H., & McCray, R. 1992, ApJ, 387, 309

Li, H., McCray, R., & Sunyaev, R. 1993, ApJ, 419, 824

Li, W., Filippenko, A., Gates, E., Chornock, R., Gal-Yam, A., Ofek, E., Leonard, D., Modjaz, M., Rich, R., Riess, A., & Treffers, R. 2001a, PASP, 113, 1178

Li, W., Filippenko, A. V., Treffers, R., Riess, A., Hu, J., & Qiu, Y. 2001b, ApJ, 546, 734

Lucy, L. 1999a, A&A, 344, 282

—. 1999b, A&A, 345, 211

—. 2002, A&A, 384, 725

MacFadyen, A., Woosley, S., & Heger, A. 2001, ApJ, 550, 410

Marietta, E., Burrows, A., & Fryxell, B. 2000, ApJS, 128, 615

Mazzali, P., & Lucy, L. 1993, A&A, 279, 447

Mihalas, D. 1978, Stellar Atmospheres (San Francisco: W. H. Freeman)

Millard, J., Branch, D., Baron, E., Hatano, K., et al. 1999, ApJ, 527, 746

Mitchell, R., et al. 2001, ApJ, 556, 979

Nomoto, K., Thielemann, F.-K., & Yokoi, K. 1984, ApJ, 286, 644

Nugent, P., Baron, E., Hauschildt, P., & Branch, D. 1995, ApJ, 441, L33

Pavlakis, K., & Kylafis, N. 1996, ApJ, 467, 292

Perlmutter, S., et al. 1999, ApJ, 517, 565

Phillips, M. 1993, ApJL, 413, 105

Phillips, M., & Heathcote, S. 1989, PASP, 101, 137

Reinecke, M., Hillebrandt, W., & Niemeyer, J. 2002, A&A, 391, 1167

Richardson, D., Branch, D., Casebeer, D., Millard, J., Thomas, R. C., & Baron, E. 2002, AJ, 123, 745

Riess, A., et al. 1998, AJ, 116, 1009

Rybicki, G., & Hummer, D. 1978, ApJ, 219, 654

Shapiro, P., & Sutherland, P. 1982, ApJ, 263, 902

Sobolev, V. V. 1947, Moving Envelopes of Stars (Leningrad: Leningrad State University)

Spyromilio, J. 1991, MNRAS, 253, 25P

—. 1994, MNRAS, 266, L61

Spyromilio, J., & Pinto, P. 1991, in Supernova 1987A and Other Supernovae, ESO/EIPC Workshop on Supernovae, ed. I. Danziger & K. Kjär, 423

Stanek, K., Matheson, T., Garnavich, P., et al. 2003, astro-ph/0304173

Starrfield, S. 2003, in From Twilight to Highlight: The Physics of Supernovae. Proceedings of the ESO/MPA/MPE Workshop held in Garching, Germany, 29-31 July 2002, p. 128., 128

Thomas, R., Branch, D., Baron, E., Li, W., & Filippenko, A. 2003, ApJ, submitted

Tsunemi, H., Miyata, E., & Aschenbach, B. 1999, PASJ, 51, 711

Utrobin, V., Chugai, N., & Andronova, A. 1995, A&A, 295, 129

Wang, L., Howell, D., Höflich, P., & Wheeler, J. 2001, ApJ, 550, 1030

Wang, L., Wheeler, J., & Höflich, P. 1997, ApJ, 476, L27

Wang, L., et al. 2003, ApJ, accepted

Wheeler, J. 1990, in Supernovae, Jerusalem Winter School for Theoretical Physics, 1

Wheeler, J. 2000, in Cosmic Explosions, ed. S. Holt & W. Zhang (New York: AIP), 445

Appendix A

tauBrute

These Appendices are included primarily as a programmers' reference, and also to give some flavor of the way that the codes designed work. For the ordinary reader, the most useful part will be the program flowcharts at the beginning. For other programmers, the list of interfaces is included for reference.

Included with each interface is a brief comment directly from the code. In some cases these comments are more descriptive than others. In cases where the usage and meaning is self-evident, commentary is kept to a minimum.

The `tauBrute` code is a simple code for computing line profiles for experimentation and exploration. Arbitrary 3D Sobolev optical depth templates are supplied for fake lines of arbitrary wavelength. Either a single scattering or multiple scattering source function may be used, but in either case pure resonance scattering ($S = J$) is assumed.

A descriptive flowchart describing `tauBrute` appears in Figure A.1.

A.1 CellClass

A.1.1 Cell_new

Constructor. Sets things set only once and unsets everything else.

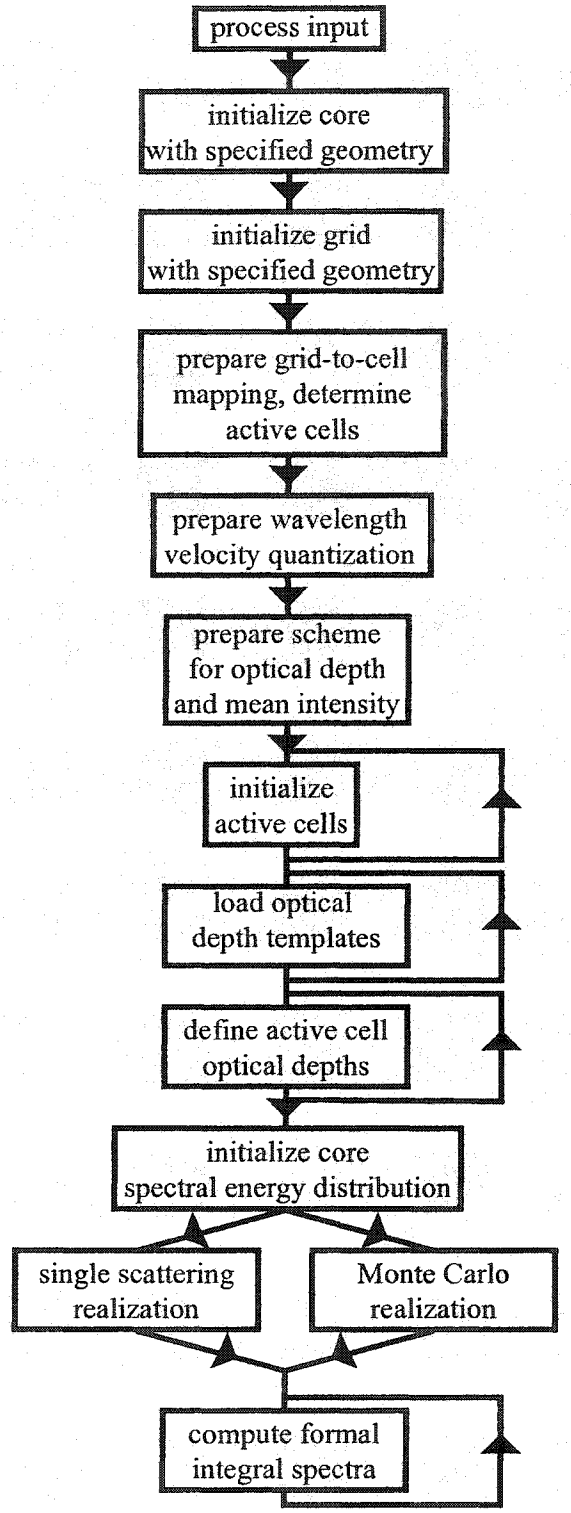

Figure A.1: Flowchart for the `tauBrute` code.

```
subroutine Cell_new( self, icel, iabu, avol, nden )
---------------------------------------------------
 type( CellType ), intent( in out ) :: self
 integer         , intent( in     ) :: icel, iabu
 real( wp )      , intent( in     ) :: avol, nden
```

A.1.2 Cell_copy

Copy constructor.

```
subroutine Cell_copy( self, orig )
----------------------------------
 type( CellType ), intent( in out ) :: self
 type( CellType ), intent( in     ) :: orig
```

A.1.3 Cell_die

Unsets the cell values and deallocates tables.

```
subroutine Cell_die( self )
---------------------------
 type( CellType ), intent( in out ) :: self
```

A.1.4 nextTemp

Sets the cell temperature. If one is provided, then that is the one set. If one is not provided, and the energy absorption rate is not zero, then we use a radiative equilibrium calculation to calculate it. In either case, the temperature dependent quantities are all unset.

```
subroutine nextTemp( self, temp )
---------------------------------
 type( CellType ), intent( in out )           :: self
 real( wp )      , intent( in     ), optional :: temp
```

A.1.5 defCell

Defines the transfer properties of the cell, including the electron distribution parameters. The electron distribution parameters are mandatory, so even if the scheme dictates that they will not be used they must be set (to zero, say). The other quantities are wavelength dependent. If there are none of them, they are then not supplied.

```
subroutine defCell( self, eden, taue, nwln, iwln, xwln )
-------------------------------------------------------
 type( CellType ), intent( in out )       :: self
 real( wp )      , intent( in     )       :: eden, taue
 integer         , intent( in     )       :: nwln
 integer         , intent( in ), optional :: iwln( 1 : nwln )
 real( wp )      , intent( in ), optional :: xwln( 1 : sch_ncol, &
                                                 & 1 : nwln      )
```

A.1.6 undefCell

Called to undefine the wavelength table parameters of a cell, or it is called if there are going to be no wavelength-dependent parameters set.

```
subroutine undefCell( self )
----------------------------
 type( CellType ), intent( in out ) :: self
```

A.1.7 showCellShort

Outputs a shrot description of cell contents.

```
subroutine showCellShort( self, unio )
--------------------------------------
 type( CellType ), intent( in )           :: self
 integer         , intent( in ), optional :: unio
```

A.1.8 showCellLong

Outputs a long description of cell contents.

```
subroutine showCellLong( self, unio )
-------------------------------------
 type( CellType ), intent( in )           :: self
 integer         , intent( in ), optional :: unio
```

A.1.9 localIndex

Returns the local index of a requested lambda if it is active. Otherwise, returns zero.

```
pure integer function localIndex( self, iwln )
----------------------------------------------
 type( CellType ), intent( in ) :: self
 integer         , intent( in ) :: iwln
```

A.1.10 thermalize

Pick a new lambda from the eta vector. Returns the index into the envelope wavelength array.

```
pure integer function thermalize( self, etab )
------------------------------------------------
 type( CellType ), intent( in ) :: self
 real( wp )      , intent( in ) :: etab
```

A.2 CharClass

A.2.1 Char_new

Initializes quantites that hold for all frames. If the characteristic is not going to be used because it is outside vmax, then nothing will be set.

```
subroutine Char_new( self, vban, vmax, pobs )
-----------------------------------------------
 type( CharType ), intent( in out ) :: self
 real( wp )      , intent( in     ) :: vban, vmax, pobs( 2 )
```

A.2.2 Char_copy

Copy constructor.

```
subroutine Char_copy( self, orig )
-----------------------------------
 type( CharType ), intent( in out ) :: self
 type( CharType ), intent( in     ) :: orig
```

A.2.3 Char_die

Destructor.

```
subroutine Char_die( self )
----------------------------
 type( CharType ), intent( in out ) :: self
```

A.2.4 showChar

Display a report on this characteristic.

```
subroutine showChar( self, unio )
---------------------------------
 type( CharType ), intent( in )           :: self
 integer         , intent( in ), optional :: unio
```

A.2.5 setObserver_phth

Takes an observer direction (phi and theta) and sets all the observer- dependent variables.

```
subroutine setObserver_phth( self, ophi, otht, xcor, xgrd )
-----------------------------------------------------------
 type( CharType ), intent( in out ) :: self
 real( wp )      , intent( in     ) :: ophi, otht
 type( CoreType ), intent( in     ) :: xcor
 type( GridType ), intent( in     ) :: xgrd
```

A.2.6 setObserver_nhat

Takes an observer direction (nhat) and sets up all the observer-dependent variables.

```
subroutine setObserver_nhat( self, nhat, xcor, xgrd )
-----------------------------------------------------
 type( CharType ), intent( in out ) :: self
 real( wp )      , intent( in     ) :: nhat( 3 )
 type( CoreType ), intent( in     ) :: xcor
 type( GridType ), intent( in     ) :: xgrd
```

A.3 CoreClass

A.3.1 Core_new

Constructor.

```
subroutine Core_new( self, rrad, zrad )
---------------------------------------
 type( CoreType ), intent( in out ) :: self
 real( wp )      , intent( in     ) :: rrad, zrad
```

A.3.2 Core_copy

Copy constructor.

```
subroutine Core_copy( self, orig )
----------------------------------
 type( CoreType ), intent( in out ) :: self
 type( CoreType ), intent( in     ) :: orig
```

A.3.3 Core_die

Destructor.

```
subroutine Core_die( self )
---------------------------
 type( CoreType ), intent( in out ) :: self
```

A.3.4 showCore

Puts a description the core object to a file unit. If the file unit is not present, then STDOUT is assumed.

```
subroutine showCore( self, unio )
---------------------------------
 type( CoreType ), intent( in out )           :: self
 integer         , intent( in     ), optional :: unio
```

A.3.5 point

Returns the status of a given point with respect to the core surface

```
pure integer function point( self, vpta )
-----------------------------------------
 type( CoreType ), intent( in ) :: self
 real( wp )      , intent( in ) :: vpta( 3 )
```

A.3.6 beam

Returns the status of a beam through a given point in a given direction with respect to the core surface.

```
pure integer function beam( self, vpta, mhat )
----------------------------------------------
 type( CoreType ), intent( in ) :: self
 real( wp )      , intent( in ) :: vpta( 3 )
 real( wp )      , intent( in ) :: mhat( 3 )
```

A.3.7 ray

Returns the status of a ray from a given point in a given direction with respect to the core surface.

```
pure integer function ray( self, vpta, mhat )
----------------------------------------------
 type( CoreType ), intent( in ) :: self
 real( wp )      , intent( in ) :: vpta( 3 )
 real( wp )      , intent( in ) :: mhat( 3 )
```

A.3.8 segment

Returns the status of a segment from a given point to another with respect to the core surface.

```
pure integer function segment( self, vpta, vptb )
-------------------------------------------------
 type( CoreType ), intent( in ) :: self
 real( wp )      , intent( in ) :: vpta( 3 )
 real( wp )      , intent( in ) :: vptb( 3 )
```

A.3.9 intPoints

Returns the value of the beam path points along the beam where the beam intersects the surface. If it doesn't intersect the core, you get back something stupid like -1, -1. If the ray only has one crossing with the core, you get -1 for one of the results, just throw it away.

```
pure function intPoints( self, vpta, mhat )
--------------------------------------------
 type( CoreType ), intent( in ) :: self
 real( wp )      , intent( in ) :: vpta( 3 )
 real( wp )      , intent( in ) :: mhat( 3 )
 real( wp )                     :: intPoints( 2 )
```

A.3.10 dilFactor

Returns the dilution factor of the core as seen from a given point.

```
real( wp ) function dilFactor( self, vpta )
-------------------------------------------
 type( CoreType ), intent( in ) :: self
 real( wp )      , intent( in ) :: vpta( 3 )
```

A.3.11 getLaunch

Returns a point on the surface of the core, and also returns an emission direction.

```
subroutine getLaunch( self, xdev, vpta, mhat )
----------------------------------------------
 type( CoreType ), intent( in     ) :: self
 real( wp )      , intent( in     ) :: xdev( 4 )
 real( wp )      , intent(    out ) :: vpta( 3 )
 real( wp )      , intent(    out ) :: mhat( 3 )
```

A.4 GridClass

A.4.1 Grid_new

Assigns determines gridpoint neighborhood volumes, and decides which ones are active and which are not.

```
subroutine Grid_new( self, vmax, ngpt, npts, xcor )
---------------------------------------------------
 type( GridType ), intent( in out ) :: self
 real( wp )      , intent( in     ) :: vmax
 integer         , intent( in     ) :: ngpt, npts
 type( CoreType ), intent( in     ) :: xcor
```

A.4.2 Grid_copy

Copy constructor.

```
subroutine Grid_copy( self, orig )
----------------------------------
 type( GridType ), intent( in out ) :: self
 type( GridType ), intent( in     ) :: orig
```

A.4.3 Grid_die

Destructor. Erases everything in the grid.

```
subroutine Grid_die( self )
---------------------------
 type( GridType ), intent( in out ) :: self
```

A.4.4 setCellMap

Prepares a mapping from the gridpoints to the cells.

```
subroutine setCellMap( self, ndim )
-----------------------------------
 type( GridType ), intent( in out ) :: self
 integer         , intent( in     ) :: ndim
```

A.4.5 unsetCellMap

Uninitializes the cell map.

```
subroutine unsetCellMap( self )
-------------------------------
 type( GridType ), intent( in out ) :: self
```

A.4.6 showGrid

Displays a report on the grid.

```
subroutine showGrid( self, unio )
---------------------------------
 type( GridType ), intent( in out )           :: self
 integer         , intent( in     ), optional :: unio
```

A.4.7 activeVolume_cmps3

Returns the total active volume in the grid for a given cell index in units of cmps**3

```
pure real( wp ) function activeVolume_cmps3( self, icel, tday )
---------------------------------------------------------------
 type( GridType ), intent( in ) :: self
 integer         , intent( in ) :: icel
 real( wp )      , intent( in ) :: tday
```

A.4.8 activeVolume_kmps3

Returns the total active volume in the grid for a given cell index in units of kmps**3.

```
pure real( wp ) function activeVolume_kmps3( self, icel )
---------------------------------------------------------
 type( GridType ), intent( in ) :: self
 integer         , intent( in ) :: icel
```

A.5 Lambda

A.5.1 setLambdas_range

Given a range of wavelengths and a band size, sets up the master lambda table. The velocity band width is in kmps.

```
subroutine setLambdas_range( wclo, wchi, vban )
-----------------------------------------------
 real( wp ), intent( in ) :: wclo, wchi, vban
```

A.5.2 setLambdas_array

Given a list of sorted wavelengths, forms a master lambda table.

```
subroutine setLambdas_array( nwln, wlen )
-----------------------------------------
 integer   , intent( in ) :: nwln
 real( wp ), intent( in ) :: wlen( 1 : nwln )
```

A.5.3 unsetLambdas

Releases information from the lambda list.

```
subroutine unsetLambdas()
-------------------------
```

A.5.4 showLambdasShort

Output of a summary of the lambdas to some file handle.

```
subroutine showLambdasShort( unio )
-----------------------------------
 integer, intent( in ), optional :: unio
```

A.5.5 showLambdasMedium

Output of the lambda list to some file handle.

```
subroutine showLambdasMedium( unio )
------------------------------------
 integer, intent( in ), optional :: unio
```

A.5.6 showLambdasLong

Output of the lambda list to some file handle.

```
subroutine showLambdasLong( unio )
----------------------------------
 integer, intent( in ), optional :: unio
```

A.5.7 linkLambdas_array

Given a list of wavelengths, links up the entries in the lambda list.

```
subroutine linkLambdas_array( nwln, wlen )
------------------------------------------
 integer   , intent( in ) :: nwln
 real( wp ), intent( in ) :: wlen( 1 : nwln )
```

A.5.8 linkLambdas_umask

Given a usage mask, links up the entries in the lambda list.

```
subroutine linkLambdas_umask( nwln, used )
------------------------------------------
 integer, intent( in ) :: nwln
 logical, intent( in ) :: used( 1 : nwln )
```

A.5.9 showLambdasLinked

Output of all the active lambdas to some file unit.

```
subroutine showLambdasLinked( unio )
------------------------------------
 integer, intent( in ), optional :: unio
```

A.5.10 getLambdaIndex

The index of a lambda such that the specified wavelength is between the index and less than or equal to the next one.

```
pure integer function getLambdaIndex( wlen )
---------------------------------------------
 real( wp ), intent( in ) :: wlen
```

A.5.11 getLambdaLinkedIndex

Returns the index of a lambda such that the specified wavelength is between the index and less than or equal to the next one. But it doesn't return the absolute index, rather it returns its position in the list of linked lambdas. If the wavelength is not in a linked lambda, zero is returned.

```
pure integer function getLambdaLinkedIndex( wlen )
------------------------------------------------
 real( wp ), intent( in ) :: wlen
```

A.6 RandomClass

A.6.1 Random_new

Constructor.

```
subroutine Random_new( self, seed )
-----------------------------------
 type( RandomType ), intent( in out ) :: self
 integer           , intent( in     ) :: seed
```

A.6.2 Random_copy

Copy constructor.

```
subroutine Random_copy( self, orig )
------------------------------------
 type( RandomType ), intent( in out ) :: self
 type( RandomType ), intent( in     ) :: orig
```

A.6.3 Random_die

Destructor, resets the random number generator to the default.

```
subroutine Random_die( self )
-----------------------------
 type( RandomType ), intent( in out ) :: self
```

A.6.4 unifDev_sngl

Select from uniform distribution between 0 and 1.

```
real( wp ) function unifDev_sngl( self )
----------------------------------------
 type( RandomType ), intent( in out ) :: self
```

A.6.5 unifDev_mult

Select from uniform distribution between 0 and 1.

```
function unifDev_mult( self, ndev )
-----------------------------------
 type( RandomType ), intent( in out ) :: self
 integer           , intent( in     ) :: ndev
 real( wp )                            :: unifDev_mult( 1 : ndev )
```

A.6.6 expoDev

Return an exponential distributed, positive random deviate of unit mean.

```
real( wp ) function expoDev( self )
-----------------------------------
 type( RandomType ), intent( in out ) :: self
```

A.7 Scheme

A.7.1 setScheme

Depending on what the user wants, we decide which columns are going to be used and we set up the column pointers. The TAU column is always used no matter what.

```
subroutine setScheme( elec, radq, etla, fint )
----------------------------------------------
 logical, intent( in ) :: elec, radq, etla, fint
```

A.7.2 unsetScheme

Deletes the current scheme settings.

```
subroutine unsetScheme()
------------------------
```

A.7.3 showScheme

Description of what the scheme looks like.

```
subroutine showScheme( unio )
-----------------------------
 integer, intent( in ), optional :: unio
```

A.8 SedClass

A.8.1 Sed_new

Provides a constructor for SED.

```
subroutine Sed_new( self, ised, nbin, wllo, wlhi, auxa )
-------------------------------------------------------
 type( SedType ), intent( in out ) :: self
 integer        , intent( in     ) :: ised, nbin
 real( wp )     , intent( in     ) :: wllo, wlhi, auxa
```

A.8.2 Sed_copy

Copy constructor.

```
subroutine Sed_copy( self, orig )
---------------------------------
 type( SedType ), intent( in out ) :: self
 type( SedType ), intent( in     ) :: orig
```

A.8.3 Sed_die

Destructor.

```
subroutine Sed_die( self )
--------------------------
 type( SedType ), intent( in out ) :: self
```

A.8.4 showSed

Output the SED information nicely.

```
subroutine showSed( self, unio )
--------------------------------
 type( SedType ), intent( in out )           :: self
 integer        , intent( in     ), optional :: unio
```

A.8.5 pickFromSed

Chooses a wavelength from the SED distribution given a bin and number between 0 and 1.

```
subroutine pickFromSed( self, ibin, xdev, wlen )
------------------------------------------------
 type( SedType ), intent( in     ) :: self
 integer        , intent( in     ) :: ibin
 real( wp )     , intent( in     ) :: xdev
 real( wp )     , intent(    out ) :: wlen
```

A.9 Spectrum

A.9.1 setSpectrum

Sets up the characteristic beams and quantities in them which are independent of observer.

```
subroutine setSpectrum( xgrd, ncha, vban )
------------------------------------------
 type( GridType ), intent( in ) :: xgrd
 integer         , intent( in ) :: ncha
 real( wp )      , intent( in ) :: vban
```

A.9.2 unsetSpectrum

Deletes the characteristic beam information.

```
subroutine unsetSpectrum()
--------------------------
```

A.9.3 calcSpectrum

Calculates the spectrum.

```
subroutine calcSpectrum( xcor, xgrd, xsed, xcel, xtht, xphi, nlam, &
                       & slam, spec                                 )
-------------------------------------------------------------------
 type( CoreType ), intent( in     ) :: xcor
 type( GridType ), intent( in     ) :: xgrd
 type( SedType  ), intent( in     ) :: xsed
 type( CellType ), intent( in     ) :: xcel( xgrd%lcel : xgrd%ucel )
 real( wp )      , intent( in     ) :: xtht, xphi
 integer         , intent( in     ) :: nlam
 integer         , intent( in     ) :: slam( 1 : nlam )
 real( wp )      , intent(    out ) :: spec( 1 : nlam )
```

A.10 TempClass

A.10.1 Temp_new_int

Construct a new candidate template using a big integer array.

```
subroutine Temp_new_int( self, imin, imax, jmin, jmax, kmin, kmax, &
                       & comm, ityp, idat                           )
-----------------------------------------------------------------------
 type( TempType )     , intent( in out ) :: self
 integer              , intent( in     ) :: imin, imax
 integer              , intent( in     ) :: jmin, jmax
 integer              , intent( in     ) :: kmin, kmax
 character( len = * ), intent( in     ) :: comm
 integer              , intent( in     ) :: ityp
 integer              , intent( in     ) :: idat( imin : imax, &
                                              & jmin : jmax, &
                                              & kmin : kmax  )
```

A.10.2 Temp_new_rwp

Construct a new candidate template using a big real working precision array.

```
subroutine Temp_new_rwp( self, imin, imax, jmin, jmax, kmin, kmax, &
                       & comm, ityp, xdat                           )
-----------------------------------------------------------------------
 type( TempType )     , intent( in out ) :: self
 integer              , intent( in     ) :: imin, imax
 integer              , intent( in     ) :: jmin, jmax
 integer              , intent( in     ) :: kmin, kmax
 character( len = * ), intent( in     ) :: comm
 integer              , intent( in     ) :: ityp
 real( wp )           , intent( in     ) :: idat( imin : imax, &
                                              & jmin : jmax, &
                                              & kmin : kmax  )
```

A.10.3 Temp_copy

Copy constructor.

```
subroutine Temp_copy( self, orig )
----------------------------------
 type( TempType ), intent( in out ) :: self
 type( TempType ), intent( in     ) :: orig
```

A.10.4 Temp_die

Destructor.

```
subroutine Temp_die( self )
---------------------------
 type( TempType ), intent( in out ) :: self
```

A.10.5 showTemp

Prints out the template header info and a little more.

```
subroutine showTemp( self, unio )
---------------------------------
 type( TempType ), intent( in )           :: self
 integer         , intent( in ), optional :: unio
```

A.10.6 cacheTemp

Puts a template on the disk.

```
subroutine cacheTemp( self, name )
----------------------------------
 type( TempType )    , intent( in ) :: self
 character( len = * ), intent( in ) :: name
```

A.10.7 fetchTemp

Makes a template, kind of a constructor, from a file.

```
subroutine fetchTemp( self, name )
----------------------------------
 type( TempType )    , intent( in out ) :: self
 character( len = * ), intent( in     ) :: name
```

A.11 Transport

A.11.1 ssTransport

Provides J's assuming single scattering transport.

```
subroutine ssTransport( xcor, xgrd, xsed, xcel )
-----------------------------------------------
 type( CoreType ), intent( in     ) :: xcor
 type( GridType ), intent( in     ) :: xgrd
 type( SedType  ), intent( in     ) :: xsed
 type( CellType ), intent( in out ) :: xcel( xgrd%lcel : xgrd%ucel )
```

A.11.2 msTransport

Computes the J's by Monte Carlo. Calculates a one-dimensional packet spectrum for debugging purposes. This method is not intended to be used for radiative equilibrium, and it is not intended to use electron scattering either.

```
subroutine msTransport( xcor, xgrd, xsed, xcel, npkt, seed, tday )
------------------------------------------------------------------
 type( CoreType ), intent( in     ) :: xcor
 type( GridType ), intent( in     ) :: xgrd
 type( SedType  ), intent( in     ) :: xsed
 type( CellType ), intent( in out ) :: xcel( xgrd%lcel : xgrd%ucel )
 integer         , intent( in     ) :: npkt, seed
 real( wp )      , intent( in     ) :: tday
```

Appendix B

synBrute

The `synBrute` code reuses most of the components described in Appendix A. Building on the `tauBrute` code to create a more useful direct analysis tool, we include the Kurucz (1993) line list and assume TE to populate the levels. The same reference optical depth scheme as in the 1D code `Synow` is used.

However, in place of radially symmetric functions to prescribe optical depth, template files like those used for `tauBrute` are used to define reference optical depth spatially for a list of ions.

Both single scattering and multiple scattering source functions are permitted. The source function is again taken to be that of pure resonance scattering. To improve packet statistics and speed up the process of opacity distribution, `synBrute` uses a combination OpenMP-MPI parallelization strategy for a distributed network of multiprocessors.

A descriptive flowchart describing `synBrute` appears in Figure B.1.

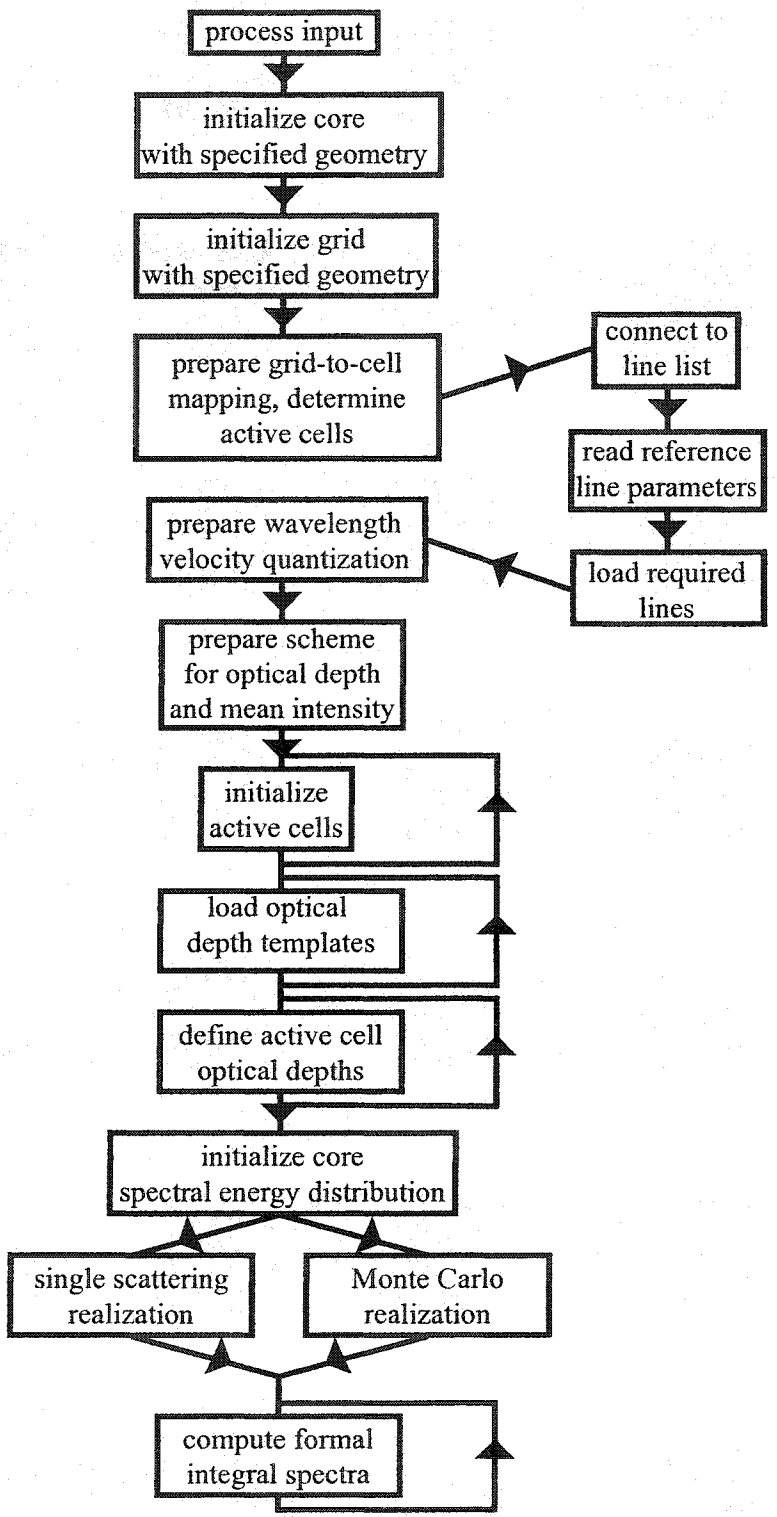

Figure B.1: Flowchart for the `synBrute` code.

B.1 Kurucz1993

B.1.1 hasKuruczPath

Returns true if the path to the Kurucz files has been set.

```
pure logical function hasKuruczPath()
--------------------------------------
```

B.1.2 setKuruczPath

Sets the path to the Kurucz files.

```
subroutine setKuruczPath( nuxi, path )
--------------------------------------
 logical                , intent( in ) :: nuxi
 character( len = * ), intent( in ) :: path
```

B.1.3 onDisk

Returns true if the corresponding Kurucz file is on the disk.

```
logical function onDisk( anum, aion )
--------------------------------------
 integer, intent( in ) :: anum, aion
```

B.1.4 connect

Connects to a Kurucz file if it is on disk and returns a Kurucz file handle.

```
subroutine connect( unio, anum, aion )
--------------------------------------
 integer, intent(    out ) :: unio
 integer, intent( in     ) :: anum, aion
```

B.1.5 disconnect

Disconnects a file handle if it is connected.

```
subroutine disconnect( unio )
-----------------------------
 integer, intent( in ) :: unio
```

B.1.6 isConnected

Returns true if the connection to the Kurucz file is open.

```
logical function isConnected( anum, aion )
------------------------------------------
 integer, intent( in ) :: anum, aion
```

B.1.7 hasLine_sngl

Returns true if there is a line with the given line index on the connected Kurucz handle.

```
logical function hasLine_sngl( unio, indx )
-------------------------------------------
 integer, intent( in ) :: unio, indx
```

B.1.8 hasLine_mult

Returns a mask where if there is a line with the given line index on the connected Kurucz handle, it is true.

```
function hasLine_mult( unio, nndx, indx )
-----------------------------------------
 integer, intent( in ) :: unio, nndx, indx( nndx )
 logical               :: hasLine_mult( nndx )
```

B.1.9 numLines_totl

Returns the number of lines on the connected Kurucz handle.

```
integer function numLines_totl( unio )
--------------------------------------
 integer, intent( in ) :: unio
```

B.1.10 numLines_lglo

Returns the number of lines on the connected Kurucz handle with log(gf) above the requested limit.

```
integer function numLines_lglo( unio, lglo )
--------------------------------------------
 integer   , intent( in ) :: unio
 real( wp ), intent( in ) :: lglo
```

B.1.11 numLines_wllm

Returns the number of lines on the connected Kurucz handle within the two wavelengths given.

```
integer function numLines_wllm( unio, wllo, wlhi )
--------------------------------------------------
 integer   , intent( in ) :: unio
 real( wp ), intent( in ) :: wllo, wlhi
```

B.1.12 numLines_lglo_wllm

Returns the number of liens on the connected Kurucz handle within the two wavelengths given above the limiting log(gf).

```
integer function numLines_lglo_wllm( unio, lglo, wllo, wlhi )
-------------------------------------------------------------
 integer   , intent( in ) :: unio
 real( wp ), intent( in ) :: lglo, wllo, wlhi
```

B.1.13 selectLine_sngl

Returns a single line.

```
subroutine selectLine_sngl( unio, indx, line )
----------------------------------------------
 integer   , intent( in     ) :: unio, indx
 real( wp ), intent(    out ) :: line( 3 )
```

B.1.14 selectLine_refl

Selects the ion's LTE reference line.

```
subroutine selectLine_refl( unio, line )
----------------------------------------
 integer   , intent( in     ) :: unio
 real( wp ), intent(    out ) :: line( 3 )
```

B.1.15 selectLine_mult

Returns multiple lines.

```
subroutine selectLine_mult( unio, nndx, indx, line )
----------------------------------------------------
 integer   , intent( in     ) :: unio, nndx, indx( nndx )
 real( wp ), intent(    out ) :: line( 3, nndx )
```

B.1.16 selectLine_totl

Returns all lines.

```
subroutine selectLine_totl( unio, nndx, line )
-----------------------------------------------
 integer   , intent( in     ) :: unio, nndx
 real( wp ), intent(    out ) :: line( 3, nndx )
```

B.1.17 selectLine_lglo

Returns all above a given log(gf). Assumes that the number nndx passed in is accurately determined before.

```
subroutine selectLine_lglo( unio, lglo, nndx, line )
-----------------------------------------------------
 integer   , intent( in     ) :: unio
 real( wp ), intent( in     ) :: lglo
 integer   , intent( in     ) :: nndx
 real( wp ), intent(    out ) :: line( 3, nndx )
```

B.1.18 selectLine_wllm

Returns all in a wavelength range. Assumes that the number nndx passed in is accurately determined before.

```
subroutine selectLine_wllm( unio, wllo, wlhi, nndx, line )
-----------------------------------------------------------
 integer   , intent( in     ) :: unio
 real( wp ), intent( in     ) :: wllo, wlhi
 integer   , intent( in     ) :: nndx
 real( wp ), intent(    out ) :: line( 3, nndx )
```

B.1.19 selectLine_lglo_wllm

Returns all in a wavelength range. Assumes that the number nndx passed in is accurately determined before.

```
subroutine selectLine_lglo_wllm( unio, lglo, wllo, wlhi, nndx, &
                                 & line                        )
-------------------------------------------------------------------
 integer   , intent( in     ) :: unio
 real( wp ), intent( in     ) :: lglo, wllo, wlhi
 integer   , intent( in     ) :: nndx
 real( wp ), intent(    out ) :: line( 3, nndx )
```

B.2 LineClass

B.2.1 lineCount

Returns the number of lines to allocate for the given log(gf), wavelength and ion restrictions.

```
integer function lineCount( lglo, wllo, wlhi, nspc, anum, aion )
-----------------------------------------------------------------
 real( wp ), intent( in ) :: lglo, wllo, wlhi
 integer   , intent( in ) :: nspc, anum( nspc ), aion( nspc )
```

B.2.2 Line_new

Loads a list of lines and sorts them.

```
subroutine Line_new( nlin, self, lglo, wllo, wlhi, nspc, anum, &
                   & aion                                      )
-----------------------------------------------------------------
 integer         , intent( in     ) :: nlin
 type( LineType ), intent( in out ) :: self( nlin )
 real( wp )      , intent( in     ) :: lglo, wllo, wlhi
 integer         , intent( in     ) :: nspc
 integer         , intent( in     ) :: anum( nspc ), aion( nspc )
```

B.2.3 refLine

Loads the reference line of an ion. The ispc is set outside.

```
subroutine refLine( self, anum, aion )
--------------------------------------
 type( LineType ), intent( in out ) :: self
 integer         , intent( in     ) :: anum, aion
```

B.2.4 locateLine

Returns the index of the line with wavelength just above that specified. 0 or n means the wavelength is out of range.

```
pure integer function locateLine( nlin, self, wlen )
-----------------------------------------------------
 integer         , intent( in ) :: nlin
 type( LineType ), intent( in ) :: self( nlin )
 real( wp )      , intent( in ) :: wlen
```

B.2.5 setBands

Makes lambda assignments for each line.

```
subroutine setBands( nlin, self, nlam, wllo, wlhi )
-------------------------------------------------
 integer          , intent( in     ) :: nlin
 type( LineType ), intent( in out ) :: self( nlin )
 integer          , intent( in     ) :: nlam
 real( wp )       , intent( in     ) :: wllo( nlam ), wlhi( nlam )
```

Appendix C

lteBrute

The most complicated code developed for this dissertation is `lteBrute`, which builds upon the parameterized direct analysis code `synBrute`. The major changes include a temperature iteration loop and inclusion of an LTE equation of state solver for determining ionization fractions. `lteBrute` builds upon the components described in the other Appendices, so we include here only those new interfaces needed for this particular code.

Instead of supplying optical depth templates as before, a composition map, a density map and initial temperature guess are provided. A radiative equilibrium procedure iterates on the temperature after each transport sweep. The source function is no longer restricted to that of pure resonance scattering; we permit an ETLA source function with a prescribed thermalization parameter that holds for the entire envelope.

A descriptive flowchart describing `lteBrute` appears in Figure C.1.

C.1 AtomData

C.1.1 ionStageLabel

Returns a Roman numeral ion stage label.

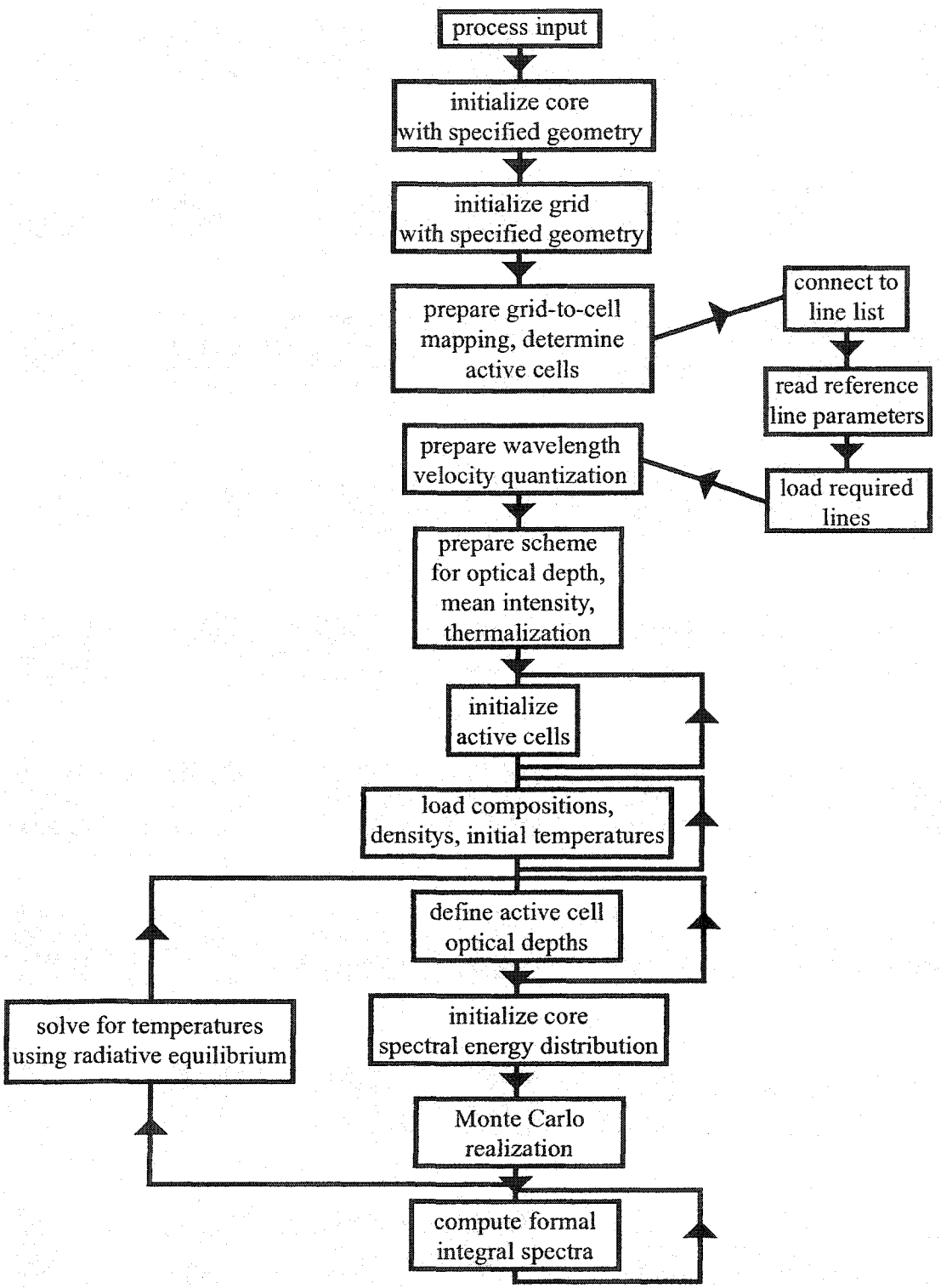

Figure C.1: Flowchart for the `lteBrute` code.

```
pure character( len = 4 ) function ionStageLabel( aion )
-------------------------------------------------------
 integer, intent( in ) :: aion
```

C.1.2 atomLabel

Returns the symbol for a given atomic number.

```
pure character( len = 2 ) function atomLabel( anum )
----------------------------------------------------
 integer, intent( in ) :: anum
```

C.1.3 ionLabel

Returns a string containing the complete name of an ion with a given atomic number and ionization stage.

```
pure character( len = 6 ) function ionLabel( anum, aion )
---------------------------------------------------------
 integer, intent( in ) :: anum, aion
```

C.1.4 atomWeight

Returns the atomic weight of an atom with the given atomic number.

```
pure real( wp ) function atomWeight( anum )
-------------------------------------------
 integer, intent( in ) :: anum
```

C.2 LtePartFunc

C.2.1 hasLtePartFunc

Returns true if the particular partition function is here.

```
pure logical function hasLtePartFunc( anum, aion )
--------------------------------------------------
 integer, intent( in ) :: anum, aion
```

C.2.2 getLtePartFunc

Returns the LTE partition function at the given temperature.

```
pure real( wp ) function getLtePartFunc( anum, aion, temp )
-----------------------------------------------------------
 integer   , intent( in ) :: anum, aion
 real( wp ), intent( in ) :: temp
```

C.2.3 getChi

Returns the ionization potential of a given ion.

```
pure real( wp ) function getChi( anum, aion )
---------------------------------------------
 integer, intent( in ) :: anum, aion
```

C.3 CompClass

C.3.1 Comp_new

Constructor.

```
subroutine Comp_new( self, ctyp, natm, anum, abun )
---------------------------------------------------
 type( CompType ), intent( in out ) :: self
 integer         , intent( in     ) :: ctyp, natm
 integer         , intent( in     ) :: anum( natm )
 real( wp )      , intent( in     ) :: abun( natm )
```

C.3.2 Comp_file

Constructor, uses a standard kind of input file. The filename passed in must not include the '.abun' suffix.

```
subroutine Comp_file( self, fabu )
----------------------------------
 type( CompType )     , intent( in out ) :: self
 character( len = * ), intent( in     ) :: fabu
```

C.3.3 Comp_copy

Copy constructor.

```
subroutine Comp_copy( self, orig )
----------------------------------
 type( CompType ), intent( in out ) :: self
 type( CompType ), intent( in     ) :: orig
```

C.3.4 Comp_die

Destructor.

```
subroutine Comp_die( self )
---------------------------
 type( CompType ), intent( in out ) :: self
```

C.3.5 getMu

Gets the mean molecular weight thing, I think...

```
pure real( wp ) function getMu( self )
--------------------------------------
 type( CompType ), intent( in ) :: self
```

C.3.6 dumpComp

Output the composition.

```
subroutine dumpComp( self, flnm )
---------------------------------
 type( CompType )     , intent( in out ) :: self
 character( len = * ), intent( in     ) :: flnm
```

C.4 LteEosClass

C.4.1 LteEos_new

Initialize an LTE EOS solver with a list of atoms to use in the solution.

```
subroutine LteEos_new( self, natm, anum, abun )
-----------------------------------------------
 type( LteEosType ), intent( in out ) :: self
 integer           , intent( in     ) :: natm
 integer           , intent( in     ) :: anum( natm )
 real( wp )        , intent( in     ) :: abun( natm )
```

C.4.2 LteEos_copy

Copy constructor.

```
subroutine LteEos_copy( self, orig )
-------------------------------------
 type( LteEosType ), intent( in out ) :: self
 type( LteEosType ), intent( in     ) :: orig
```

C.4.3 LteEos_die

Destructor.

```
subroutine LteEos_die( self )
-----------------------------
 type( LteEosType ), intent( in out ) :: self
```

C.4.4 setLteEos

Solves the LTE equation of state for the previously specified composition given a total number density and temperature. Note that if you are looping over density and temperature, the density should be the inner loop and temperature the outer one. For a given temperature, the Saha ratios are the same, and as long as you don't change the temperature the Saha ratios are cached.

```
subroutine setLteEos( self, nden, temp )
----------------------------------------
 type( LteEosType ), intent( in out ) :: self
 real( wp )        , intent( in     ) :: nden, temp
```

Appendix D

List of Acronyms

CD	common-direction (velocity surface)
CP	common-point (velocity surface)
DCO	discretized continuous opacity
EEP	equal-energy packet
ES	elementary supernova
ETLA	equivalent two-level atom
GRB	gamma-ray burst
HV	high velocity
IR	infrared
LTE	local thermodynamic equilibrium
MC	Monte Carlo
MPI	message-passing interface
NLTE	non-local thermodynamic equilibrium
PV	photospheric velocity
RTE	radiative transfer equation
SED	spectral energy distribution
SN, SNe	supernova, supernovae
TE	thermal equilibrium